Spatial and Temporal Control of Lipid-Membrane Morphology Induced by Sphingomyelinase

by

Ling Chao

Bachelor of Science, Chemical Engineering
National Taiwan University, 2003

Submitted to the Department of Chemical Engineering in Partial Fulfillment of the Requirements for the Degree of

DOCTOR OF PHILOSOPHY IN CHEMICAL ENGINEERING

at the

MASSACHUSETTS INSTITUTE OF TECHNOLOGY

June 2009

Signature of Author:_____
Ling Chao
Department of Chemical Engineering
May 11, 2009

Certified by:_____
Klavs F. Jensen
Warren K. Lewis Professor of Chemical Engineering
Professor of Materials Science and Engineering
Thesis Supervisor

Certified by:_____
Alice P. Gast
Adjunct Professor of Chemical Engineering
Thesis Supervisor

Certified by:_____
T. Alan Hatton
Ralph Landau Professor of Chemical Engineering
Thesis Supervisor

Accepted by:_____
William M. Deen
Professor of Chemical Engineering
Chairman, Committee for Graduate Students

Spatial and Temporal Control of Lipid-Membrane Morphology Induced by Sphingomyelinase

by

Ling Chao

Abstract

Sphingomyelinase (SMase) has been shown to be involved in a variety of cell regulation processes. It can convert sphingomyelin (SM) to ceramide (Cer) and has been suggested to influence the cellular processes by reorganizing the cell membrane morphology. This thesis aims at a more comprehensive understanding of how sphingomyelinase (SMase) can regulate lipid membrane heterogeneity.

We develop corralled model raft membranes in a microfluidic device to study the complex phase phenomena induced by SMase. The mass balance of lipid molecules in each confined corral greatly helps us to interpret results. By using the corralled membrane arrays, we are able to obtain the overall statistical distribution of the induction time of a slow domain nucleation and therefore fairly compare the membrane responses caused by different factors. In addition, the flow control by a microfluidic device solves the difficulty of distributing SMase uniformly to membrane systems. Furthermore, the laminar flow in a microchannel allows us to create model membrane arrays with a variety of lipid membrane compositions or solution conditions, which can serve as a screening tool to study a broad range of parameters associated with the interactions between lipid membranes and SMase or other peripheral proteins.

We report that SMase can induce both a reaction-induced and a solvent-mediated phase transformation, causing switches of three stationary membrane morphologies and multiple-time-domain ceramide generation in model raft membranes. During the reaction-induced phase transformation, the ceramide generated by SMase causes the disintegration of pre-existing rafts rich in sphingomyelin and cholesterol, and recruit sphingomyelin to form SM-enriched domains which are relatively inaccessible to SMase. Once most of the sphingomyelin is physically trapped in SM-enriched domains and the SM concentration in the SMase-accessible region becomes low, the morphology pauses. The pause situation is resolved after the formation of a 3-D feature, rich in SMase, sphingomyelin (SMase's substrate), and ceramide (SMase's product), which triggers the solvent-mediated phase transformation. This 3-D feature is hypothesized as a slowly nucleating SMase-enriched phase where SMase processes sphingomyelin at low concentration more efficiently. The disparate time-scales of the formation of these SMase-features and the SM-enriched domains allow for the development of a significant duration of the middle pause morphology between the two transformations. The results show that SMase can be actively involved in the lipid membrane phase changes. The SMase-induced multi-stage morphology evolution is not only due to the membrane compositional changes caused by SMase,

but also due to the selective binding of SMase, and SMase's special phase behavior during the solvent-mediated phase transformation.

We further demonstrate that lipid membrane composition and SMase concentration can be used to tune the two phase transformations and therefore the intervals and spatial patterns of SMase-induced multi-stage morphology evolution. At a physiologically relevant concentration of SMase, we observe that membrane composition can influence the formation of SM-enriched domains and the nucleation of SMase-features at different extents of time scale and thus significantly tune the stable duration of the middle pause morphology. More importantly, the induction time of SMase-feature nucleation can be significantly decreased by increasing the supersaturating level of its three components in the membrane system.

We further model the spatio-temporal morphology change during the solvent-mediated phase transformation. Three major kinetic processes are described in the model: the consumption of SM by the enzymatic reaction at an SMase-feature, the diffusion of SM from SM-enriched domains to an SMase-feature, and the release of SM due to the dissolution of SM-enriched domains. We combine MATLAB coding with Comsol, a software using finite element method to solve partial differential equations, to solve the model numerically due to the complex geometry and the moving boundary of our membrane systems. The non-dimensionality of the model allows the system to be characterized by three non-dimensional parameters. We show all of the possible scenarios of spatial pattern change during the phase transformation. The modeling results are shown to be consistent with our experimental results and can provide insights into the system parameters which are difficult to measure.

Thesis Supervisors: Klavs F. Jensen, Warren K. Lewis Professor of Chemical Engineering

Alice P. Gast, Adjunct Professor of Chemical Engineering

T. Alan Hatton, Ralph Landau Professor of Chemical Engineering

ACKNOWLEDGEMENTS

It has been my great pleasure to work with three thesis advisors, Professors Klavs Jensen, T. Alan Hatton, and Alice P. Gast. I would like to express my gratitude for all of their guidance and support. I have greatly benefited from Klavs's guidance, wisdom, insights, and professional support during the last three years. His suggestions helped to shape my research skills, which helped me focus my research questions and obtain a thorough scientific story for my thesis work. In addition, with his help, I was able to transfer from the former Gast lab to the Jensen lab smoothly. This thesis would not have been possible without Alice, who during our first meeting introduced me to this interesting project. She was an encouraging mentor, providing me with both great freedom and direction in my project. I feel honored to have been her last student before she became the President of Lehigh University. Alan has been an encouraging mentor, providing me with motivation when I encountered difficulties in my research, and it has always been fun to work with him.

I thank my thesis committee, Professors Alexander M. Klibanov, Georges Belfort, and Patrick S. Doyle, who generously provided me with invaluable inputs and suggestions. I would also like to extend my gratitude to Bob in the MIT writing center. He has worked with me on my thesis for half a year. My writing skills have significantly improved with his help. I also thank the wonderful ChemE staff at MIT: Suzanne Easterly, Richard Lay, Mary Wesolowski, Katie Lewis, Iris Chang, and Alina Haverty, who were always willing to help.

All of the people in the Jensen group have made me feel at home for the last three years. I really enjoyed everyone's company and appreciate their friendship. Many of them have greatly contributed to my personal and professional time at MIT. Mahmooda Sultana has become one of my closest friends, providing unlimited and invaluable supports. I feel grateful to have gotten to know her; our constant exchange of ideas has greatly contributed to my personal and professional development. Kishori Deshpande and Andrea Adamo are always there to provide me with wise professional suggestions and emotional support. Hemant Sahoo, Jane Rempel, Vicki Dydek, and Jain Wen have provided me with many great suggestions and fun conversations.

Everyone in the Hatton group has always been very friendly and fun. I especially appreciate Fei Chen's help with solving the moving boundary problems in Comsol and Ying Diao for testing some samples in XRD for me. My former group, the Gast group, also provided a great working environment. I especially thank Paulina Achurra for introducing me to soft-lithography and Margaret Horton for teaching me a lot about lipid membranes.

My time at MIT was enjoyable in large part due to many friends. I am grateful for the fun time and unlimited support from these friends: Liang-yu Chen, Susan Nasr, Iris Chang, Chin-Wu Chen, Chia-Ling Pai, Yi-Chun Lu, Amy Chi, Wan-Chen Lin, Chiara Toglia, Lisa Kung, Yu-Chen Ye, Hsin-Pe Shih, Aone Wang, Shu-Jen, Mo-Han Shih, Yi-Fan Lin and many other friends I met through ROCSA. I would like to extend my appreciation to Susan Nasr: her kindness, optimism, and perseverance have greatly influenced my attitudes towards difficulties and contributed to my survival at MIT.

Finally and most importantly, I am grateful to have a wonderful family. Thanks to my parents, my grandparents, my aunts, and my brother, for their love, unconditional support, and encouragement through all of these years.

TABLE OF CONTENTS

3. Sphingomyelinase-induced phase transformations: causing morphology switches and multiple-time-domain ceramide generation in model raft membranes

LIST OF FIGURES

LIST OF TABLES

Chapter 1. Introduction

1.1. Heterogeneity in Biological Lipid Membranes

The cell membrane used to be viewed as a homogeneous phospholipid bilayer, which acts mainly as a solvent for integral proteins and as a permeability barrier for the cell.[1] The perception of the cell membrane structure and dynamics has changed since researchers found detergent-resistant fractions rich in sphingomyelin (SM) and cholesterol (Ch) in plasma membranes, which was defined as lipid rafts (Figure 1-1).[1,2] The strong interaction between some lipids is suggested to cause the phase separation in cell membranes. The concept of heterogeneity in lipid membrane has been further developed after researchers extensively studied the lipid membrane phase behavior by reconstituting the lipid raft composition in cell-free lipid model membranes.[3-5]

Lipid membrane heterogeneity has been proposed as playing important roles in many cellular processes.[6] Segregation of various membrane domains in the cell membrane can create spatially segregated environments, resulting in suitable platforms for signal transduction.[7] However, questions still remain about lipid membrane domains' size and stability, and about how their functional mechanisms can be regulated.[8-10] Therefore, knowledge about the underlying mechanisms that control lateral lipid membrane heterogeneity is important for understanding the cell membrane's organization.

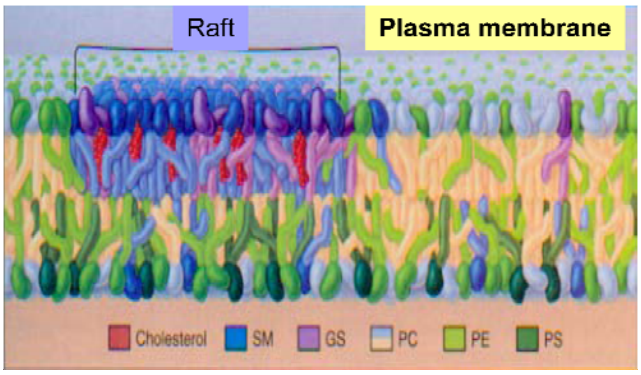

Figure 1-1. Illustration of a lipid raft in cell plasma membranes.[2]

1.2. Roles of Sphingomyelinase in Nature

Sphingomyelinases (SMase) are enzymes that occur naturally in mammalian and bacterial cells and catalyze the hydrolysis of the lipid sphingomyelin into ceramide and phosphorylcholine (Figure 1-2). Many different kinds of sphingomyelinases have been identified and are characterized by their ion dependence, pH optimum, or cellular localization.[11] A list of the sphingomyelinases with their corresponding optimal pHs and locations can be found in reviews.[12,13] Among the different kinds of SMase, SMase from *Bacillus cereus* has been used often for model system studies since its secondary structure,[14] Mg^{2+} binding and catalytic function,[15] and active site [16] is better known.

In general, SMase has been suggested to be involved in a variety of cell regulation processes, particularly in programmed cell death (apoptosis).[13,17-23] One of the two principal pathways in apoptosis is receptor-mediated signaling at the plasma membrane.[24] Many of these death receptors have been reported to require SMase for their biological effects, and ceramide

accumulation is generally observed in cells undergoing apoptosis.[25-29] Some other studies have shown that SMase is required for causing radiation-induced apoptosis in tumor cells.[30-33] Furthermore, SMase has been demonstrated to mediate the infection of pathogens.[34,35]

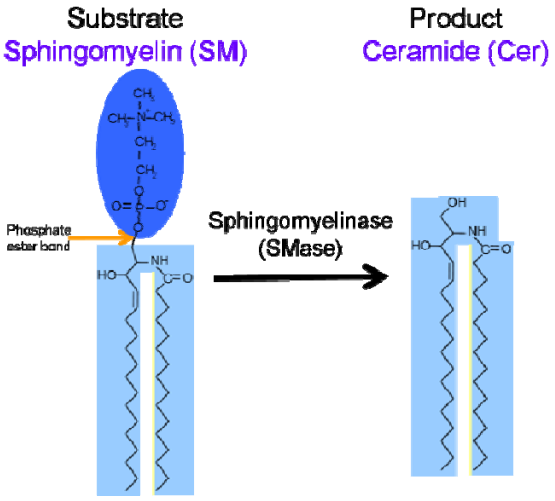

Figure 1-2. Sphingomyelinase can hydrolyze sphingomyelin at its phosphate ester bond; the product is ceramide.

1.3. Roles of Ceramide in Nature

Ceramide is a sphingolipid that has gained much attention as an important signaling molecule in vital cell processes as diverse as apoptosis, growth arrest, senescence, differentiation, mediating an immune response, and cell cycle arrest.[12,36] Structurally, ceramides are composed of a fatty acid chain, of varied length, saturation, and hydroxylation, bound via an amide linkage to the amino group of a sphingoid base. Ceramides constitute the hydrophobic backbone of all the complex sphingolipids: sphingomyelin, cerebrosides, gangliosides, and others. The fatty acid chain length of ceramide can vary from two to 28 carbons, although C-16 to C-24 ceramides are

most abundant in mammalian cells. These fatty acids are usually saturated or monounsaturated.[12] Ceramides are among the least polar, most hydrophobic lipids in nature.

Recent studies have begun to unravel the biophysical roles of ceramide in cell signaling. The generation of ceramide by sphingomyelinase in response to a stress signal or other agonist can induce local changes of the membrane environment. This, in turn, could affect the permeability and fluidity of the membrane, increase movement of proteins into or from lipid rafts, cause conformational changes in membrane-associated enzymes or receptors, etc. Although ceramide has also been thought as a "second messenger" (a small molecule that has direct downstream targets in cell signaling pathways), there is still no evidence showing which downstream targets can directly interact with ceramide. In addition, unlike other better-studied second messengers, such as lysophosphoglyceride generated by phospholipases A2 (PLA2), ceramide has been found to strongly favor partitioning into bilayers instead of being a free lipid in solution. The hydrophobic property further increases the possibility that the main role of ceramide is to cause changes in the membrane properties.

Some studies have shown the differing properties of sphingomyelin and ceramide. Wang et al. observed that ceramide exhibits a much higher affinity for ordered lipid domains than does sphingomyelin.[37] In addition, sphingomyelin interacts very tightly with cholesterol, through hydrogen-bonding between the C-3 hydroxyl group of cholesterol and the headgroup of sphingomyelin, and this serves as the basis for raft formation. Ceramide, on the other hand, have very poor affinity for cholesterol and tend to separate into ceramide-enriched domains.[38] These

property differences have implied the possibility that the turnover of sphingomyelin to ceramide will change both the dynamics and biophysical properties of cell membranes.

1.4. Sphingomyelinase-Lipid Membrane Interactions

1.4.1. Influence of Lipid Membrane Properties on Sphingomyelinase's Behavior

Sphingomyelinase is one kind of peripheral protein. Evidence has shown that lipid organization can modulate the interaction of many different kinds of peripheral proteins with membrane surfaces. These peripheral proteins non-covalently bind to lipids, and thus the physical chemistry of the lipid interface allows for a rapid and reversible control of peripheral interactions. Kinnunen et al. provided a good review showing how composition, molecular organization, surface pressure, electrostatic potential, interfacial curvature, and physical state (e.g., gel, fluid, liquid-ordered etc.) of membrane lipids can regulate the binding of many different kinds of peripheral proteins to the lipid surface.[39]

Interfacial lipases belong to a category of peripheral proteins that can hydrolyze their lipid substrates after binding the lipid membranes. It is generally believed that the intermolecular organization of the lipid substrate markedly affects the activity.[39-48] Among various phospholipases, phospholipases A2 (PLA2) has been extensively studied on lipid monolayers and could provide some insights into other lipases' behaviors.[41,49-51] PLA2 have been found to have a lag time after the enzyme is exposed to membranes. Some studies have shown that the existence of phase separation can reduce the lag time or increase the burst activity. PLA2 reaches its maximum activity in the range of temperature where the gel-to-liquid phase transition

of the phospholipid substrate takes place.[51,52] Grainger et al. found that lateral separation and domain formation originated by the addition of non-substrate molecules would also induce activation of PLA2.[53] The burst of activity at the end of the lag time is promoted by lateral domain separation produced when the enzymatic lipid products reach a defined concentration threshold. Further, the products or phases formed after the addition of PLA2 also seem to influence PLA2's activity and binding behavior. For example, the connectivity of distributed substrate domains has been found to modulate pancreatic PLA2's adsorption and activity.[54] Grainger et al. observed that the formation of PLA2 enriched regions by epifluorescence microscopy occurs after the products were generated in lipid monolayers.

In the last decade, sphingomyelinase has started to attract attention since it is found to be involved in many cellular processes and its substrate is an important component of lipid rafts. SMase activity was found to have lag times, followed by bursts of activity. The lag time of SMase on the monolayers is suggested to originate from the partitioning process at the interface and a bimolecular enzyme-dependent step followed by a slow, irreversible rate-limiting enzymatic activation. After the lag time, the enzymatic activity rises quickly and reaches a steady-state regime, subsequently followed by a gradual halting of product formation.[55]

Among the studies from monolayers and small lipid vesicles, the most conclusive finding regarding SMase's behavior is that SMase prefer their substrates in fluid states rather than gel states.[45,56] Most kinds of sphingomyelin from different species have a gel-to-fluid transition temperature in the physiological range of temperature (35˚C-45˚C). An interesting case is that Ruiz-Arguello et al.[56] have observed that the activity of SMase is lower when the lipid vesicles

are in a gel state. When the temperature is increased and the systems have crossed into the fluid states of the substrate, the activity increases and the lag time is decreases. They have also observed that SMase activity at 37˚C increases in proportion to the ratio of glycerophospholipids, as diluting lipids, and the lag time becomes progressively shorter. Their studies suggest that SMase requires the lipid substrate to be in a fluid bilayer, irrespective of whether this is achieved through a thermotropic transition or by modulating bilayer composition.[56]

1.4.2. Influences of Sphingomyelinase on Lipid Membrane Structures

Many physiological studies have reported that SMase can induce cell morphology changes during apoptosis. In general, large lipid membrane platforms with clustered receptors have been observed in cells within a few minutes after SMase is activated, which is the early stage or induction phase of apoptosis.[28,35,38] The large platforms are thought to help concentrate and thereby cluster the required membrane receptors, while the clustering has been found to be an essential step for those receptors to trigger their subsequent cellular pathways.[57] At late stage or the execution phase of apoptosis (occurring in hours or days after SMase is activated), the membrane blebbing (or apoptotic body formation) can be observed. The blebbing, it has been suggested, may be facilitated by the negative spontaneous curvature induced by ceramide.[58,59]

In model systems, many structural changes of membrane systems induced by SMase have also been observed. These structural changes include lateral phase separation or domain formation, enhancement of membrane permeability, the induction of membrane fusion, and small lipid vesicle formation at the surface of giant vesicles. A brief summary is shown below.

Domain formation has been detected by various kinds of analytic tools. For example, a combination of differential scanning calorimetry and IR spectroscopy techniques has been used to show that less than 5 mol% can cause a gel-fluid transition in small lipid vesicles.[60-62] Epifluorescence microscopy has been used to visualize the formation of dark domains on pure SM monolayers.[63,64] Literature attributes the domain formation primarily to the distinctive molecular structure of ceramide. First, chain mismatch appears to be an important factor regulating the phase separation; however, such a phenomenon has also been observed in the absence of chain length disparity in ceramide-phospholipid mixtures.[60,65] Second, ceramide can act both as acceptors and donors through their hydroxyl and amide groups, and thus have the capacity to form extensive hydrogen bonds in the phospholipid bilayers.[65,66]

In addition to the domain formation or phase separation, several groups have also found that adding SMase to SM-containing membranes induces membrane permeability and budding of vesicles. Ruiz-Arguello et al. have observed that rapid efflux of fluorescent dyes occurred after addition of SMase to large unilamellar vesicles consisting of SM, PE, Ch (2:1:1 mole ratio).[67] Montes et al. have shown that the mere presence of long chain ceramide can dramatically alter the membrane permeability.[68] The solute efflux was proposed to come from the property that ceramide easily induces negative monolayer curvature, which causes membrane instability.[38] Figure 1-3(a) illustrates how the small-head-group molecular shape of ceramide can facilitate the lamellar-hexagonal transition of lipids and cause the instability. Nurminen et al. coupled SMase to microspheres held in a micropipette and brought the micropipette into contact with a giant liposome membrane (with SOPC and SM) on a defined region where the enzyme reaction can be

examined by microscopy. They observed the shedding of small vesicles from the membrane into the interior of the giant liposome.[69] Zha et al. found adding SMase or ceramides induces the rapid formation of vesicles (400nm) in fibroblasts and macrophages in the absence of ATP.[70] This budding capacity has also been attributed to the tendency of ceramide to induce negative spontaneous curvature (Figure 1-3(b)).[71]

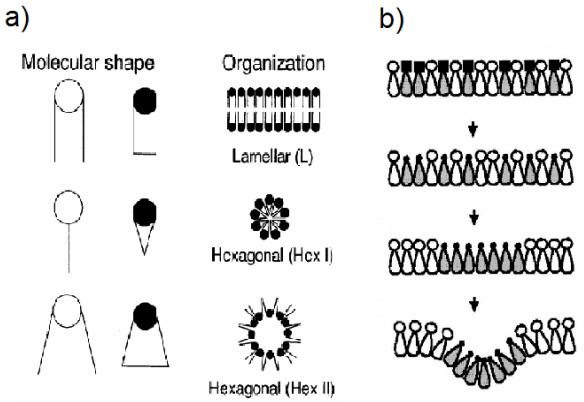

Figure 1-3. (a) A general correlation between the molecular shape and its preferred molecular organization. (b) A schematic illustration of how the curvature can be generated after the formation of ceramide domains. [71]

Most of the studies have attributed the structural changes to the appearance of ceramide. Recently, some studies have started to suggest that SMase molecule itself may also play roles in the structural or phase changes besides generating ceramide. Studies on pure sphingomyelin monolayers have shown that ceramide generated by SMase *in situ* can induce pattern formation in membrane domains which cannot be achieved by incorporating ceramide *ex situ.*[64,72] Recently, in model raft membranes, Johnston et al. and Chiantia et al. have used atomic force microscopy (AFM) to demonstrate that SMase can induce topographical features more complex than those generated by incorporating ceramide *ex situ.*[73,74] However, the AFM studies have

difficulty recording the kinetic processes of morphology changes in the presence of SMase because of tip contamination problems, and have not been able to identify how SMase is involved in the complex phase changes. Although some studies have used fluorescence microscopy to record the real-time morphology changes in the presence of SMase, only early time changes have been reported.[75,76] The complex heterogeneity, varying from region to region and sample to sample, also makes the characterization difficult.

1.5. Model Lipid Membrane Systems

Model lipid membrane systems can be useful for studying the physical principles governing the nature of the cell membrane because allow simplification of an otherwise impossibly complex cell membrane. The current knowledge of the molecular processes occurring at biological membranes has been aided by studies performed on lipid monolayers and bilayers in various configurations: at the air-water interface, as giant unilamellar vesicles (GUVs; liposome size above 1μm) in solution, as black lipid films, and in various kinds of supported lipid bilayers (SLBs) distinguished by the method of formation. By studying lipid-enzyme interaction in model membrane systems, their physical chemistry can be isolated from a multitude of other processes. The occurrence and properties of domains can be monitored with lipid probes and optical measurements. The use of fluorescent lipid probes is particularly convenient because they allow direct visualization of domains large enough to be resolved microscopically.

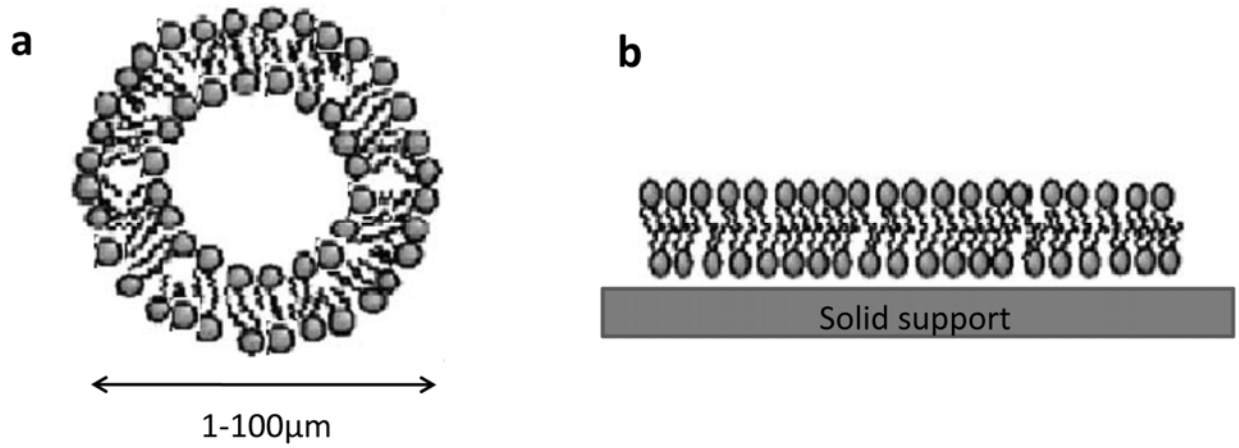

Figure 1-4. Models of biological membranes: (a) Giant unilamellar vesicles (GUVs) (1μm to 100 μm in diameter); (b) Bilayers formed by vesicle deposition on mica, glass, or silica (supported lipid bilayers, SLBs).

Among the model membranes, GUVs[77,78] and SLBs[79,80] have received substantial attention. GUVs consist of a bilayer in the shape of a spherical shell, separating an "intracellular" liquid volume from the "extracellular" space (Figure 1-4(a)), while the SLBs are planar extended bilayers adsorbed on a suitable solid surface (Figure 1-4(b)). Although the preparation procedure of monolayers is more developed, the behavior of domains in monolayers may not be entirely representative of cell membranes composed of lipid bilayers. Black lipid films are unsupported planar lipid bilayers which can be formed by a brush technique in a 150–200 mm diameter hole in Teflon film and bathed by buffers (Figure 1-4(c)). They can be voltage-clamped to determine their capacitance for the purpose of studying transport of materials across the membrane[81]; however, the preparation is more difficult and less robust. Among the model membranes, giant unilamellar vesicles (GUVs) and supported lipid bilayers (SLBs) were used in this project.

GUVs consist of a free standing bilayer in the absence of solid support effects[77,78], while the SLBs have a fixed position, making it easier to trace domain changes[79,80].

1.5.1. Supported Lipid Bilayers (SLBs)

The fixed position of SLBs can facilitate the interpretation of structural and dynamic data obtained in a system. That is, unlike a GUV moving and rotating around in the solution, planar lipid bilayers ease the tracing of domain formation and movement since they are fixed to a surface. In addition, SLBs are compatible with a wide range of surface analytical tools requiring planar geometry. These tools include surface plasmon resonance (SPR),[82] atomic force microscopy (AFM),[83] Brewster angle microscopy, quartz crystal microbalance (QCM) [84], ellipsometry, and fluorescence recovery after photobleaching.[85-88] In early studies, SLBs were mostly formed by sequential Langmuir-Blodgett (LB) deposition of two lipid monolayers on a hydrophilic substrate[79,89-92] (Figure 1-4(d)); however, McConnell and coworkers found that small vesicles can undergo rupture and fusion to form an extended, adsorbed, planar bilayer on suitably prepared surfaces.[93] This spontaneous self-assembly of supported continuous bilayers from vesicles in solution is commonly used for creation of SLBs today. The primary reason to choose the vesicle deposition method, rather than LB deposition, is its experimental simplicity and reproducibility. In addition, it is easy to integrate functional components such as integral proteins [85,94] into the membrane.

Although questions remain about the influence of the solid support on some aspects of supported planar lipid bilayers, some experiments have shown that supported bilayers retain their fluid

properties by trapping a thin water layer between the solid support and the lipid bilayer.[95] Dietrich et al. further showed, by photobleaching experiments, that supported lipid bilayers diffuse laterally, indicating that the lipids retain their mobility. They have been shown to preserve the thermal phase transitions of lipids [96-99] and domain formation on them has also been observed [83,100-104].

1.5.2. Giant Unilamellar Vesicles (GUVs)

Giant unilamellar vesicles (GUVs) can provide a free standing bilayer, without potential solid support effects. They consist of a bilayer in the shape of a spherical (in the bulk phase) shell, separating an "intracellular" liquid volume from the "extracellular" space (Figure 1-4(b)). In addition, the system is especially good for measuring permeability and observing domain mobility unrestricted by solid supports. GUVs can be easily prepared by the electroformation method developed by Angelova and Dimitrov[105,106], which generates vesicles with size ranging from 1-100 μm. Although phase dynamics can be easily observed on GUVs in the absence of solid support effects, they rotate and make it difficult to trace phase changes in lipid bilayers.

1.5.3. Model Raft Compositions

In this study, ternary mixtures of lipids with 1,2-Dioleoyl-sn-glycero-3-phosphocholine (DOPC), sphingomyelin (SM), and cholesterol (Chol) are primarily used to generate model raft membranes. The ternary mixture of an unsaturated lipid, a saturated lipid, and cholesterol have been demonstrated to have phase separation similar to that found in complex mixtures of cell

extracts.[3] Figure 1-5 illustrates the chemical structures of the three lipids. The strong interaction between sphingomyelin and cholesterol allows them to pack densely to form a liquid-ordered (L_o) phase.[38,107] DOPC is a symmetric unsaturated lipid, which usually packs less densely in lipid membranes, and usually separates from the liquid-ordered (L_o) phase to form a liquid-disordered (L_d) phase. These L_o and L_d phases appear below a certain transition temperature. Previous studies have used phase diagrams to demonstrate how the transition temperature depends on the lipid composition in ternary mixtures containing an unsaturated phospholipid, sphingomyelin and cholesterol.[5]

In giant unilamellar vesicles, we have observed that DOPC/BSM/Chol membranes readily phase-separate into mobile microscopic domains once the temperature is below the transition temperature. However, in supported lipid bilayers, the phase-separated domains are immobile[108,109], although the mobility of each lipid molecule has been shown to be retained. The domain size and morphology are found to relate to the thermal history during the preparation of the supported lipid bilayers.[110]

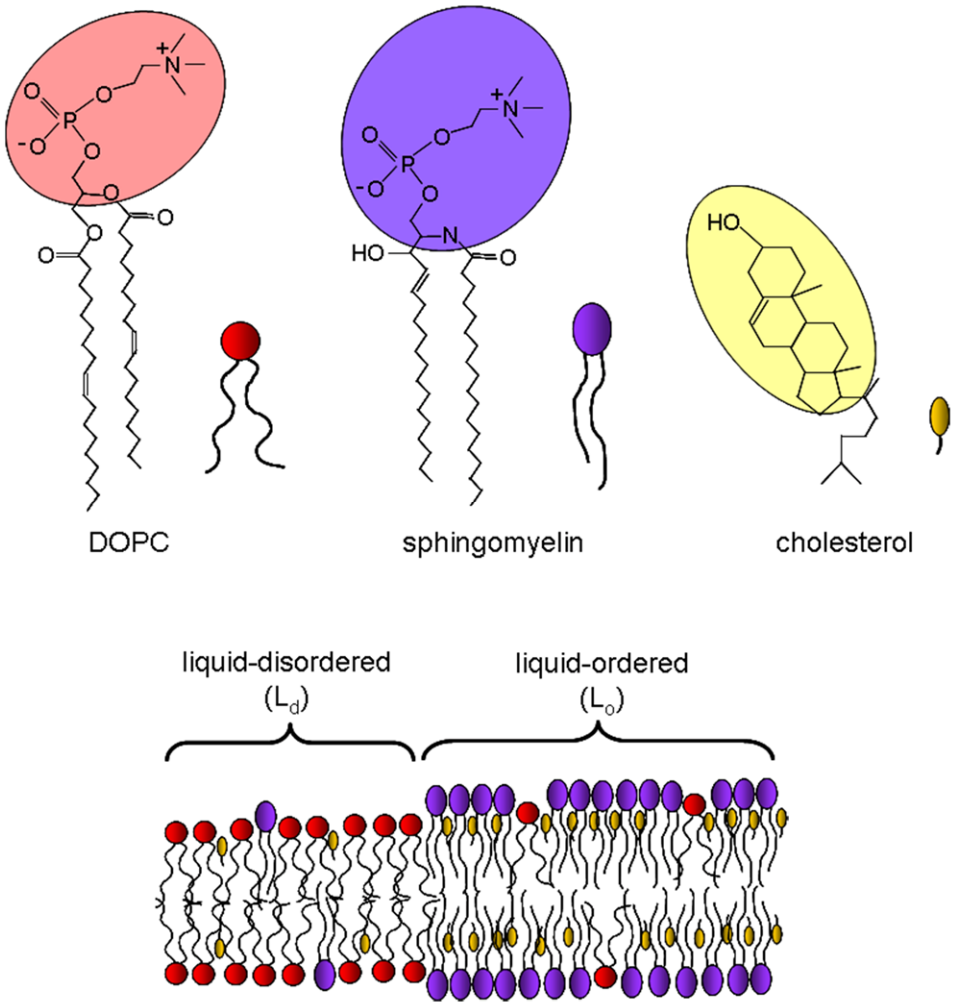

Figure 1-5. Lipid structure and schematic of model lipid rafts in a phase-separated lipid bilayer.[111]

1.6. Thesis Objectives and Overview

This thesis aims to provide understanding of how Sphingomyelinase (SMase) can regulate lipid membrane heterogeneity. We use corralled model raft membranes in a microfluidic device to study the underlying reorganization mechanism, which is complicated by the composition change caused by the reaction, the enzyme's selective binding to different phases, the enzyme's special phase behavior, and the substrate's accessibility and replenishment in different phases.

Chapter 2 describes the microfluidic platform with corralled membranes we developed in order to study the complex phase behavior induced by SMase. The corralled membranes provide a mass balance of lipid molecules during the reaction, and allow a large number of systems to be observed in parallel. The flow controlled by a microfluidic device solves the difficulty of distributing SMase uniformly. The laminar flow in a microchannel allows us to create model membrane arrays with a variety of lipid membrane compositions or solution conditions.

Chapter 3 reports two SMase-induced phase transformations in model raft membranes: a reaction-induced and a solvent-mediated phase transformation. Using multiple labeling approaches, we record the multi-stage morphology evolution and examine where the SMase, its substrate, and its product locate at different stages of the morphology evolution. The use of lipid probe's partition behavior as an internal reference allows us to correlate the characterization results to the morphology evolution with time. The results show that SMase is actively involved in the overall phase behavior, causing morphology switches and multiple-time-domain ceramide generation.

Chapter 4 examines carefully how the pre-existing rafts can be transformed to SM-enriched domains in the reaction-induced phase transformation. The large pre-existing domains in giant unilamellar vesicles and large annealed pre-existing domains in supported lipid bilayers allow us to visualize the dynamics of domains during the competition between ceramide and cholesterol for sphingomyelin.

Chapter 5 demonstrates that lipid membrane composition and concentration of SMase can be used to adjust the kinetic processes of the two phase transformations and thereby the intervals and spatial patterns of the multi-stage phenomena. Our corralled membrane systems allow us to capture the stochastic nature of domain nucleation, which is a major difficulty in quantifying and comparing the membrane responses caused by the different factors.

In Chapter 6, we develop a kinetic model to describe the morphology change during the solvent-mediated phase transformation. We combine Matlab coding with Comsol, a software using a finite element method to obtain spatio-temporal solutions, to numerically solve the system with complex geometry and moving boundaries.

Chapter 2. Microfluidic Devices for Studying Complex Phase Phenomena Induced by Sphingomyelinase

2.1. Introduction

Since the SMase enzymatic reaction has strong interplay with the physical states of lipid membranes, an effective control of microenvironment conditions during the enzymatic reaction is needed for studying the system with high spatio-temporal resolution information (domain dynamics) embedded in small amount of materials (lipid bilayers). We develop a microfluidic platform with model membrane arrays to achieve easy tracking of the observed membrane systems, effective control of reaction conditions, and high-throughput screening of experimental conditions. Two different types of model membrane arrays are developed. The arrays of supported lipid bilayer are formed by depositing small lipid vesicles to the glass surface patterned with protein corrals. The arrays of giant unilamellar vesicles are formed by physically trapping the giant vesicles into the protein-coated PDMS microwells by gravity. These developed systems are also suitable for studying the phase changes of lipid membranes caused by other peripheral proteins.

Most of our experiments are done in supported lipid bilayers (SLBs). Corralled supported lipid bilayers allow the mass balance of lipid molecules during the surface reaction, greatly helping the interpretation of the complex phase behaviors induced by SMase. In addition, the model

membrane arrays with numerous separated systems which can be observed in parallel are used to capture the stochastic nature of domain nucleation, in order to quantify the nucleation time and compare the influences from different factors. The flow control by a microfluidic device solves the difficulty in uniformly distributing SMase solutions to the membrane systems. Furthermore, the laminar flow in microchannels can allow the reagents to follow the streamline with only inter-diffusion, and thereby create a variety of lipid membrane compositions and solution conditions for each membrane system confined in corrals. The variation of conditions in the corralled systems on a single platform can be served as a screening tool to study a broad range of parameters associated with the interactions between lipid membranes and SMase or other peripheral proteins.

2.2. Development of Supported Lipid Membrane Arrays in a Microfluidic Device

2.2.1. Fabrication of PDMS Microchannels and Stamps

The polydimethylsiloxane (PDMS) stamps and microchannels used in my project are made by a method called soft lithography[112], a popular and reliable technique for producing microfluidic devices. PDMS is flexible enough to seal against most types of substrate surfaces and is rigid enough to maintain channel structures. The technique incorporates photolithography methods that have been used for years in the semiconductor industry into a micromolding scheme that eventually produces micron-sized structures in negative relief in PDMS. The individual steps are illustrated in Figure 2-1. Initially, a clean dry silicon wafer is spin-coated with a layer of SU8

photoresist whose thickness is equal to the desired thickness of the stamps or microchannels. A mask containing the pattern of structures is then placed over the wafer and exposed to ultraviolet light. The negative photoresist crosslinks in the areas exposed to the light. After being submerged in developer solution, only the crosslinked photoresist in the exposed regions remains on the wafer. This pattern of photoresist thus serves as a mold or master for PDMS stamps or channels. PDMS prepolymer, along with a curing agent, is then cast on the pattern-containing wafer. At an elevated temperature, the PDMS cures, producing a soft flexible material with the channels embedded in negative relief. The patterned PDMS can be easily peeled from the wafer. The stamps can be used immediately after being cut to a suitable size. The microchannel pieces can be sealed against a glass coverslip by treating the PDMS with air plasma. The holes are punched by 20 gauge needles (610μm) to form the inlets and outlets of the channels. We have made masters with various desired configurations in the Microsystems Technology Laboratories at MIT.

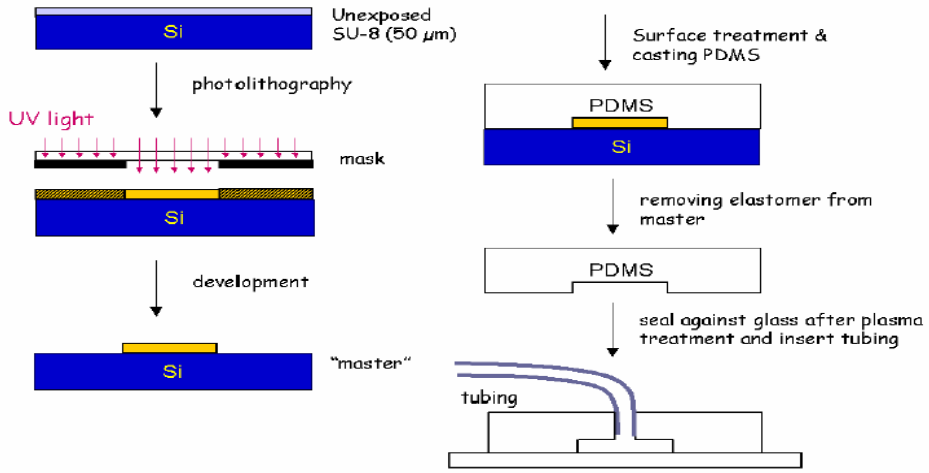

Figure 2-1. Preparation steps of a PDMS microchannel (The illustration is adapted from H. Lu).

2.2.2. Corral Printing by PDMS Stamps

Our goal is to create many different confined supported lipid membrane systems on a single platform. Kung et al. have used microcontact printing to print protein patterns as barriers to confine the lateral diffusion of lipids in lipid membranes.[113-115] The poly-(dimethylsiloxane) (PDMS) stamps used to print proteins onto glass is easy to integrate into my experimental setting. In our experimental procedure, we fabricated a stamp with numerous 50x50 μm^2 corral patterns. The size is chosen to mimic the relevant size of the plasma membrane of a cell. The surface of the PDMS stamp was oxidized for approximately 30 sec in air plasma before incubated in a solution containing 250 μg/mL bovine serum albumin (BSA) for 10 min. The stamp was then dried under a nitrogen stream, removing excess solution from the stamp. The stamp was then placed in contact with a clean glass surface under a weight of 10 g/cm^2 for about 10 min. After the printing, small lipid vesicles were applied to the patterned surface and deposited to the glass surface where there is no printed protein, creating supported lipid bilayers confined in corrals. Usually, we can distinguish the printed protein pattern only after the non-printed regions are filled with labeled lipid membranes. Here we use labeled BSA to demonstrate the performance of PDMS printing before lipid vesicle deposition (Figure 2-2).

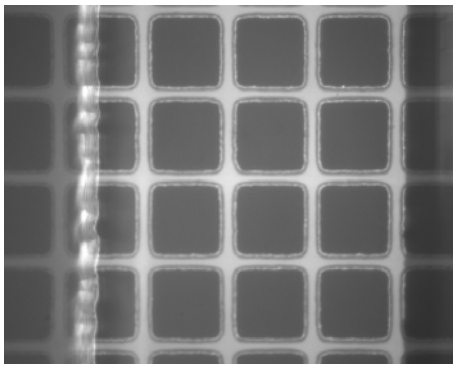

Figure 2-2. The Texas-Red® labeled-bovine serum albumin (BSA) printed on a coverslip in a 200μm wide microchannel. The inner size of each corral is 50μm x 50μm. The darker left and

right sides are the regions sealed with the PDMS slab. The boundaries show where the channel side walls are located.

2.2.3. Formation of Supported Lipid Bilayers

The spontaneous self-assembly of supported continuous bilayers from small unilamellar lipid vesicles in solutions is commonly used for creation of supported lipid bilayers (SLBs). The vesicle deposition process depends on the interplay of membrane-support, inter-membrane, and intra-membrane interactions. The nature of the support (its surface charge, structure, and roughness), the nature of lipid vesicles (their composition, charge, size, and physical state), and the aqueous environment (the pH and ionic strength) all influence the process.[79,83,84,86,90,116-124] Despite the accumulated efforts to understand and control the spontaneous SLB-formation process by vesicle deposition [79,83,84,90,120-124], the optimal approach to tailor bilayer formation is still unclear and experimental-based.

We chose some of our experimental parameters of vesicle deposition based on the directions provided by the previous literature. First, Ca^{2+} is a well-known promoter of SLB-formation[83,86,116,117]. We incorporated 2mM Ca^{2+} in our vesicle deposition buffer (10mM HEPES, 2mM CaCl2, 10mM CaCl2, 100mM NaCl, pH=7.4). Second, many solid supports have been reported as effective substrates for lipid vesicles to adsorb and break[84,118,119], and we chose glass coverslips as our solid support due to its transparency and easy-sealing with PDMS slabs. Third, Reimhult et al. have demonstrated that the vesicle to supported bilayer transition on SiO_2 (such as glass surface) is thermally-activated and temperature-dependent [125]; bilayer formation can be completely prevented even on SiO_2 at a sufficiently low temperature. In our experiments, we

operated the vesicle deposition process at a temperature 5°C above the miscibility transition temperature of the used lipid mixture. Furthermore, the vesicle to bilayer transition has been shown to be facilitated by applying osmotic stress on the vesicles [119]. We use pure water as the washing buffer to cause the osmotic stress.

Our experimental procedures for generating small unilamellar lipid vesicles are as follows. First, the lipid mixture with desired composition was dried from chloroform in a glass flask by nitrogen flow and the residual solvent was fully removed by placing the flask on a vacuum pump for at least 90 min. The dried lipid mixture was reconstituted in the buffer (10mM HEPES, 2mM $CaCl_2$, 10mM $CaCl_2$, 100mM NaCl, pH=7.4) at a concentration of 2.5 mM. After the lipid solution was mixed well and heated to a temperature above the miscibility transition temperature of the lipid mixture, it was extruded 19 times through an 80-nm polycarbonate filter in an Avanti Mini-Extruder (Alabaster, AL) to form small unilaminar vesicles (SUVs). The stock SUV solutions were stored at 4˚C for up to one week before being used. The stock solutions were diluted to 0.2 mg/mL just before use for the vesicle deposition.

The prepared SUV solution was heated to a temperature above the miscibility transition temperature of the lipid mixture and was flowed into a PDMS device with patterned glass surface which had been kept at the same temperature. After the vesicle solution was incubated with the glass surface for 30 min, water was flowed into the channel to wash away the excess vesicles. We have tested several operating parameters of the vesicle deposition process in a microchannel and listed them in Table 2-1.

Table 2-1. Operating parameters of the vesicle deposition process in a 50 μm high and 500 μm wide microchannel

Parameter	**Used value**	**If operating at a much smaller value**	**If operating at a much larger value**
Vesicle concentration	0.2 mg/ml	Not enough for critical coverage	Taking more washing time
Vesicle size	~80 nm	Difficult to generate by extrusion method	More defects observed in the formed membranes
Average exposure time of vesicle solutions to glass surface	30 min	More defects observed in the formed membranes	More adsorbed vesicles on the formed membranes
Washing flow rate	15μl/min	Insufficient washing and more adsorbed vesicles on the formed membranes	More defects observed in the formed membranes
Temperature during the vesicle deposition	5°C above Tm	Un-ruptured vesicles adsorbed on glass surface	More defects observed in the formed membranes

2.2.4. Microfluidic Assembly for Generating SLB Arrays

To assemble the PDMS microfluidic channel with SLB arrays, 20 gauge needles (610μm) were used to punch holes on the fabricated PDMS microchannel slabs in order to allow the later connection between the channel inlets and outlets to the tubing. The microchannel slabs with punched holes were then treated with air plasma for 15 sec, immediately followed by the sealing against a protein-printed glass coverslip. Tygon tubings were connected to the punched holes on PDMS slabs through 23 gauge stainless steel connectors. After the device was assembled, the lipid vesicle solutions were driven into the channel by either syringe pump or gravity. With the operating parameters introduced in the last section, the lipid vesicles deposited to the glass surface where no protein had been coated. The overall process is shown in Figure 2-3. The upper and side views of the formed corralled membranes are shown in Figure 2-4.

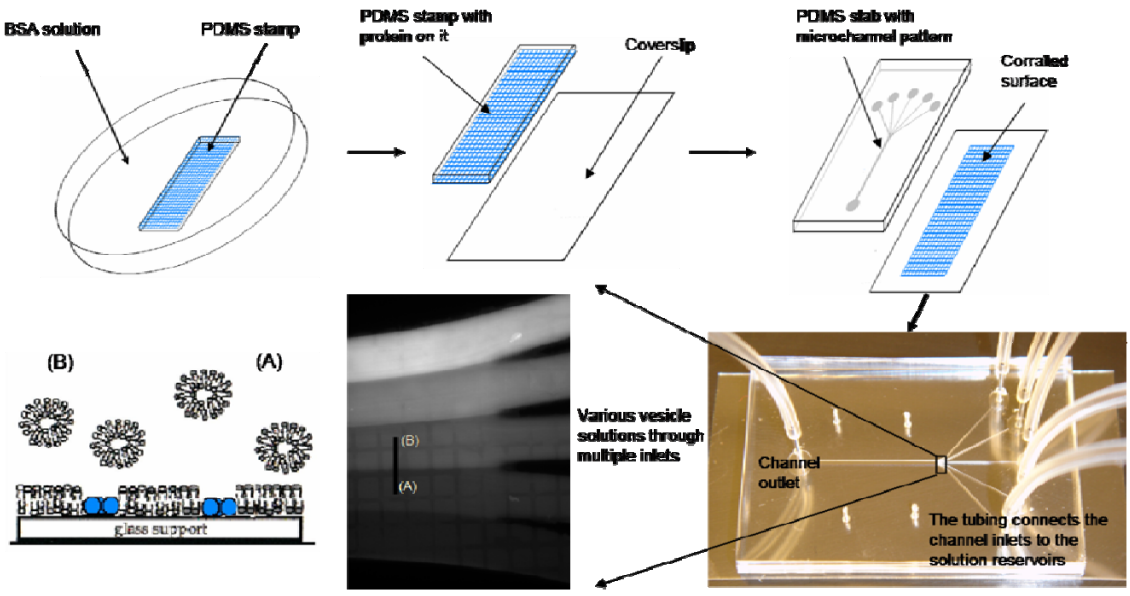

Figure 2-3. Formation of corralled supported lipid bilayers in a microfluidic device. The BSA (Bovine Serum Albumin) molecules are shown in blue color. They stained to the plasma-treated PDMS stamp and were printed to the glass surface before the PDMS microchannel slab was sealed with the glass. Lipid vesicles deposited to the region where there was no printed protein. Vesicle solutions with different compositions can be flowed into the main channel at the same time through multiple inlets to generate corralled membranes with different compositions in the same platform. More detailed will be introduced in the section 2-7.

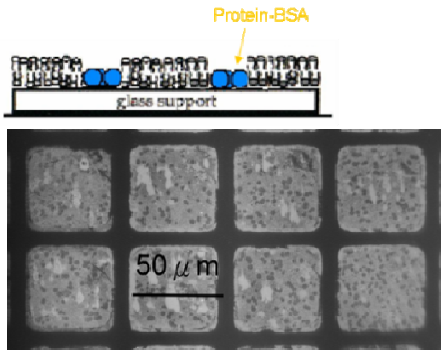

Figure 2-4. The upper view and side view of Texas-Red DHPE-labeled membrane systems confined in bovine serum albumin (BSA) corrals. The membrane composition is 40/40/20 molar ratio of DOPC/egg SM/ Cholesterol with 0.5%Texas Red®-DHPE.

2.3. Development of Giant Unilamellar Vesicle Arrays in a Microfluidic Device

2.3.1. Electroformation of Giant Unilamellar Vesicles (GUVs)

Giant unilamellar vesicles (GUVs) are spherical lipid bilayers that are 1-100 μm in diameter. We prepared GUVs by the electroformation method developed by Angelova and Dimitrov [105,106] in a special temperature-controlled chamber. As illustrated in Figure 2-5, dry lipid films on two conductive substrates are hydrated in aqueous solution; upon application of a gentle AC field, lipid bilayers swell from the film to form GUVs.

We followed the procedure developed by M. Horton, a previous group member. Indium tin oxide- (ITO) coated glasses were purchased from Präzisions Glas and Optik GmbH (Iserlohn, Germany) and were rinsed with deionized (DI) water. Approximately 40 μL of lipids in chloroform at a concentration of 5 mg/mL were spread on the ITO plates; the lipid films were dried 2 hr in a vacuum chamber. The dried plates were placed parallel 5 mm apart (face to face) in a Teflon holder filled with a swelling solution and connected to a function generator with 1 V AC, 10 Hz signal. The AC signal was applied 1.5-2.5 hr to form GUVs.

It has been shown that the presence of ions in the swelling solution is not ideal for the GUV formation, and that sugar solutions can stabilize the GUVs. Therefore, we used a sucrose solution as the swell solution and reconstituted the GUVs in the desired buffer after they were formed and removed from the Teflon holder. The concentration of the sucrose solution is set to

have the same osmolarity as the desired buffer to prevent the breakage of GUVs due to the osmotic stress during the reconstitution.

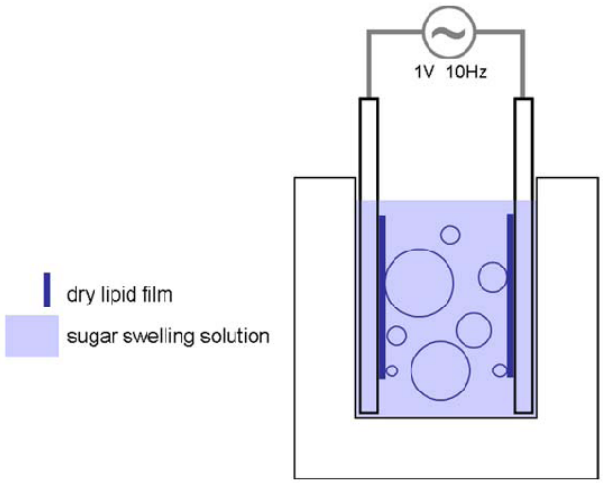

Figure 2-5. Electroformation of giant unlamellar vesicles (GUVs).[111]

2.3.2. Microfluidic Assembly for Generating GUV Arrays

We constructed GUV arrays by physically trapping GUVs into microwells made of polydimethylsiloxane (PDMS). The GUVs move and rotate in solutions. The trapping of them in microwells can facilitate us to keep track of the GUV during the observation of lipid membrane domain changes. The laminar flow in an incorporated microfluidic channel can also allow us to create the variation of solution conditions for GUVs trapped in different microwells. The PDMS microwell was fabricated by soft lithography and the steps are shown in Figure 2-6. After the fabrication of microwells in a microfluidic device, both a GUV solution and a buffer with lighter density than the vesicle buffer were flowed into the microchannel. The flows were stopped to allow the different streams to mix, resulting in lighter density solution outside GUVs than the solution insides GUVs. The larger density of the buffer inside GUVs than the density of the

buffer outside can drive the GUVs to settle down into the microwells due to gravity. Modifying the PDMS surface with bovine serum albumin (BSA) can prevent undesirable deposition of the GUVs to the surface.

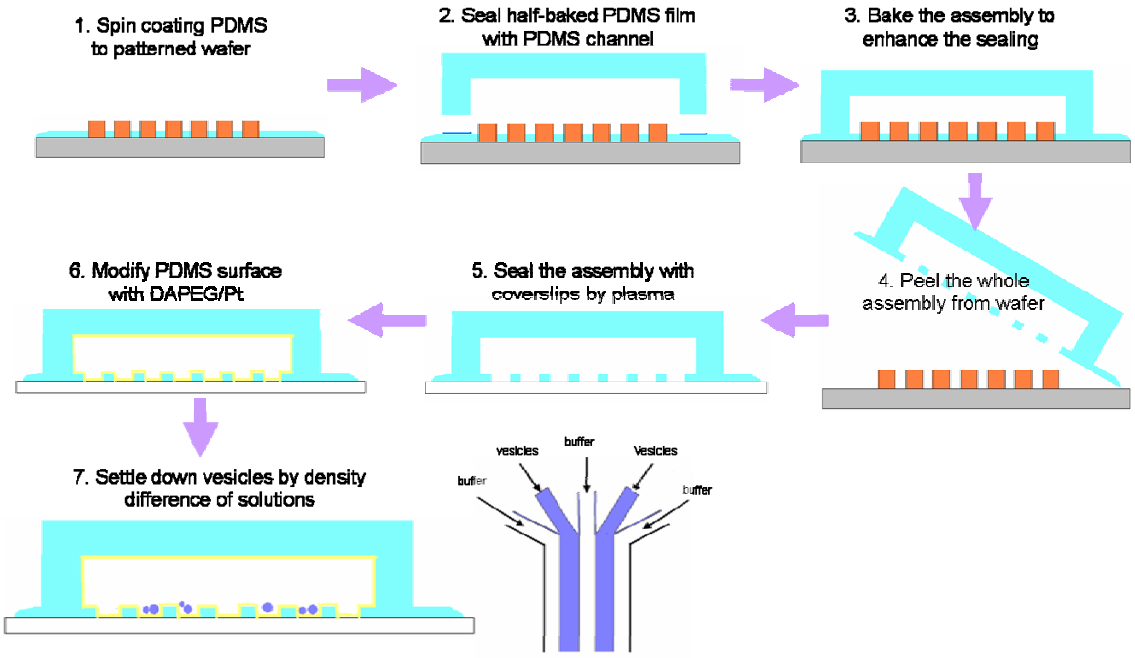

Figure 2-6. Formation of corralled giant unilamellar vesicles in a microfluidic device. After the fabrication of the microwell channel, the alternative flows of vesicle solutions and lighter-density buffers are directed into the channel in order to construct the density difference between the solution inside and outside the vesicles inside the channel, which drives the vesicles to settle into the microwell due to gravity.

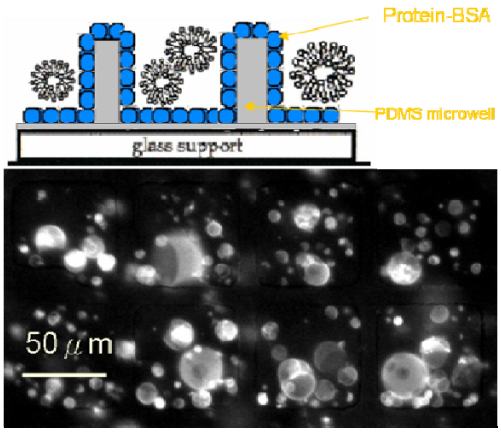

Figure 2-7. The upper view and side view of Texas-Red DHPE-labeled GUVs confined in PDMS microwells coated with bovine serum albumin (BSA). The membrane composition is 40/40/20 molar ratio of DOPC/egg SM/ Cholesterol with 0.5%Texas Red®-DHPE.

2.4. Mass Balance of Lipid Molecules in Confined Supported Lipid Bilayers

The SLB membrane in a corral can be viewed as an individual system. The isolation of each membrane system can allow the mass balance of lipid molecules in a corral during the surface reaction. The mass balance during to the reaction here refers to the 1 to 1 stochiometric relationship of the amount of sphingomyelin, the substrate of SMase, and the amount of ceramide, the product of SMase, and the confinement of the other un-reacted lipids in a corral. As we show in chapter 3 and 5, the mass balance dramatically helped the interpretation of the complex morphology changes induced by SMase.

We used the membranes with small amount of sphingomyelin-enriched phase (the dark phase indicated by white circle in Figure 2-8) at room temperature since this type of domain is microscopic and has a range of miscibility temperature which is accessible by the microscope-temperature stage we used. The temperature was increased 1°C every 10 min to ensure that the phase behavior in the membrane system close to its equilibrium state at the temperature during the temperature change. Figure 2-8 shows that the dark phase amount is consistent in the membrane systems confined to the same size. In addition, the dark phase dissolved with increased temperature. Furthermore, the same amount of the dark phase in a corral can be obtained in a corral after the temperature is increased from 24°C to a temperature at which all of the dark phase is dissolved (30°C) and then brought back to 24°C. Despite the same amount of phase in a corral, the dark phase nucleates at very different locations after the temperature cycle, indicating the mobile nature of the lipid molecules. The results indicate that the lipid molecules are restricted to each corral and are mobile in supported lipid bilayers confined in corrals.

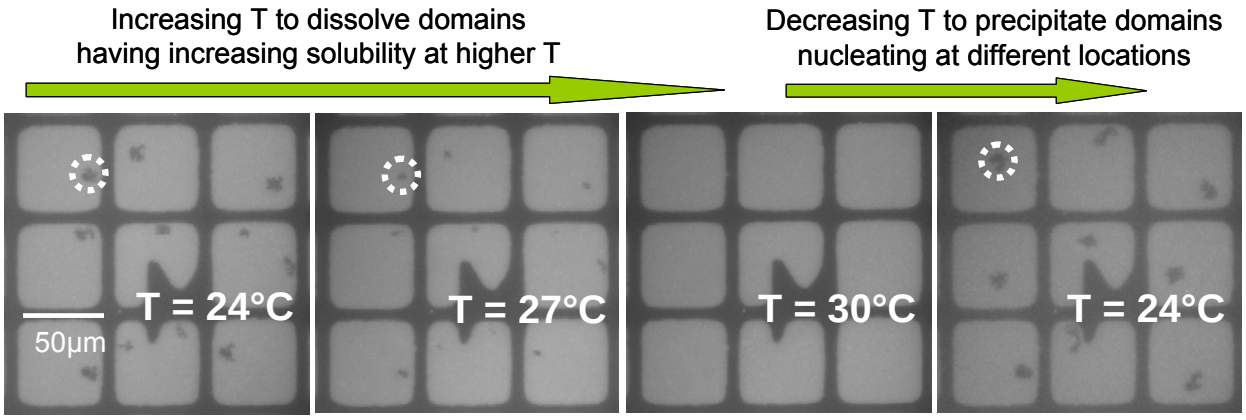

Figure 2-8. Temperature cycle to demonstrate the freely mobile nature of lipid molecules in the membrane confined in a corral. The open white circle highlights the dissolution-precipitation nature of the SM-enriched domains in supported lipid bilayers. The original morphology of this

system is formed after 0.005 unit/ml SMase is added to the membrane systems with 89.5mol% DOPC/ 10mol% Egg SM/0.5mol%Texas-Red® DHPE for 10 min.

2.5. Performance Comparison between the Developed SLB Systems and Conventional SLB Systems

To demonstrate the performance of the corralled membranes in a microfluidic device, we compared the morphology changes induced by SMase in a corralled membrane system in a microfluidic device and in a non-corralled membrane system with manual addition of reagents. Figures 2-9(a, b, c) are the typical Texas-Red® DHPE images of corralled membrane systems before the addition of SMase, about 20 min after the addition, and about 90 min after the addition. In this system, the flow conditions of lipid vesicle solutions and washing solutions during the formation of supported lipid bilayers were controlled at the operating conditions mentioned in section 2.1.3. After the corralled membranes formed, the flow was controlled to allow the lipid membrane to be exposed to 0.005 unit/ml sphingomyelinase (SMase) from *Bacillus cereus* for 2 min at room temperature. On the other hand, Figures 2-9(d, e, f) show the morphology change of a non-corralled membrane system. The membrane is prepared by conventional incubation/washing steps: the vesicle solution and washing buffer were added to and removed from a glass surface by pipette. The formed membrane on a glass was stored in a small chamber with buffers. The calculated amount of SMase solution is added to the small chamber by pipette to generate 0.005 unit/ml SMase concentration above the membrane system. Figures 2-9(d, e, f) are the cropped images from a region having the same size and corresponding timing as Figures 2-9(a, b, c) in a 2cm x 2cm piece of supported lipid bilayers.

Before the addition of SMase, we usually observed some irregular micron-sized dark regions in the membranes prepared by the conventional method (Figure 2-9(d)), but not in the corralled membranes prepared under controlled washing flows (Figure 2-9(a)). These dark regions might be defects reported in previous literature.[73,76] After the addition of SMase, they seemed to attract new domains to form around them, probably because growing around them is more energetically favorable than nucleation.

After the addition of SMase, we observed that the heterogeneity induced by SMase is confined in each of the corrals and each corralled membrane shows quite consistent morphology change (Figures 2-9(b, c)). However, large-scale heterogeneity was observed in conventionally-formed membranes after the addition of SMase (Figures 2-9(e, f)). Since previous literature has reported that SMase has a high binding constant to its substrate and dissociates from the lipid membrane very slowly [126,127], the distance between the location of a region of a membrane and where the SMase is added would influence the initial condition of how much SMase binds to that region. The large-scale heterogeneity could be attributed to the non-uniform distribution of SMase, which is difficult to prevent in a manual addition but can be handled more easily by the controlled flow in a microchannel. The more uniform initial condition of membrane morphology and SMase distribution allows us to obtain consistent results from area to area. The fixed controlled flow conditions also allow more robust results from sample to sample, which is important for us to correlate time evolution results to other characterization results. In addition, in a confined membrane, we can interpret the SMase-induced phase phenomena easily without

considering which size and location of a region in a heterogeneous membrane is representative to describe the phase behavior.

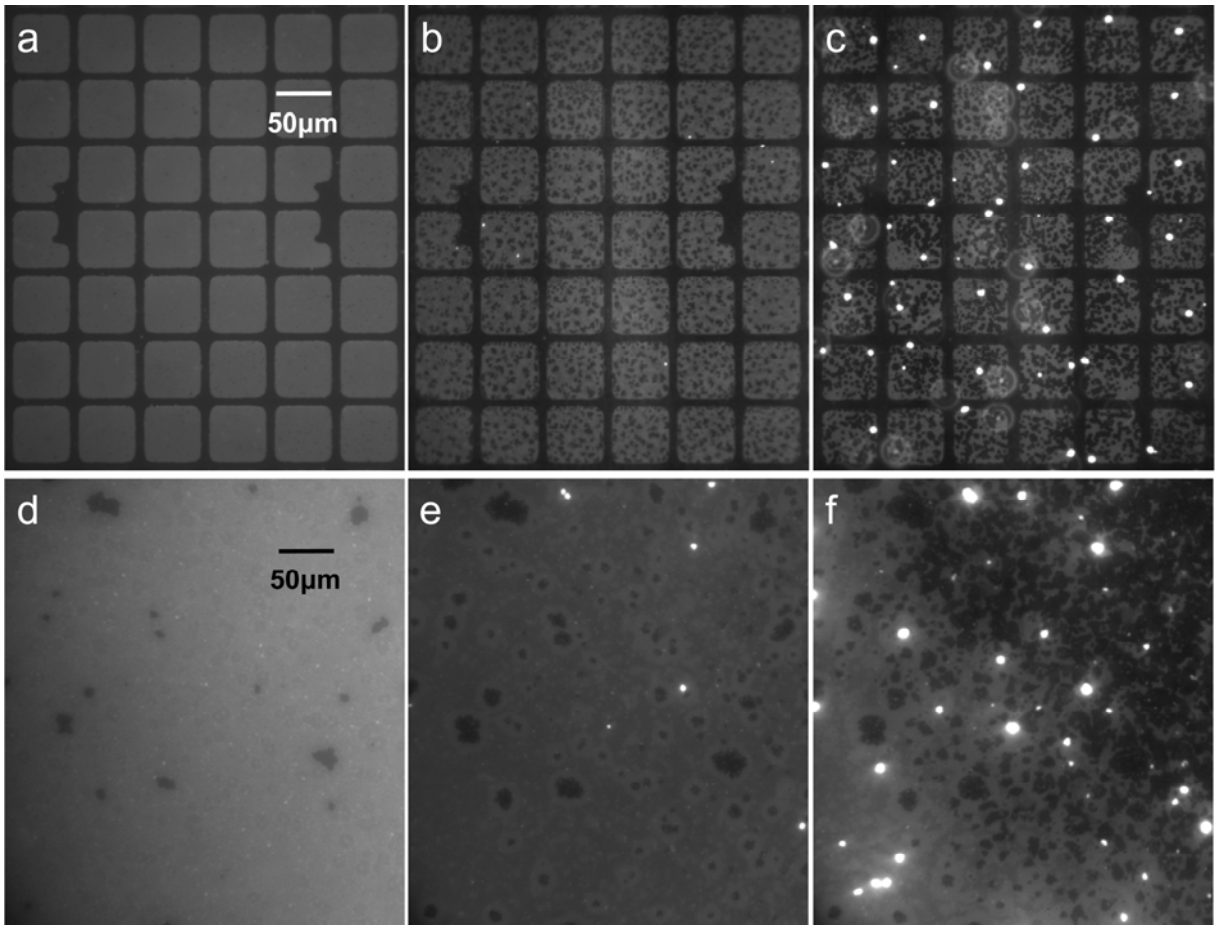

Figure 2-9. Corralled membranes in a microfluidic device for studying membrane morphology changes induced by SMase. (a), (b), and (c) are images taken in the corralled membrane system before the addition of SMase, at about 20 min after the addition, and at about 90 min after the addition, respectively. (c), (d), and (e) show the performance of the non-corralled membrane prepared by a conventional incubation/washing method and affected by the manually added SMase. The images were taken at similar times to those in (a), (b), and (c), respectively. Both membrane systems are composed of 40/40/20 molar ratio of DOPC/SM/Chol and incorporated

with 0.5% mol of Texas-Red® DHPE to image the morphology changes. 0.005 unit/ml SMase was used and the experiments were performed at room temperature.

2.6. Numerous systems in parallel to capture the stochastic nature of domain nucleation

As we will show in chapter 3 and 5, the overall phase change induced by SMase is composed of several nucleation and growth events of new domains. The stochastic nature of the nucleation sometimes makes it difficult to quantify and compare the membrane responses caused by different factors. Many repeated experiments or many systems with the same conditions would be required to statistically describe the domain nucleation.

In most of our systems, we observed a slowly-nucleating feature rich in SMase, sphingomyelin (the SMase's substrate), and ceramide (the SMase's product). The slow nucleation rate causes the feature to have a wide distribution of induction time. We used the SLB arrays to capture the distribution of the induction time of SMase-features in a single set of experiment. Figure 2-10 shows the images taken when only a few SMase-features had nucleated, when SMase-features had already nucleated in half of the corrals, and when SMase-features had nucleated in all of the forty-nine corralled membrane systems. Figure 2-11 illustrates how the number of corrals with SMase-features changed with time in a set of experiments. Each line is from three sets of forty-nine-corral experiments with the same composition. The four lines represent the four different membrane compositions. Obtaining the distribution instead of single data points allowed us to compare the effects caused by different membrane compositions and SMase concentrations. The more complete analysis and discussion are in Chapter 5.

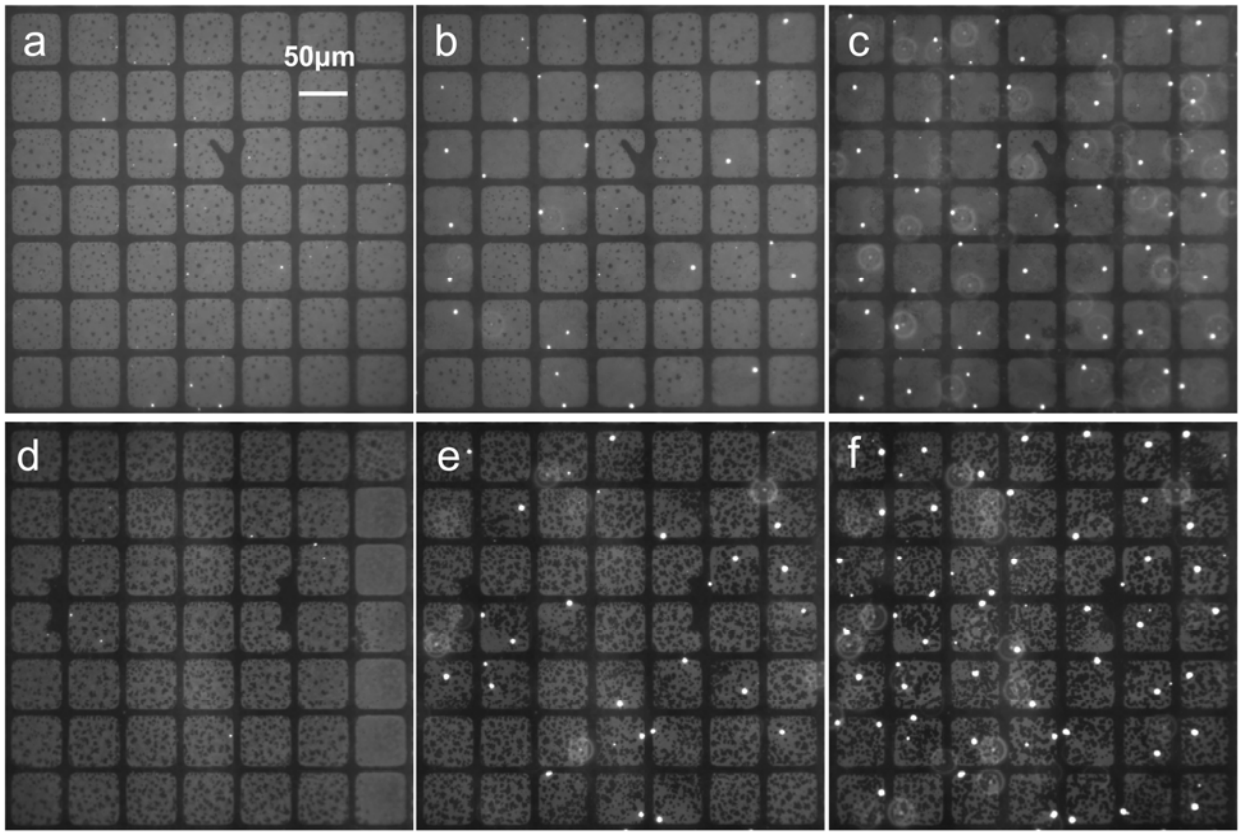

Figure 2-10. Forty-nine 50 μm x 50 μm membranes separated by corrals in a single set of experiment. The large number of membrane systems allows us to quantify and compare the phenomena in membranes with different conditions, whose difficulty is the large variation of the SMase-feature nucleation time as demonstrated in Figure 2-11. (a)(b)(c) are the images taken in 60/20/20 DOPC/SM/Chol membranes when only a few SMase-features had nucleated, when SMase-features had already nucleated in half of the corrals, and when SMase-features had nucleated in all of the forty-nine corralled membrane systems, respectively. (d)(e)(f) are the images taken in 40/40/20 DOPC/SM/Chol membranes. The bright rings in the images are the diffraction patterns from the SMase-features on the opposite surface of the 50μm height microchannel and can be ignored.

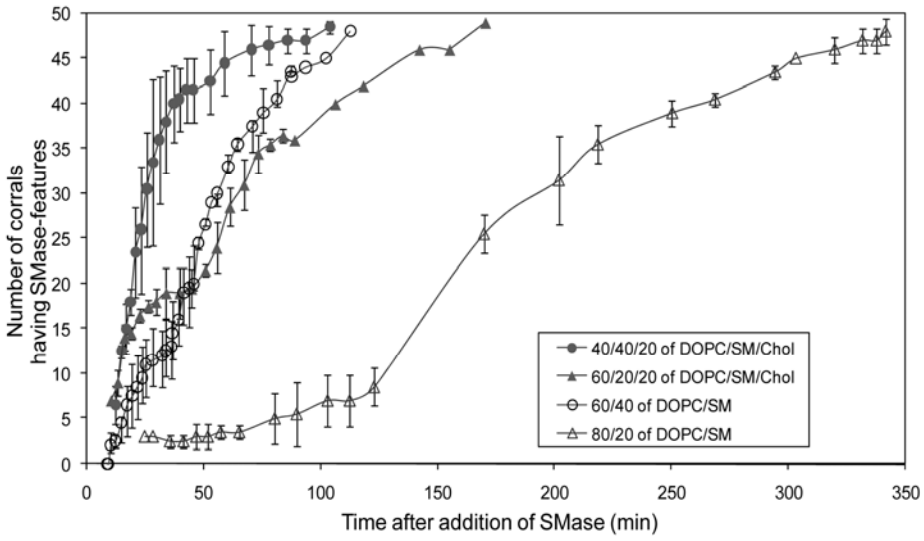

Figure 2-11. How the number of corrals having SMase-features changes with time in a set of experiment with forty-nine corrals. Each line is from three sets of forty-nine-corral experiments with the same composition. The four lines represent the four different compositions.

2.7. Laminar flows to generate membrane arrays with various compositions and solution conditions

Laminar flow occurs when the Reynolds number (Re) of a flow system is much less than one (the Reynolds number represents a ratio of inertial to viscous forces acting on a fluid element and is defined as $Re = \rho UL/\mu$, where ρ is the fluid density, U is the average velocity, L is a characteristic length for the system, and μ is the fluid viscosity). The flow in a microfluidic device with micron-sized channel can be easily operated at the conditions allowing $Re \ll 1$. In a laminar flow configuration, the molecules follow their streamlines and the mixing is limited by their inter-diffusion.

We utilized the laminar flow to create gradients with multiple components through the multiple microfluidic inlet streams. In a laminar flow configuration, the mixing of adjacent streams is limited by their inter-diffusion. The relative concentrations of different components vary gradually and continuously over a transitional mixing region at the interfaces between the flows. Ideally, the gradient can be controlled by flow parameters related to the ratio of axial flow rate and lateral diffusion rate (or called the Peclet number=UL/D, where U is the average velocity, L is a characteristic length for the system, and D is the diffusivity of the diffusing molecule). In addition, the flow gradient can be estimated by solving the diffusion equations under some appropriate assumptions.

Following the rationale, we can construct the gradient of small lipid vesicle solutions with various compositions during the formation of supported lipid bilayers. During the bilayer formation by vesicle deposition, the initial contact and sticking of vesicles to a surface is irreversible. As a consequence, whatever composition of vesicles approaches the surface is captured by the surface. Once the lipid membrane is captured by the surface, it is confined in its own corral. This process yields spatially varying composition in different corrals. Similarly, we can also construct spatially varying reaction conditions (such as enzyme concentration, and ionic strength) over different corrals after the corralled membranes form.

Figure 2-12 demonstrates an example in which five lipid vesicle solutions with different composition were flowed into the main channel. The flow was implemented by withdrawing the fluid through a syringe pump since withdrawing has shown to give better flow stability than

infusing. The main channel is 500 um wide and 50 um high, and the average flow rate is 5 μl/min. Water's density and viscosity are used as those of the dilute solutions. The calculated Re is 0.167, indicating that the flows are in laminar flow configuration. The laminar flow configuration can be visualized by using streams with different amount of fluorescent dyes into the same channel, as shown in the lower middle picture in Figure 2-3.

We can further calculate the Peclet number to check the relative ratio of axial flow rate and lateral diffusion rate in the system. The diffusion coefficients of vesicles can be estimated by the Stokes-Einstein Relation, $D=K_BT/3\pi\eta d$, where d is hydrodynamic diameter, K_B is Boltzman constant, T is temperature, and D is translational diffusion constant. For a 80nm vesicle, the estimated diffusion coefficient in water is $2.8x10^{-12}$ m^2/s. The Peclet number (Pe= UL/D) is 11745 if we use the width of each stream(~100 μm) as the characteristic length (L). The large Pe indicates that the inter-mixing of components between the streams is very minor, and thereby the composition of the lipid membrane in a corral is probably very close to the composition of the prepared lipid vesicles in the stream above the corral. The more obvious gradient or mixing can be achieved by decreasing the flow rate, using a longer channel, and observing the gradient at further downstream regions. For example, if we control the flow at 0.1 μl/min in a 50μm x 500 μm channel, the Pe would be around 200. An obvious gradient would be observed at the end of a channel with 2 cm length (200 times of the width of each stream).

After the formation of corralled lipid membranes with various compositions, uniform 0.005 unit/ml SMase solutions were flowed into the main channel in order to observe the domain dynamics caused by SMase. Figure 2-12 clearly shows that the corralled membranes with

different compositions have different domain morphology after they were exposed to the same SMase solutions. The results demonstrate that condition variations among corrals on a single platform is doable and can be a screening tool to study a broad range of parameters associated with the interactions between lipid membranes and peripheral proteins.

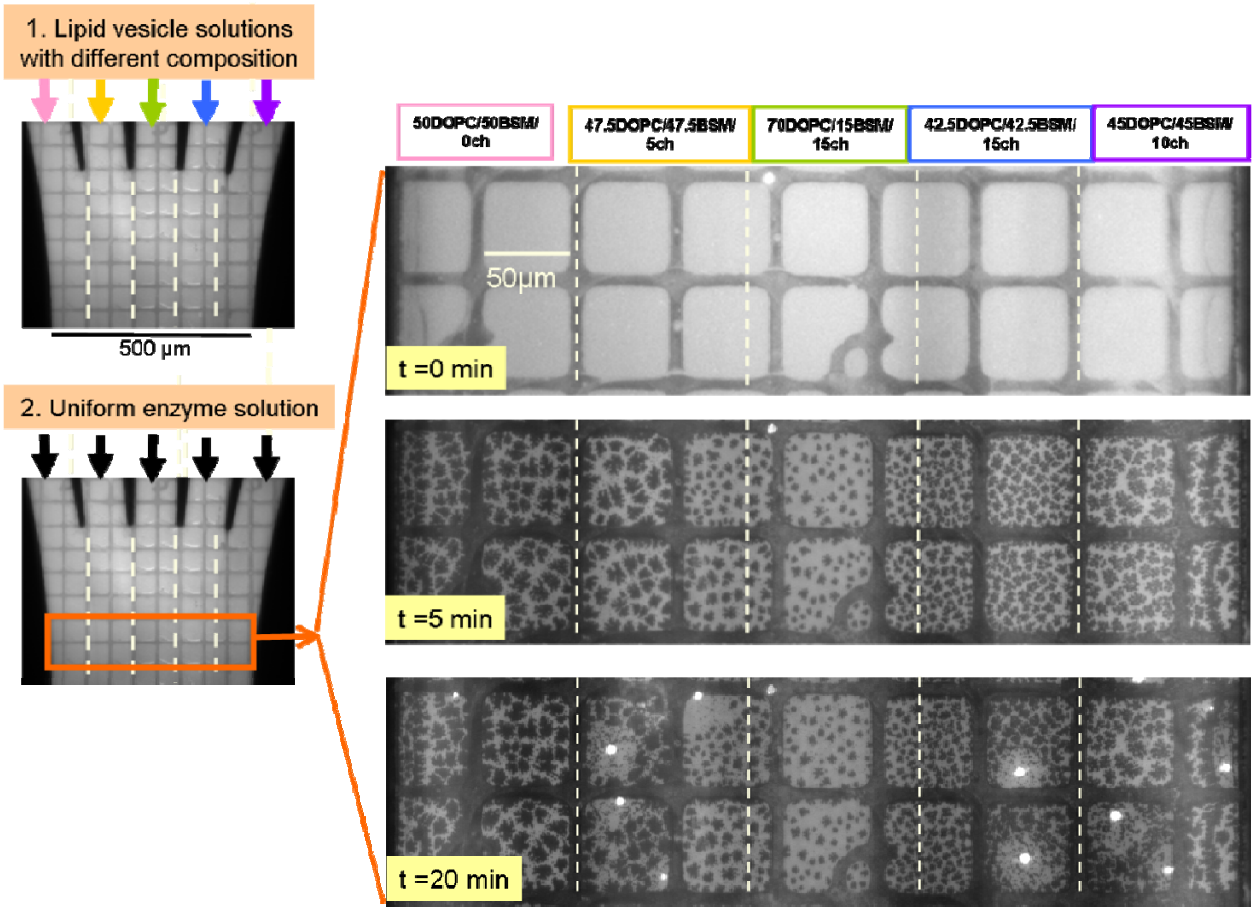

Figure 2-12. An example showing how the corralled membranes in a microfluidic channel can be a screening tool. The composition variation was constructed first in this case. Later, the morphology evolution can be observed under a fluorescence microscope easily after SMase was uniformly distributed to the SLB array with composition variation.

Chapter 3. Sphingomyelinase-induced phase transformations: causing morphology switches and multiple-time-domain ceramide generation in model raft membranes

3.1. Introduction

As we have introduced in chapter 1, sphingomyelinase (SMase) in cell membranes has been reported to be involved in a variety of cell regulation processes, particularly in programmed cell death (apoptosis)[13,17,19,21-23]. Both biophysical data on ceramide[65,128-132] and evidence from physiological studies[28,35,38] have suggested that the SMase influences the cellular processes by altering the phase dynamics in the membrane.[38] In the early stage or induction phase of apoptosis, large lipid membrane platforms with clustered receptors have been observed in cells in a few minutes after SMase is activated. The large platforms are thought to help concentrate and thereby cluster the required membrane receptors, while the clustering has been found to be an essential step for those receptors to trigger their subsequent cellular pathways.[57] In the late stage or the execution phase of apoptosis, the negative spontaneous curvature induced by ceramide in the membrane has been suggested to facilitate the membrane blebbing or apoptotic body formation.[58,59]

Many biophysical studies have incorporated ceramide *ex situ* into model raft membranes in order to further understand the underlying mechanism of the lipid membrane phase change due to the compositional change caused by SMase. Some bulk assay studies using a fluorescence multiprobe and multiparameter approach have shown that ceramide can not only form ceramide-enriched domains but can also recruit sphingomyelin to form sphingomyelin-enriched domains in lipid bilayers with model raft compositions.[133,134] Recent atomic force microscopy (AFM) studies have also demonstrated the two different domains corresponding to those mentioned above.[73,74] However, most of the analyses were done in the absence of SMase.

In fact, some studies have suggested that SMase may play other roles besides causing the compositional change of lipid membranes. Studies on pure sphingomyelin monolayers have shown that ceramide generated by SMase *in situ* can induce pattern formation in membrane domains which cannot be achieved by incorporating ceramide *ex situ*[64,72] Recently, in model raft membranes, Johnston et al. and Chiantia et al. have used atomic force microscopy (AFM) to demonstrate that SMase can induce topographical features more complex than those generated by incorporating ceramide *ex situ*.[73,74] However, the AFM studies have difficulty recording the kinetic processes of morphology changes in the presence of SMase because of tip contamination problems, and have not been able to identify how SMase is involved in the complex phase changes. Although some studies have used fluorescence microscopy to record the real-time morphology changes in the presence of SMase, only early time changes have been reported.[75,76] The complex heterogeneity, varying from region to region and sample to sample, also makes the characterization difficult.

In order to study whether and how the SMase is involved in the phase changes, we constructed a well-controlled model membrane system in a microfluidic channel and used multiple labeling approaches to identify where SMase binds and the major components of the different phases. The planar surface of supported lipid bilayers (SLBs) provides a good platform for the easy tracking of membrane domains. The SLBs were confined to corrals as described in chapter 2 in order to provide control of the mass balance of lipid molecules during the surface enzymatic reaction. The controlled flow in a microfluidic device primarily provides two advantages for the study in this chapter. First, it provides a more robust preparation of SLBs. Second, the control and uniform addition of SMase is essential for obtaining physiologically relevant and robust results because of its high binding constant to its substrate and slow dissociation from the lipid membrane [126,127]. Non-uniform initial conditions may contribute to the later membrane morphology heterogeneity and cause difficulty in interpreting the results.

The results in this chapter show that the overall morphology change can be generalized into three stationary morphology stages separated by two transition stages in model raft membranes. The real-time evolution of morphology over the biologically relevant time scale is imaged by Texas-Red® DHPE, a fluorescent lipid probe. These lipid probe images are taken as references to correlate the characterization results of observed features. With the help of antibodies and labeled SMase, we identify the two transition stages as a reaction-induced and a solvent-mediated phase transformation. More importantly, we observe a 3-D structure rich in SMase, sphingomyelin, and ceramide, and the nucleation of this feature triggers the solvent-mediated phase transformation. The multi-stage morphology evolution is shown to be caused not only by

the phase change due to compositional changes, but also by the selective binding of the enzyme to different phases, the accessibility and replenishment of the substrate in different phases, and the enzyme's special phase behavior.

3.2. Materials and Methods

3.2.1. Materials.

1,2-Dioleoyl-*sn*-glycero-3-phosphocholine (DOPC), 1-Palmitoyl-2-Oleoyl-*sn*-Glycero-3-Phosphocholine (POPC), cholesterol (Chol), brain sphingomyelin (BSM), and egg sphingomyelin (ESM), were purchased from Avanti Polar Lipids (Alabaster, AL). Texas-Red®1,2-dihexadecanoyl-*sn*-glycero-3 phosphoethanolamine triethylammonium salt (Texas-Red® DHPE), 1,1'-didodecyl-3,3,3',3'-tetramethylindocarbocyanine perchlorate ('DiI'; $DiIC_{12}(3)$), Alexa Fluor® 488 Microscale Protein Labeling Kit, Alexa Fluor® 488 goat anti-rabbit IgG, and Alexa Fluor® 488 goat anti-mouse IgM (μ chain) were purchased from Invitrogen (Eugene, OR). Lysenin antiserum was purchased from Peptides International, Inc. (**Louisville, KY**). Sphingomyelinase from *Bacillus cereus* and all other reagents, unless otherwise specified, were purchased from Sigma (St. Louis, MO). The PBS buffer in this paper is 0.01 M phosphate buffered saline (138 mM NaCl/ 27 mM KCl, pH 7.4).

3.2.2. Preparation of small unilamellar vesicles (SUVs)

Small unilamellar vesicles (SUVs) were prepared for the vesicle deposition to form supported lipid bilayers (SLBs). SUVs were formed by extrusion where dried lipids were reconstituted in the buffer (10 mM HEPES, 2 mM $CaCl_2$, and 100 mM NaCl, PH=7.4) at a concentration of 2 mg/mL and then passed 19 times through an 80-nm polycarbonate filter in an Avanti Mini-Extruder (Alabaster, AL). The stock SUV solutions were stored at 4˚C for up to one week before being used. The stock solutions were diluted to 0.2 mg/mL just before use in the vesicle deposition.

3.2.3. Preparation of supported lipid bilayers on a glass coverslip

Glass coverslips were cleaned by argon plasma for 10 min. The prepared SUV solutions were heated to a temperature above the miscibility transition temperature of the lipid mixture and were added to the coverslips which had been already placed on a hot plate at the same temperature. The coverslips were incubated with the SUV solutions for 30 min and rinsed extensively with water at the same temperature.

3.2.4. Preparation of corralled supported lipid bilayers in a microfluidic device

The protein micro-contact printing developed by Kung et al.[135] was used to construct supported lipid bilayer systems in separate corrals. By controlling the size and shape of the printed corrals, we can construct lipid membranes with controllable amount and position. We fabricated the polydimethylsiloxane (PDMS) stamp with 50 μm x 50 μm corral configuration and used it to

print bovine serum albumin (BSA) (250 μg/ml) to the clean glass coverslips cleaned by argon plasma for 10 min before the printing. The patterned glass coverslips were later sealed with PDMS microchannel slabs. The device with a patterned surface was used immediately or stored under water for up to one day prior to use. The prepared SUV solutions were flowed into the microchannel and the SUVs deposited on the glass surfaces that were devoid of protein. Later, water was flowed into the channel to wash away the non-specifically bound vesicles. The deposition process was performed at a temperature above the miscibility transition temperature of the lipid mixture in a temperature-controlled water bath. The corralled membranes were stored in water at room temperature and used within two days of preparation. The membranes were heated to and kept at 37˚C for 20 minutes before use.

3.2.5. Conjugation of Sphingomyelinase with Alexa Fluor ®488 Dye

Conjugation of Sphingomyelinase from *Bacillus cereus* (Sigma, St. Louis, MO) with Alexa Fluor® 488 dye was performed by using the Alexa Fluor®488 microscale protein labeling kit from Invitrogen (Eugene, OR). The SMase as received was reconstituted to 1mg/ml and dialyzed for 3 hrs in the HEPES buffer (10mM HEPES/ 100mM NaCl/ 2 mM $MgCl_2$) at 25 °C. About 4.5 μL of 11.3 nmol/ml reactive Alexa Fluor 488 dye was used to label 31.4 μg of SMase in the HPEPS buffer. Excessive dye was removed using a spin column with Bio-Gel P-6 fine resin.

3.2.6. Characterization by immunostaining

After the SMase in the SLB system was washed extensively with PBS buffer, we used anti-ceramide antibody to stain the ceramide and lysenin to stain the sphingomyelin in the system. 5 μg/ml monoclonal anti-ceramide antibody produced in mouse (clone MID 15B4) (Sigma, St. Louis, MO) in a PBS buffer was flowed into the channel and incubated with the lipid membrane for 20 min followed by a PBS buffer wash. After the wash, 10 μg/ml labeled secondary antibody, Alexa Fluor® 488 goat anti-mouse IgM (μ chain) (Invitrogen, Eugene, OR), was flowed into the channel and incubated with the system for another 20 min followed by another PBS buffer wash. We used the same incubation/wash procedure to detect the localization of the sphingomyelin. 10 μg/ml of lysenin, a sphingomyelin-specific binding protein, was introduced to the membrane and the excess protein was washed away. The staining procedure was followed by using lysenin antiserum from rabbit (diluted 1/1000 with PBS) and 20 μg/ml Alexa Fluor® 647 goat anti-rabbit IgG as labeled secondary antibodies. For the double staining of both ceramide and sphingomyelin as shown in Figure 3-6, anti-ceramide antibody and lysenin were mixed together before flowed into the channel while kept at the concentration mentioned above. Second, Alexa Fluor® 488 goat anti-mouse IgM and lysenin antiserum were flowed into the channel together and washed. Finally, Alexa Fluor® 647 goat anti-rabbit IgG was flowed into the channel alone. The doubling staining was compared with the single staining for either ceramide or sphingomyelin, and no significant cross reactivity between these two sets of primary/secondary antibodies was shown (Figure 3-9). After the staining process, we used fluorescence microscopy to locate the labeled antibody complex on the membrane surface.

3.2.7. Images by fluorescence microscopy

The morphology evolution images were observed using a Nikon TE2000-E inverted microscope with a Nikon CF DL 20X objective and a Plan Neofluar 100X/1.30 oil immersion objective. Temperature control of the samples was accomplished by a microscope heating stage unit (Instec, Boulder, CO) and an objective collar heater (Bioptechs, Butler, PA). Experiments were performed at 37°C unless otherwise specified.

Fluorescence confocal microscopy experiments were performed with a Zeiss laser scanning module (LSM) microscope with a Plan-Apochromat 63X/1.4 oil immersion objective. For a three-channel experiment, the excitation light from lasers at 633, 543 and 488 nm. The emission was split by two dichroic mirrors (NFT 635 and NFT 545) and one filter (BP 505-530) to detect the Alexa Fluor® 647, Texas-Red® DHPE, and Alexa Fluor® 488.

3.2.8. Image processing

The fractional area of the dark region in the florescence image was calculated with Matlab software (Mathworks Inc., Natick, MA). The defined dark region was delineated by an image processing routine to ensure the same standard for all of the images in the morphology evolution. In short, this routine can first eliminate the uneven background from inevitable uneven illumination based on two morphological operators, erosion and dilation.[136] After removing the uneven illumination, we can accurately define the region by Otsu's threshold method[137], and calculate the area ratio by the defined region. Figure 3-1 shows that elimination of the uneven background is necessary for obtaining an accurate description of the domain ratio in an image.

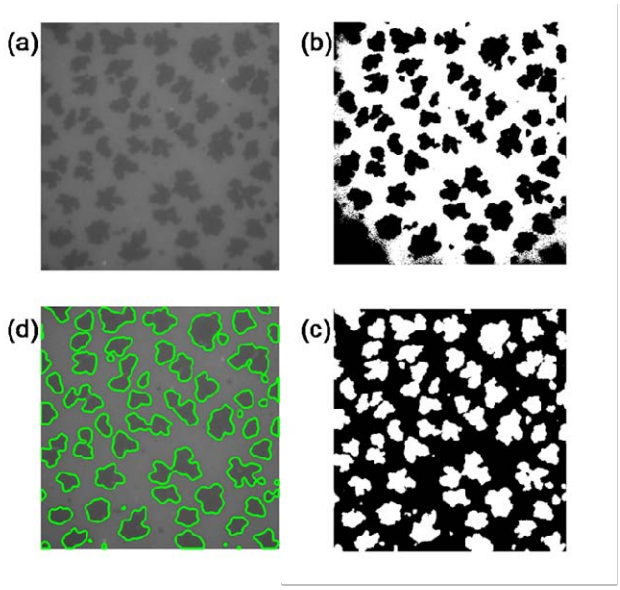

Figure 3-1. Performance of the image processing routine. (a) shows an original image; (b) shows the region obtained by applying Otsu's threshold method directly to the original image. The dark region at the corners is caused by the uneven illumination; (c) shows the region obtained by applying Otsu's threshold method after the uneven illumination is eliminated; (d) shows the superimposition of the borderlines of (c) to the original image, which indicates that our image processing routine can accurately describe the domain morphology.

3.3. Results

3.3.1. Spatial morphology change with stages induced by sphingomyelinase

3.3.1.1. Detailed morphology evolution in a single corralled membrane system

We formed 50 μm x 50 μm corralled model membranes in a microfluidic device. The flow conditions of lipid vesicle solutions and washing solutions during the formation of supported lipid bilayers were controlled to be the same for every experiment in order to achieve a more robust preparation of supported lipid bilayers. After the corralled membrane systems formed, the flow in a microfluidic channel was controlled to allow the lipid membrane to be exposed to 0.005 unit/ml Sphingomyelinase (SMase) from *Bacillus cereus* for 2 minutes at room temperature. 0.5 mol% Texas-Red® DHPE, a phospholipid with Texas-Red® dye-labeled headgroup, was incorporated into lipid membrane systems to reveal the morphology change.

Figure 3-2(a) shows a detailed morphology evolution of the morphology change induced by 0.005 unit/ml SMase at 37°C in a single 50 μm x 50 μm corralled membrane. 40/40/20 molar ratio of 1,2-Dioleoyl-sn-glycero-3-phosphocholine (DOPC)/ brain sphingomyelin (BSM)/ cholesterol (Chol) incorporated with 0.5 mol% of Texas-Red® DHPE is used in this experiment. To further illustrate morphological change over time, the morphology evolution images were processed with Matlab and the corresponding fractional areas of the dark region were used to plot Figure 3-2(b). Before the addition of SMase (t= 0), the lipid membrane had small gray blurred pre-existing domains, assumed to be sphingomyelin and cholesterol enriched domains, based on previous phase studies of model raft membranes [5,138]. The bright patches were probably the non-specifically bound small vesicles and most of them were washed away after the SMase solution was introduced to the surface. After the addition of SMase, the pre-existing rafts faded

away, and some dark domains started to grow quickly for a few minutes. Later, the morphology change paused. The pause morphology started to reorganize after a bright feature appeared (about 20 min after the addition of SMase). In this reorganization stage after the bright feature formed, the dark domains revealed by Texas-Red® DHPE can be distinguished into two different types: one type started to dissolve in a direction away from the bright feature (indicated by dashed diamond in Figure 3-2(a)); in contrast, the other type started to grow (indicated by dashed box in Figure 3-2(a)). Eventually, all of the dissolvable domains dissolved and all of the other type domains grew to their full size. The final constant morphology lasted for days.

According to the characteristics of the domain morphology change, the morphology evolution after the addition of SMase can be divided into four stages: (A) formation of two types of dark domains; (B) a pause morphology; (C) dissolution of one type of dark domain, and growth of the other type after the formation of bright features; (D) a final stationary morphology.

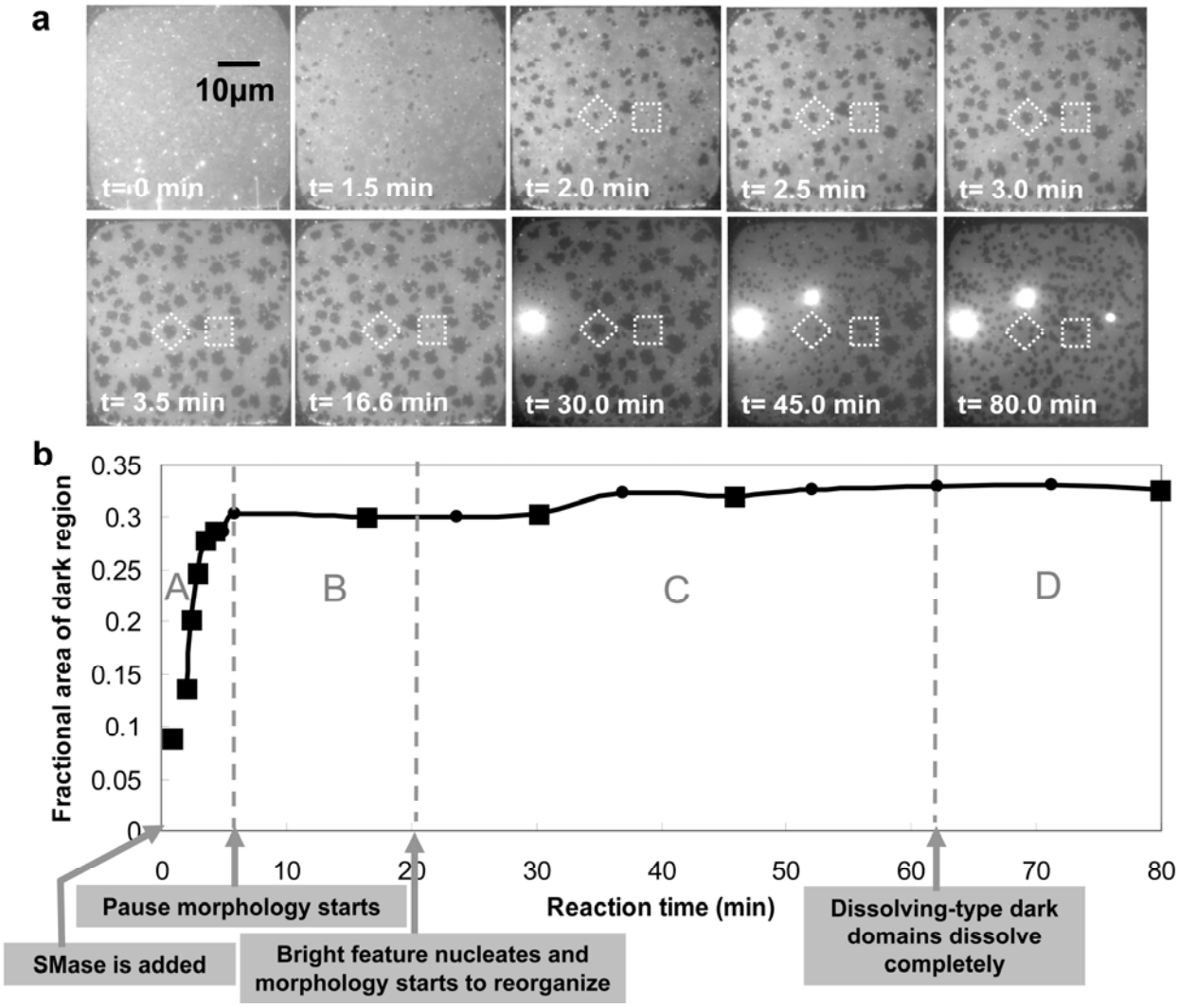

Figure 3-2. (a) Morphology evolution images after the 40/40/20 DOPC/BSM/Chol Texas-Red® DHPE-stained membrane in a 50 μm x 50 μm corral was treated with 0.005 unit/ml SMase at 37ºC. White dashed diamond indicates the dark domains which dissolved after the bright feature formed; white dashed box indicates the dark domains which grew after the bright feature formed. (b) The graph illustrates how the fractional area of the overall dark region changed with time. The data points denoted with closed rectangles have their corresponding images in (a). The morphology evolution is described by four stages labeled as A, B, C, and D.

3.3.1.2. Comparable morphology evolution in model raft membranes with various compositions

We also observed the morphology evolution with these stages in model membranes with different ratios of unsaturated phospholipid/SM/Chol or different types of SM and unsaturated phospholipid (Figure 3-3). In every of the membrane systems we tested, dark domains formed quickly in minutes and a pause morphology was reached. Although all of these systems had dark domains with different sizes and shapes in their pause morphologies, we observed that the pause situation was always followed by the formation of bright features. In addition, two types of domains can be always distinguished: one type of dark domain dissolved and the other grew after the bright feature appeared. In the membrane systems with brain sphingomyelin, we noticed that those dissolving-type dark domains have sizes of few microns, and those growing-type domains are much smaller (Figure 3-3(a, b, c)). Sometimes the growing-type domains even cannot be resolved in the pause morphology (Figure 3-3(a), stage B) and can be observed after they started to grow after the bright feature occurs (Figure 3-3(a), stage C and D). In contrast, in the membrane systems with egg sphingomyelin, those dissolving-type domains are much smaller (around 1 μm). Their growing-type domains at the pause morphology are even larger than their dissolving-type domains and can grow to sizes of few microns in the final stage (Figure 3-3(d, e)). One thing to notice is that these stages also occur in the membrane system without cholesterol (Figure 3-3(c)). We did observe that the absence of cholesterol can delay the appearing time of the bright features (or the time for stage C to start), and the related work is shown in chapter 5.

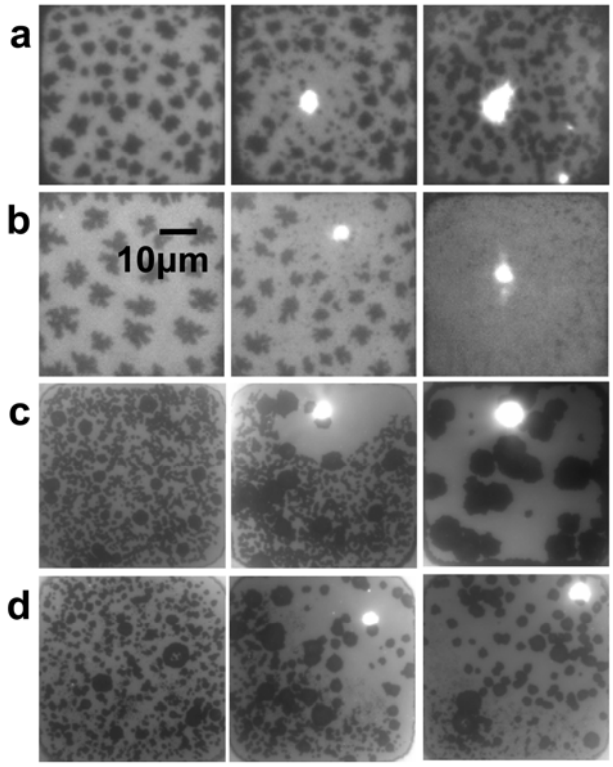

Figure 3-3. Morphology evolution with stages induced by SMase occurs in other Texas-Red® DHPE-stained model raft membrane systems: (a) 60/40/0 DOPC/BSM(brain sphingomyelin) /Chol; (b) 70/15/15 DOPC/BSM/Chol; (c) 40/40/20 DOPC/ESM(egg sphingomyelin)/Chol; (d) 40/40/20 POPC(1-Palmitoyl-2-Oleoyl-*sn*-Glycero-3-Phosphocholine)/ESM/ Chol . All of them have two types of dark domains and bright features. One type dissolved and the other grew after the formation of the bright features. Images were taken during their pause morphology (stage B), when one type dark domains dissolved and the other grew (stage C), and the final stage (stage D).

3.3.1.3. Control experiments with no observable stages

In the control experiment, no morphology change was observed in membranes with only DOPC up to one day (Figure 3-4(b)). In addition, we did not observe these stages but only observed continuous spatial morphology changes in membranes with only BSM (Figure 3-4(a)). The darkness indicates the conversion of BSM to ceramide, which was confirmed by using anti-ceramide to test the composition. The result suggests that the stages associated with changing stationary spatial morphologies not only requires the substrate of SMase but may also require a DOPC-enriched fluid phase to facilitate the phase transformation.

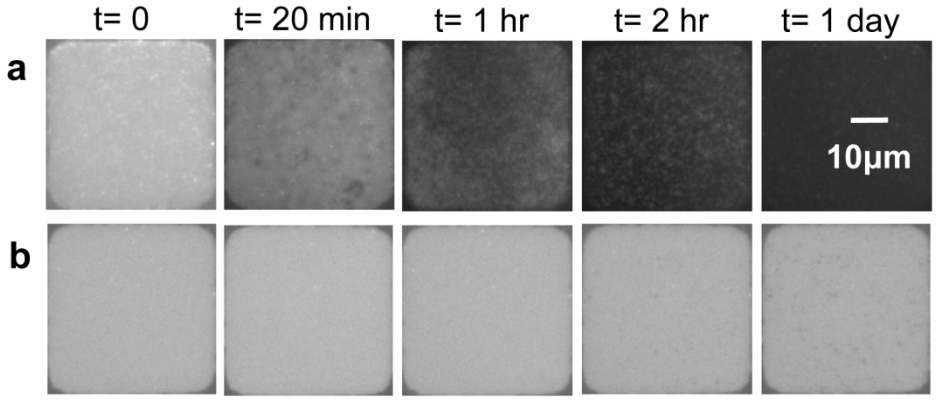

Figure 3-4. Control experiments following the evolution of model membranes with (a) pure BSM and (b) pure DOPC after they were treated with 0.005 unit/ml SMase at 37ºC. 0.5mol%Texas-Red® DHPE was incorporated to both membrane systems.

3.3.1.4. Observed features are not artifacts associated with the fluorescent lipid probe

The pre-added fluorescence lipid probe, Texas-Red® DHPE allows real time observation of the evolution of the lipid membrane morphology; however, the probe could influence membrane phase behaviors. To further ensure that the morphological evolution and the corresponding features are not artifacts introduced by the fluorescence probe, we compared systems imaged with pre-added lipid probe (Texas-Red® DHPE) with those imaged by the intercalating dye (1,1'-didodecyl-3,3,3',3'-tetramethylindocarbocyanine perchlorate ($DiIC_{12}(3)$)) added after the SMase reaction. The addition of intercalating dye after the reaction has proceeded to a particular time point reveals the spatial morphology change in an unperturbed SMase-lipid membrane system. Figure 3-5(a) is a typical Texas-Red® DHPE image we obtained when the SMase reaction proceeded to stage C. We treated the membrane without any Texas-Red® DHPE under the same conditions, and when the reaction proceeded to the time corresponding to stage C, we added $DiIC_{12}(3)$ to the system to stain the features (Figure 3-5(b)). As shown in Figure 4(b), $DiIC_{12}(3)$ can also distinguish three different features whose sizes and relative locations correspond well to the features observed in Texas-Red® DHPE images although $DiIC_{12}(3)$ is shown to have different staining preference for the various features. As shown by the B line in Figure 3-5, $DiIC_{12}(3)$ happens to also preferentially stain the bright feature defined in Texas-Red® DHPE images. Both of the dark domains defined in Texas-Red® DHPE images are actually lighter than the background phase in $DiIC_{12}(3)$ images (indicated by the S line and the L line).

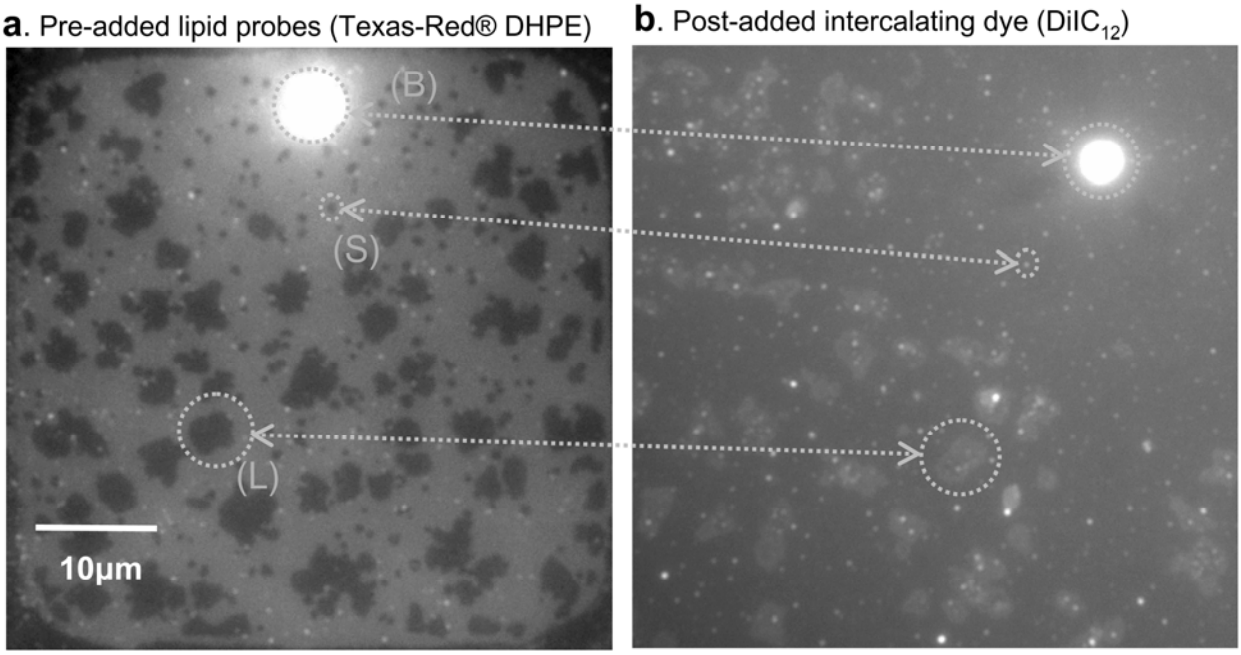

Figure 3-5. Corresponding features observed in membrane systems with (a) pre-added lipid probes (Texas-Red® DHPE) and with (b) addition of the dye (DiIC12) after the reaction. Line (B) indicates the bright feature; line (S) indicates the smaller dark domains; line (L) indicates the larger dark domains as defined in the Texas-Red® DHPE image. The different relative fluorescence intensities of the features are due to the different staining properties of the two probes. Both membrane systems are composed of 40/40/20 molar ratio of DOPC/BSM/Chol and treated with 0.005 unit/ml SMase**.**

3.3.2. Identification of the major components of membrane domains by antibodies

Since Texas-Red® DHPE provided the real-time information but not the composition or the identity of the domains, the identification of the domains at each stage in the morphology evolution is critical for the interpretation of the complex phase behavior. To further identify and

characterize membrane domains, we stained the ceramide in the membrane with anti-ceramide and the sphingomyelin with lysenin, a sphingomyelin-specific binding protein [139-141].

3.3.2.1. Double-labeling of SM and Cer in lipid probe-stained membranes

When the reactions in a Texas-Red® DHPE-stained membrane proceeded to stages B, C, or D, both Alexa Fluor® 488-labeled anti-ceramide antibody complexes and Alexa Fluor® 647-labeled lysenin antibody complexes were added to the membrane. The images obtained under a three-channel confocal microscope (Figure 3-6(a); images before being superimposed are in Figures 3-6) show that the dark domains dissolving after the bright feature forms are sphingomyelin-enriched domains (SM-enriched domains) and that those domains growing after the bright feature forms are ceramide-enriched domains (Cer-enriched domains). In stage B, both SM-enriched domains and Cer-enriched domains exist. In stage C, those SM-enriched domains close to the bright feature (indicated by the gray circle) disappear and the overall intensity from anti-ceramide antibody complexes is higher than the intensity in stage B. In stage D, only Cer-enriched domains can be significantly observed. Before the addition of SMase, only lysenin, but no anti-ceramide, binds to the membrane significantly, which shows there is no non-specific binding of anti-ceramide to the model raft membranes. Lysenin seems to bind to the whole membrane, but not uniformly. This observation is probably due to the existence of the small pre-existing domains rich in sphingomyelin and cholesterol which could not be resolved well by the microscope.

3.3.2.2. Double-labeling of SM and Cer in the absence of lipid probes

In order to ensure that the Texas-Red® lipid probe does not influence the qualitative interpretation, and to rule out the possibility of energy transfer between the three fluorescence dyes, we also apply the antibody characterization to the membranes in the absence of Texas-Red® lipid probes (Figure 3-6(b); images before being superimposed are in Figures 3-7). Alexa Fluor® 488-labeled anti-ceramide antibody complexes and Alexa Fluor® 647-labeled lysenin were used. According to the emission and excitation specta of Alexa Fluor® 488 and Alexa Fluor® 647, no significant energy transfer can occur between these two dyes. The results are very similar to those obtained in Texas-Red® DHPE-stained membranes. In fact, without the lipid probe, the distribution of Cer-enriched domains seems to be more uniform, and how sphingomyelin is transformed to ceramide can be more easily seen. More importantly, we clearly observed that both anti-ceramide and lysenin antibody complexes bind to the feature corresponding to the bright feature shown in the Texas-Red DHPE images in the absence of the lipid probe's interference, indicating the feature contains both SM and Cer.

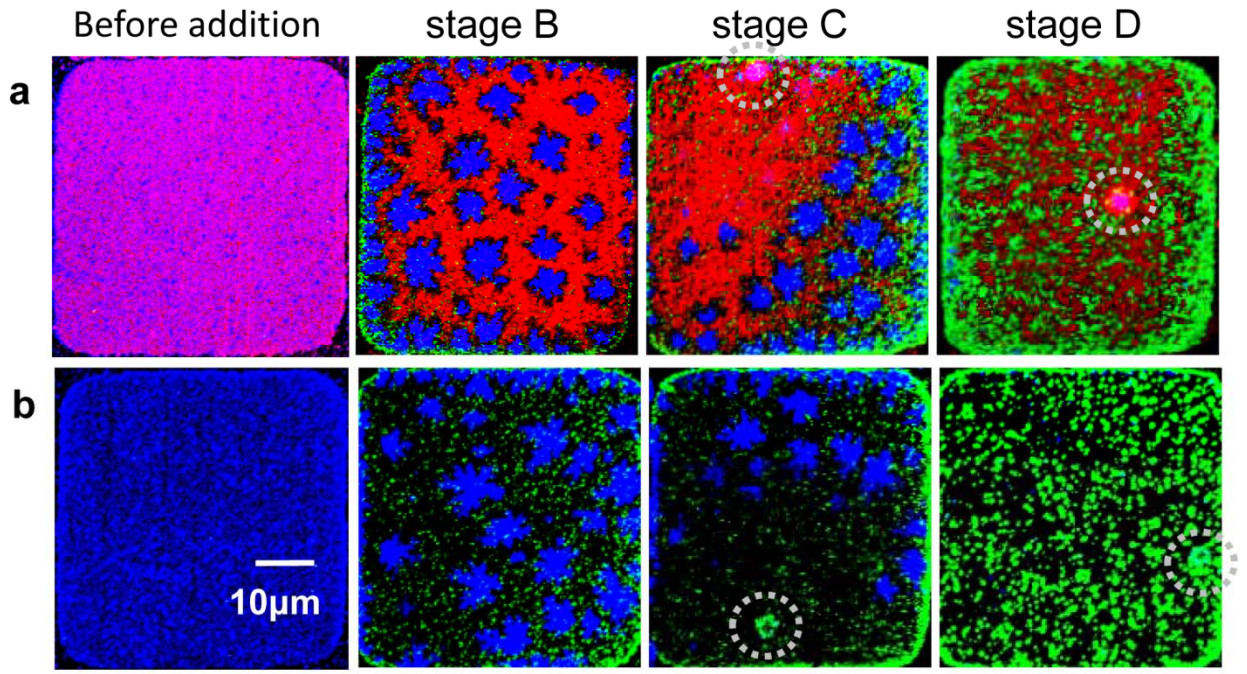

Figure 3-6. Fluorescence from antibodies shows the location of ceramide and sphingomyelin. The reaction by 0.005 unit/ml SMase in the 40/40/20 DOPC/BSM/Chol membranes was quenched at stages B, C, and D, and the membranes were treated with Alexa Fluor® 488-labeled anti-ceramide and Alexa Fluor® 647-labeled lysenin. The red color is from Texas-Red® DHPE, the green color indicates where ceramide locates, and the blue color indicates where sphingomyelin locates. The open gray circles indicate those bright features which initiate the reorganization of domains. (a) The membrane is stained by 0.5 mol% of Texas-Red DHPE. Purple indicates where it is stained by both red and blue markers. The images from each color channel before being superimposed are in Figure 3-7. (b) The membrane is not stained by Texas-Red DHPE. The non-superimposed images are in Figure 3-8. Gray circles indicate where the bright features locate.

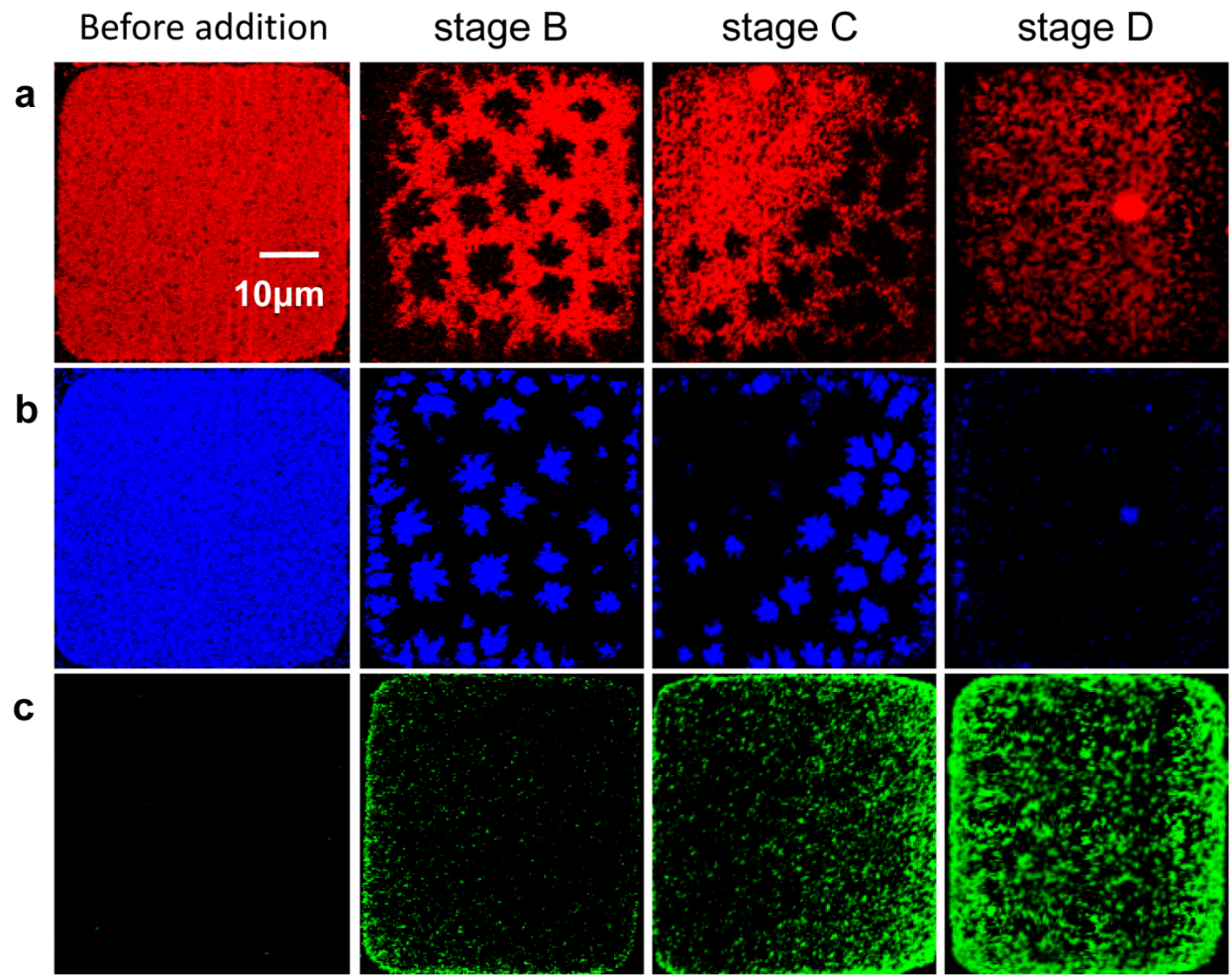

Figure 3-7. The images of Figure 3-6(a) before superimposition: (a) illuminated by Texas Red® DHPE; (b) illuminated by Alexa Fluor® 647-labeled lysenin; and (c) illuminated by Alexa Fluor® 488-labeled anti-ceramide.

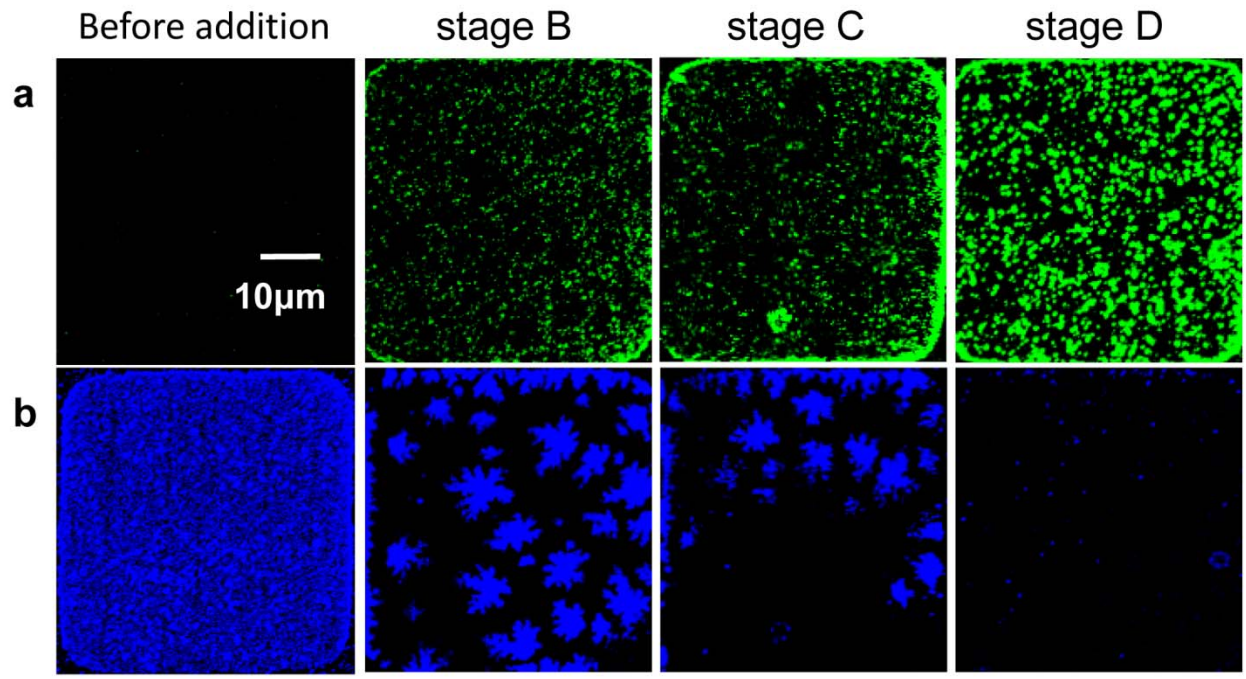

Figure 3-8. The images of Figure 3-6(b) before superimposition: (a) illuminated by Alexa Fluor® 488 labeled anti-ceramide; and (b) illuminated by Alexa Fluor® 647 labeled lysenin.

3.3.2.3. Single-labeling of either SM or Cer in the absence of lipid probes

To eliminate the possibility of any cross-reactivity between the two sets of antibody complexes, we also conducted single labeling of either anti-ceramide or lysenin (Figure 3-9). The similar results from the single labeling and each channel in the double labeling show that no significant cross-reactivity is occurring between the two sets of antibody complexes.

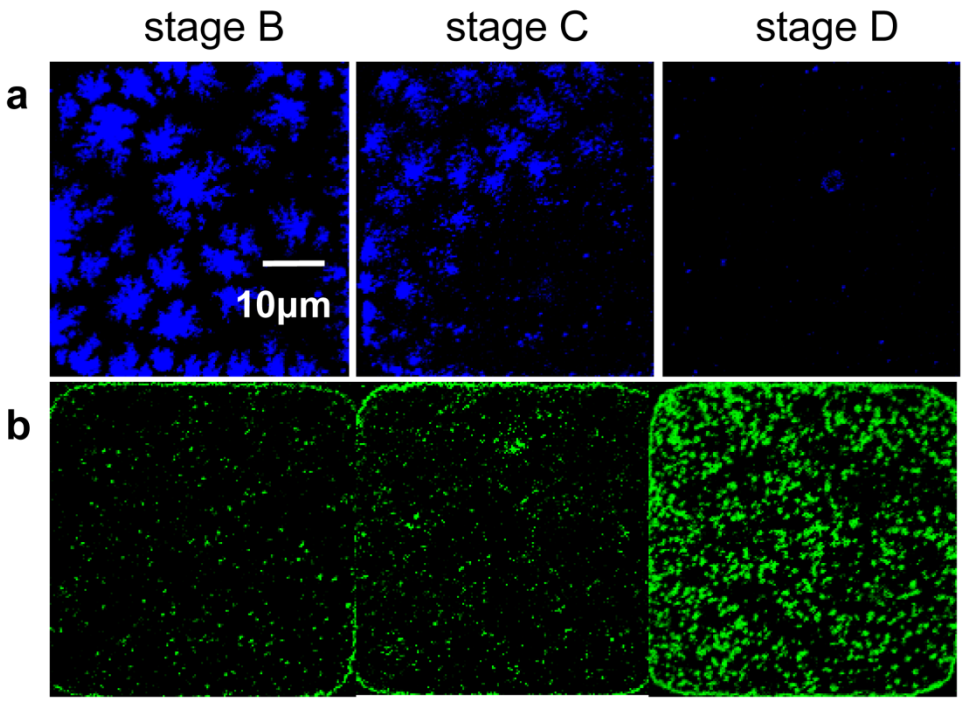

Figure 3-9. Single labeling of either SM or Cer. (a)The membrane is labeled with Alexa Fluor® 647 labeled lysenin. (b) The membrane is labeled with Alexa Fluor® 488 labeled anti-ceramide.

3.3.3. 3-D feature by fluorescence confocal imaging

3.3.3.1. Labeling of the bright feature in the absence of lipid probes

To further investigate the structure of the bright feature (defined in the Texas-Red® lipid probe images), we used confocal microscope to record the labeled-antibody image stack in the z direction perpendicular to the supported lipid bilayer plane. The membranes at stage D with single labeling in the absence of Texas-Red® lipid probes are used in order to reduce any cross reactivity between labeling molecules and to obtain clearer images. Figure 3-10(a) shows the image stacks obtained from the system labeled by Alexa Fluor® 488-labeled anti-ceramide antibody complexes and Figure 3-10(b) is from the system with Alexa Fluor® 647-labeled

lysenin antibody complexes. The number at the upper right corner of an image indicates the location of that image in the stack. "0" indicates the focal plane of the supported lipid bilayers, "-1" indicates the first plane below the lipid membrane plane (the glass support side), "1" indicate the first plane above the lipid membrane plane (the solution side), etc. The distance between two consecutive planes is 0.36 μm.

Figures 3-9(a) and (b) show that both anti-ceramide and lysenin bind to the bright features, suggesting that these features contain both ceramide and sphingomyelin. In both systems, hollow rings exist in the lipid membrane planes and these rings gradually shrink in the planes away from the lipid membranes. The antibodies were added after these features formed and would primarily stain their outer surface if no penetration occurred. We also imaged the planes below the lipid membrane plane. The signal in the "-1" plane is weaker than the signal in the planes above the lipid membrane and no signal can be observed in the planes further below the "-1" plane. Therefore, the shrinking hollow rings in the z stack images at and above the lipid membrane indicate that these features connect to the membrane and extrude out into the solution side.

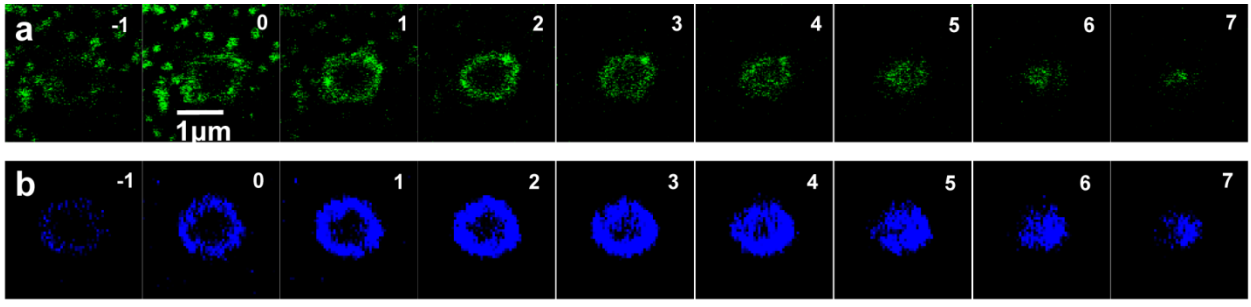

Figure 3-10. Fluorescence confocal imaging of the 3-D features in stage D. The features were stained either (a) by Alexa Fluor® 488-labeled anti-ceramide or (b) by Alexa Fluor® 647-labeled lysenin. The number at the upper right corner of an image indicates the location of that

image in the stack. "0" indicates the focal plane of the supported lipid bilayers, "-1" indicates the first plane below the lipid membrane plane (the glass support side), "1" indicates the first plane above the lipid membrane plane (the solution side), etc. The distance between two consecutive planes is 0.36 μm.

3.3.3.2. Consistent appearances of the bright features among corralled membrane systems

We observed consistent appearance of the bright features in all of the corralled membranes. The consistent appearance was already roughly observed in the Texas-Red® lipid probe images from a regular microscope (Figure 3-1(c)). Here, we further observed their consistent appearance clearly in confocal imaging of the labeled antibodies without any possible interference from the lipid probe (Figure 3-11). The confocal imaging allows us to observe the size and shape of these 3-D features out of the lipid membrane plane. Four corrals cropped from a corralled membrane system are used to demonstrate the consistency of these features in different corrals. The planes are labeled in the same way as described in the last section. The consistency of the appearance in each image from different focal planes shows that these 3-D features have a consistent size and shape. The consistent appearances of these features in membranes with a confined size suggest that these features could be another phase in addition to SM-enriched and Cer-enriched domains in the SMase-lipid membrane system. Sometimes multiple 3-D features are formed in a corral. For example, the upper right corral in Figure 3-11(b) has two features. Both 3-D features can be observed clearly from the "1" plane to "3" plane and have smaller laterally projected diameter. The overall extent of these two features seems to be similar to the extent of the feature in a one-feature corral. The consistent extent is reasonable since each corralled membrane contains the

same amount of reactants and SMase, which should result in the same phase extent. The different number of the features in corrals confined to the same size is due to the kinetics of the nucleation of the features, which will be further discussed in chapter 5.

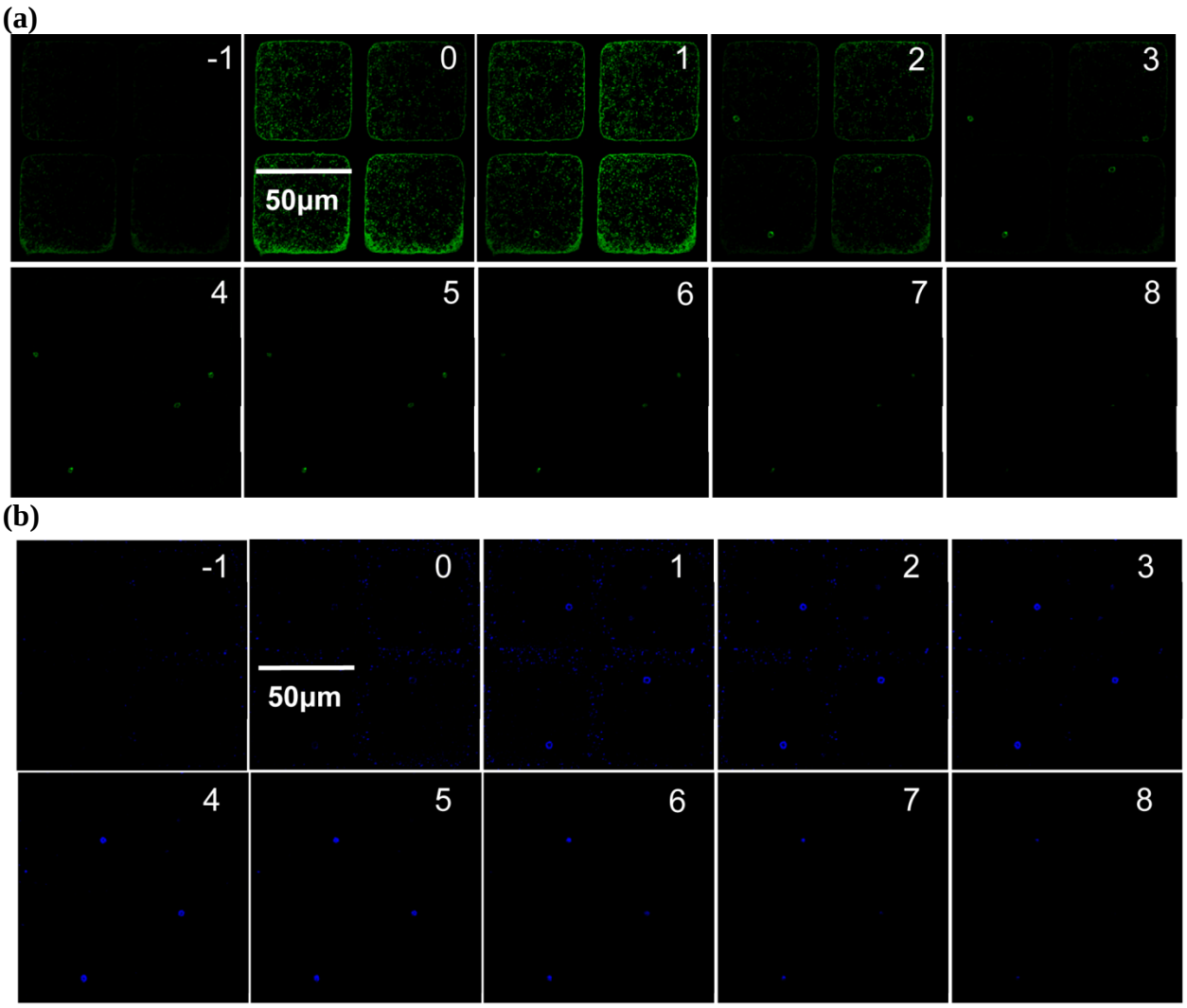

Figure 3-11. Consistent appearance of the features among the membranes confined to the same size. (a) The membrane systems were stained by Alexa Fluor® 488-labeled anti-ceramide. (b) The membrane systems were stained by Alexa Fluor® 647-labeled lysenin. Both sets of images were obtained in the stage D of the morphology evolution induced by 0.005 unit/ml SMase. The images from different focal planes are numbered in the same way as described in Figure 3-10.

The background signal with the corral shape in (b) was from the weak non-specific binding of lysenin antibody complexes to the BSA used to print the corral.

3.3.4. Where does the SMase bind?

The selective binding of SMase or its spatial distribution over the lipid membrane was investigated using Alexa Fluor®-488 labeled SMases. Figure 3-12 shows that morphology evolution induced by the labeled SMase in a Texas-Red® DHPE-stained membrane (images before being superimposed are in Figure 3-13). The images from Texas-Red® DHPE show that the labeled SMase also induces the stages with corresponding dark domains and bright features (defined in Texas-Red® images), although the size, shape and distribution of the dark domains are not completely the same as those in a regular SMase system. The quick growth of dark domains in minutes, a pause morphology, the formation of bright features followed by dissolution of one type of domain and growth of the other, and a final stationary morphology can be clearly observed (Figure 3-12). According to the consistent morphology they produce, we suggest that the behavior of the labeled SMase is similar to the one of the regular SMase.

As shown in Figure 3-12, the yellow color saturated with both red and green colors at the bright features (indicated by dashed circle) indicates that the bright feature is rich in not only Texas-Red® DHPE but also a large amount of the labeled SMase. Another important thing to notice is that the labeled SMase binds significantly to the growing-type dark domains but not to any of the dissolving-type dark domains. The antibody characterization results in the previous paragraphs have shown that the growing-type dark domains are Cer-enriched domains and the dissolving-

type dark domains are SM-enriched domains. The lesser binding extent of the labeled SMase to the SM-enriched domains suggests that SMase cannot easily access the sphingomyelin stored in SM-enriched domains.

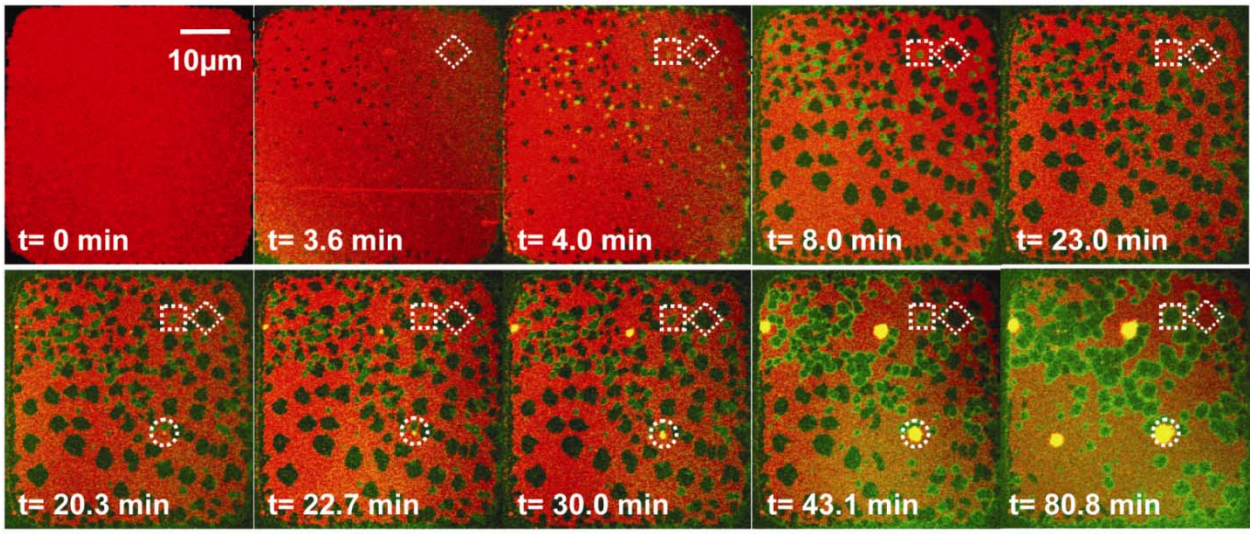

Figure 3-12. Morphology evolution of the 40/40/20 DOPC/BSM/Chol Texas-Red® DHPE-stained membrane treated with 0.005 unit/ml Alexa Fluor®-488 labeled SMase. Red color is from Texas-Red® DHPE and green color is from Alexa Fluor®-488 labeled SMase. The yellow color indicates the superimposition of both red and green markers. The non-superimposed images are in Figure 3-13. Dashed box indicates the growing-type dark domains; dashed diamond indicates the dissolving-type dark domains; dashed circle indicates the bright feature, as defined in Texas-Red® DHPE images.

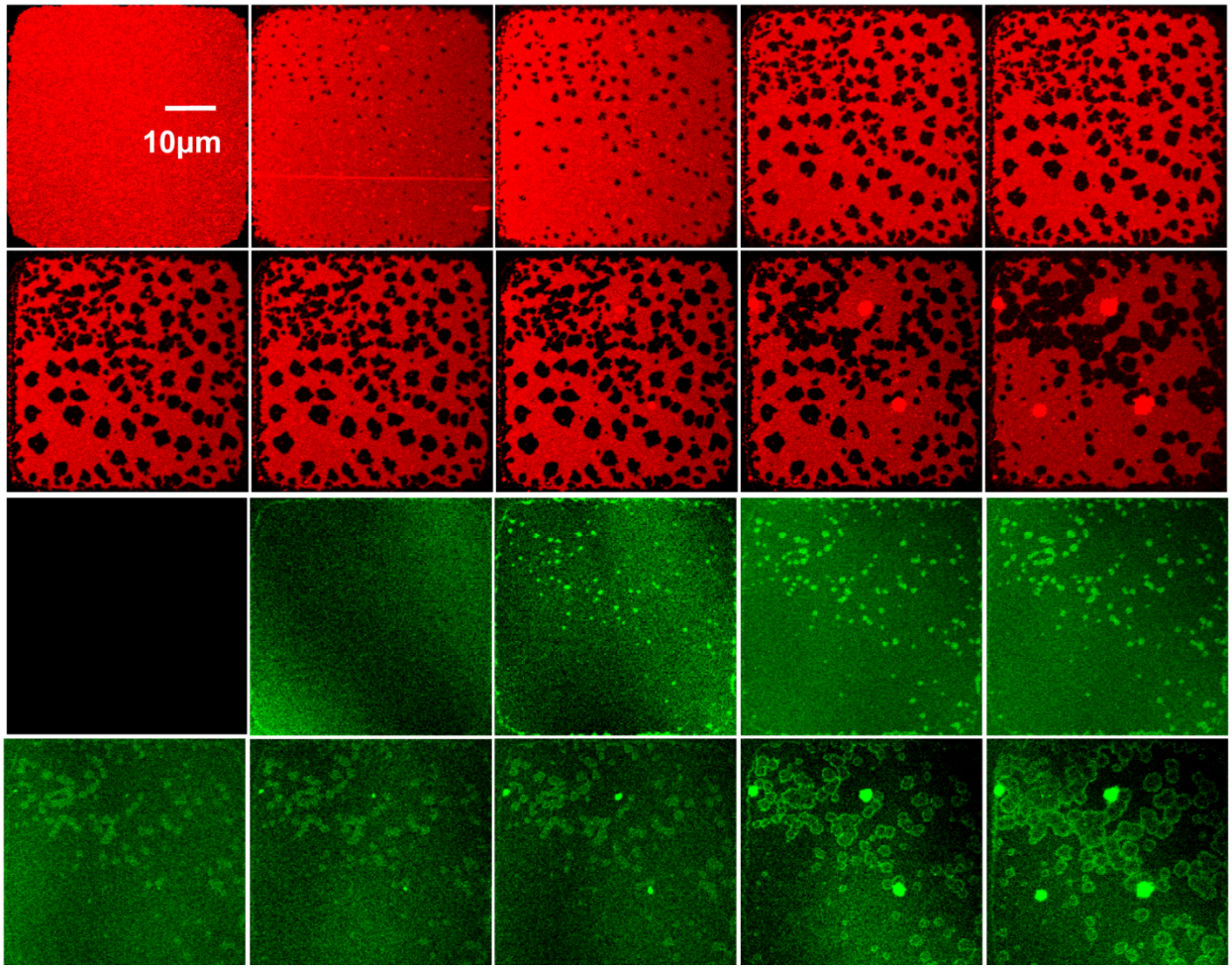

Figure 3-13. The images of Figure 3-12 before superimposition. The upper row shows the images under the illumination of Texas Red® DHPE. The lower row shows the images under the illumination of Alexa Fluor® 488-labeled SMase.

3.3.5. Identification of the solvent-mediated phase transformation process at stage C by spatial sphingomyelin concentration profile

The domain reorganization at stage C occurs when the bright feature defined in Texas-Red® DHPE images forms and causes SM-enriched domains to dissolve. To investigate what causes

this domain reorganization, we carefully examined the spatial fluorescence intensity profile of the labeled-lysenin complex images. Although the exact correlation between the fluorescence intensity from the labeled-lysenin complex and the amount of sphingomyelin is not clear, the stronger the intensity, the more sphingomyelin should be there. This positive correlation was used to infer the spatial distribution of sphingomyelin. The typical fluorescence images of the lysenin-labeled complex at stage B, C, and D in the SLB treated with 0.005 unit/ml SMase are shown in Figure 3-14(a, b, c). To further demonstrate how the intensity varies spatially, the surface plots of the fluorescence intensity from Figure 3-14(a, b, c) are shown in Figure 3-14(d, e, f) respectively. The intensity of the SM-enriched domains was high and saturated the pixels. In addition, the medium fluorescence intensity from the bright feature which causes the dissolution of SM-enriched domains suggests that it also contains significant amount of sphingomyelin, consistent with those results obtained by the confocal microscopy. Furthermore, there was also significant fluorescence intensity from the background phase and it decreased towards the bright feature which can be observed in Figure 3-14(b) or (e).

In order to obtain a clearer view of the sphingomyelin concentration variation along the radial direction away from the bright feature, we plot the intensity profiles along the dashed lines in Figure 3-14(a, b, c) in Figure 3-14(g). The concentration of SM in the background phase where SM-enriched domains had not dissolved was significantly higher than the concentration where they had already dissolved. Therefore, the decrease of the concentration of sphingomyelin in the background phase, named as [SM], surrounding the SM-enriched domains is suggested to drive the dissolution of these domains. The decrease of the [SM] along the radial direction towards the

bright feature suggests that the bright feature consumes sphingomyelin and acts as a sink of sphingomyelin molecules.

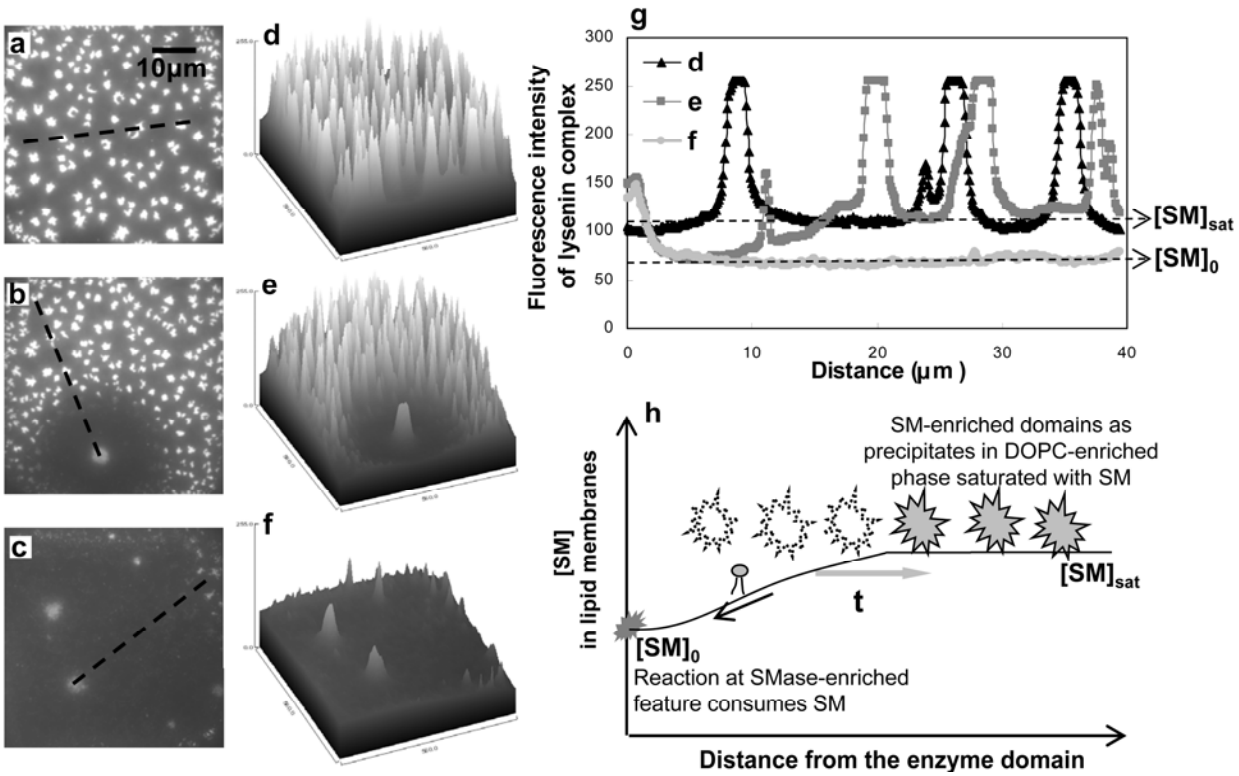

Figure 3-14. Spatial sphingomyelin concentration profile indicated by fluorescence intensity of the labeled-lysenin complex. (a, b, c) The typical fluorescence images of the labeled-lysenin complex in the 40/40/20 DOPC/BSM/Chol membrane after the reaction induced by 0.005unit/ml SMase is quenched at stage B, C, and D, respectively. (d, e, f) Surface plots of the fluorescence intensity from d, e, f, respectively. (g) Intensity profiles of labeled lysenin along the dashed lines in a, b, c. (h) Schematic representation of the concentration profile of SM in the radial direction from the bright feature and how the consumption of SM can cause the dissolution of SM-enriched domains.

3.4. Discussion

3.4.1. The interpretation of the overall behavior

The interpretation of the phenomena induced by SMase reaction is illustrated in Figure 3-15, combining the morphology evolution with the identification of the domains in each stage. Before the addition of SMase, we observe pre-existing sub-micron-sized domains. These gray domains are probably the conventional rafts rich in sphingomyelin and cholesterol, and the light background region is a liquid-disordered DOPC-enriched phase. After the addition of SMase, some dark domains grow (stage A) and a pause morphology is reached (stage B) in the Texas-Red® DHPE-revealed morphology evolution. The antibody characterization suggests that these dark domains are SM-enriched and Cer-enriched domains. The stable pause morphology can be explained by our labeled SMase results showing that SMase cannot easily get access to SM-enriched domains (Figure 3-12). The irregular shape of the SM-enriched domains indicates their gel properties with which boundaries cannot relax to reduce the line tension with the surrounding fluid phase. Once most of the SM is stored or aggregated in SM-enriched gel domains, the overall reaction may become very slow, resulting in a period of stasis.

The pause ends after the bright features (defined in the Texas-Red® DHPE-revealed morphology evolution) form. The results from labeled SMase and antibody characterization suggest that these bright features are rich in SMase, and contain sphingomyelin and ceramide. Only after these features rich in SMase form in the systems, the dissolution of SM-enriched domains and the further growth of Cer-enriched domains can be observed (stage C). The mechanism of the SM-enriched domain dissolution and conversion into Cer-enriched domains will be discussed later.

The final stationary morphology is reached after all of the SM-enriched domains dissolve, and the Cer-enriched domains fully grow (stage D).

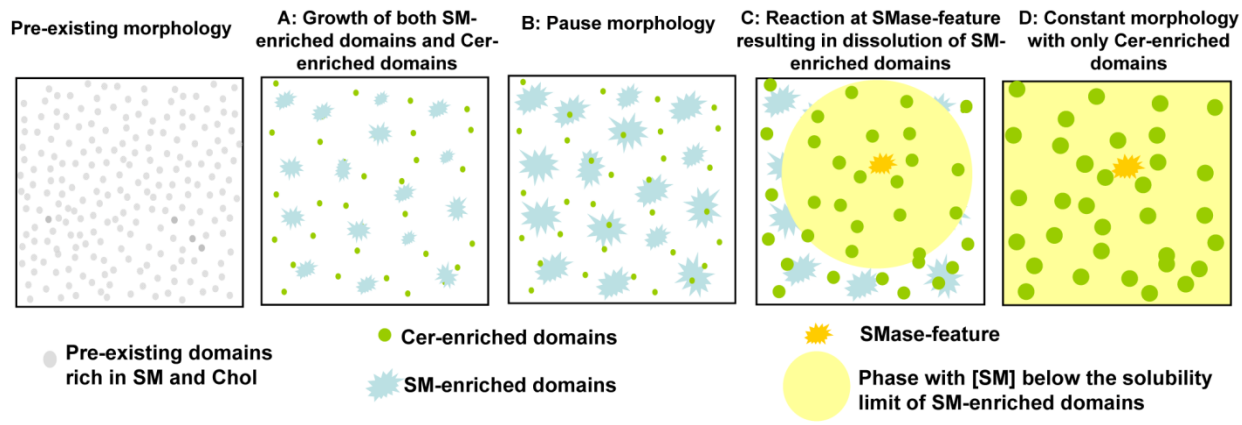

Figure 3-15. Schematic illustration of the spatial morphology change induced by SMase. The evolution is composed of three constant morphology stages (pre-existing, B, D) switched by two transformation stages (A, C).

Our anti-ceramide antibody characterization results (Figure 3-6) show that the mode of ceramide generation also changes with these stages. Figure 3-15 shows a schematic illustration of how the ceramide and sphingomyelin contents in a membrane system may change with the stages. Before the addition of SMase, no labeled anti-ceramide antibody can be observed. After the addition of SMase, only a small amount of labeled anti-ceramide is observed in stage B and no significant difference can be observed over the whole stage B. After the transformation stage C, a significant increase of the labeled anti-ceramide amount can be observed in the final stage D. The anti-ceramide antibody characterization is shown to be consistent with the lysenin antibody characterization indicating the sphingomyelin amount change with the stages (Figures 3-5 and 3-

13). The membrane before addition of SMase is rich in sphingomyelin. In stage B, the un-reacted sphingomyelin is stored in gel-like SM-enriched domains. In stage C, the SM released from the SM-enriched domains is probably primarily converted to Cer at the SMase-feature (section 3.3.5). The significant growth of the Cer-enriched domains is followed after the ceramide generated at the SMase-features diffuses back to the whole membrane. These consistent characterization results following the reaction stoichiometry show how the ceramide generation can change with the stages caused by the SMase-induced complex phase behavior, as illustrated in Figure 3-16.

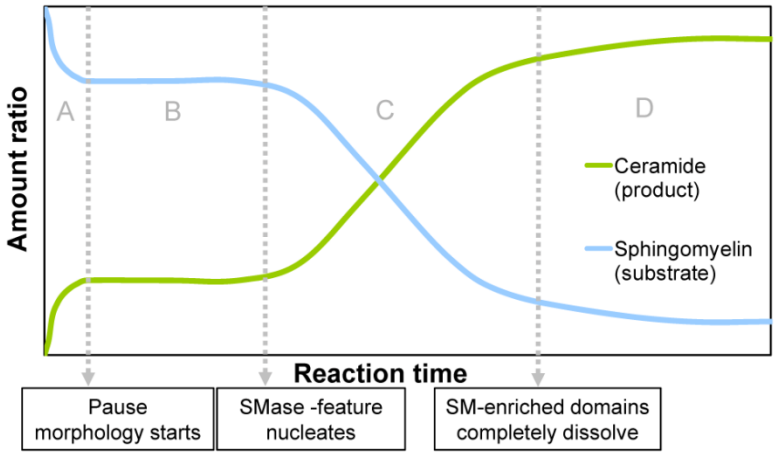

Figure 3-16. Schematic illustration of the multiple-time-domain ceramide generation due to the phase changes induced by SMase.

3.4.2. The formation of SMase-feature

We hypothesize that the bright feature rich in SMase is another phase in addition to SM-enriched domains, Cer-enriched domains and the DOPC-enriched phase in SMase-model raft membrane systems. The feature is always found to nucleate in the fluid DOPC-enriched phase, and contains not only SMase but also SM and Cer, as shown from our antibody characterization and labeled

SMase experiments (Figures 3-9). The confocal imaging of antibody characterization further shows that these features have consistent 3-D appearances and fluorescence intensity from either anti-ceramide or lysenin antibody complexes in the membrane systems confined to the same size (Figure 3-11).

In our experiments, we remove SMase from the bulk solution after the membrane is exposed to the SMase solution for two minutes; therefore, the supply of SMase to form the SMase-features can only be from the SMase binding to the membrane during this period and remaining after the washing step. The high binding rate and slow dissociation rate of SMase [126,127] allow a significant amount of SMase still binding to the membrane after the washing step. This experimental procedure excludes the possibility that the bright feature rich in SMase is formed from precipitation from an excess of SMase in the bulk solution. In addition, under this experiment condition, we can also ensure that the amount of SMase in the membrane systems in the later stage C cannot be more than the amount in the earlier stage B. Therefore, the further significant ceramide generation in stage C after a period of stasis (stage B) is not due to the increased amount of SMase but probably due to the SMase's property change after the SMase is concentrated to the SMase-features.

We speculate that the SMase in the SMase-feature can process SM at low SM concentration more efficiently. Labeled SMase experiments suggest that the pause morphology in stage B can be explained by the formation of SM-enriched domains leaving the DOPC-enriched phase with a low concentration of SM, and the inaccessibility of SMase to the SM-enriched gel domains. The labeled lysenin intensity profile experiments show that the SM concentration level in the DOPC-

enriched phase did not change in stage B; however, once an SMase-feature nucleated in the DOPC-enriched phase, the SM concentration in the DOPC-enriched phase started to reduce significantly (Figure 3-14). Since the overall SMase amount in stage C is similar to or less than the amount in stage B, we reason that the concentrated SMase with its substrate and product (SM and Cer) at the SMase-features can process its substrate at low concentrations more efficiently than can the distributed SMase on the DOPC-enriched phase. Further investigations on the structure and composition of the SMase-features could further clarify the reasons for this behavior.

We observed that the formation of SMase-features at about half an hour after the addition of SMase, which allows the development of the stage B in the morphology evolution. The appearance of the SMase-features after a period of stasis can be explained by their long induction time. Nucleation of a new phase is known to be a kinetic process, influenced by the organization of the new formed phase. Usually, the slower the nucleation rate, the longer the induction time [142]. We observed very few numbers of these features forming in a corralled membrane compared with other kinds of domains, indicating their slow nucleation rates, which is consistent with the observed long induction time. In this study, we qualitatively demonstrate the appearance of these features and further statistical studies about the nucleation time of these features will be shown in chapter 5.

The observation of an enzyme-enriched phase was also reported in a lipid monolayer system with another kind of interfacial lipase, phospholipase A.[143] Although the function of the

phospholipase A-enriched domain was not addressed, this enzyme domain was also shown to occur in the middle of the reaction and to cause the dissolution of its substrate domains.

3.4.3. Reaction-induced phase transformation by SMase

We directly visualize a kinetic process of the growth of domains which are characterized as SM-enriched and Cer-enriched domains induced by SMase in a model raft membrane. Recently, Castro et al. have used the fluorescence multiprobe and multiparameter approach to show that one ceramide molecule could recruit up to three sphingomyelin molecules to form gel domains in model raft membranes.[134] In the absence of SMase, their study suggests that it is thermodynamically favorable for ceramide to cause the formation of not only Cer-enriched domains but also SM-enriched domains. That is, a three-phase regime, consisting of a liquid-disordered, SM-enriched, and Cer-enriched phases, exists in a certain model raft composition range in lipid membranes, as shown in Figure 3-17. In the presence of SMase, our study shows one kinetic process by which this phase change occurs, driven by the compositional changes or the generation of ceramide by SMase (shown by the purple line in Figure 3-17). The compositional change drives the system to cross a phase boundary and to enter into a three-phase coexistence regime, and thus the original phases in the system can be transformed to the three phases mentioned above. As temperature and pressure are kept constant under most biological conditions in nature, the compositional change induced by an enzymatic reaction could be a way to transform one phase to another and to switch the spatial pattern.

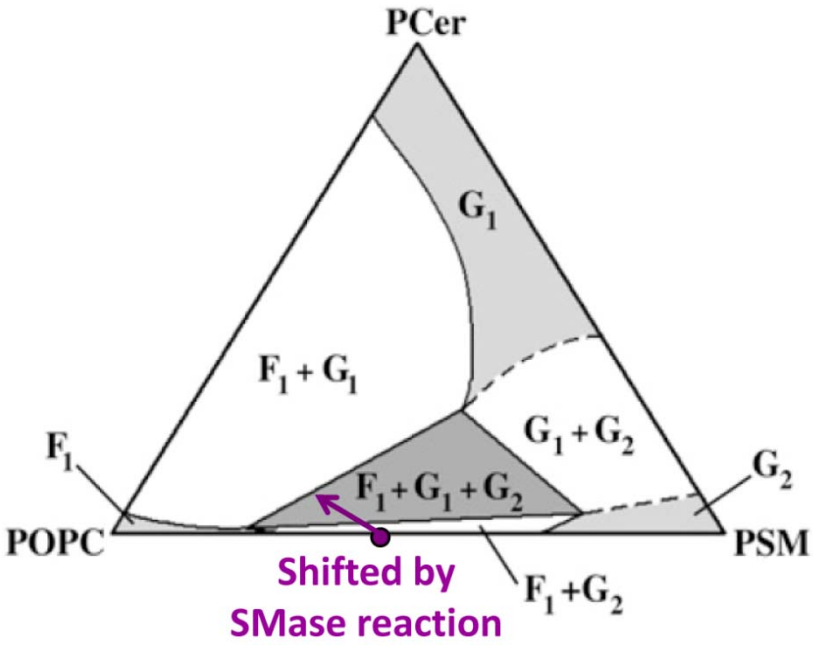

Figure 3-17. SMase enzymatic reaction causes the membrane system entering into a three phase coexistent region in a PC-SM-Cer ternary mixture phase diagram. The phase diagram is adapted from Castrol et al [134]: G1 represents the Cer-enriched phase, G2 represents SM-enriched phase an F1 represents a PC-enriched phase. The purple dot indicates the initial location of a membrane system before addition of SMase (in the absence of Cer). After the addition of SMase, the location of the membrane system in the phase diagram is shifted due to the composition change caused by SMase enzymatic reaction. The purple line indicates the shifted direction determined by the reaction stoichiometry (one SM to one Cer).

3.4.4. Solvent-mediated phase transformation

The domain reorganization in stage C starts once an SMase-feature nucleates. The relatively fast morphological change and the antibody characterization indicate that the membrane composition starts to change significantly. Several evidences suggest that the reaction primarily occur at the

SMase-feature in this stage C although slow reaction may still occur in the fluid DOPC-enriched phase or even at the SM-enriched and Cer-enriched domains. First, the SM concentration decreasing towards the SMase domain shown in Figure 3-14(g) indicates that the SMase-feature serves as a sink for SM. In addition, all of the features in stage C except the SMase-feature also appear in stage B but no obvious morphology change can be observed. Furthermore, from our antibody characterization results, the ceramide amount starts to increase significantly only after the SMase-features form.

This phenomenon is analogous to a solvent-mediated phase transformation, in which a substance undergoes solid-to-solid phase changes via a solution phase in a three-dimensional system. A schematic illustration of this phenomenon is given in Figure 3-14(h). The SM-enriched domain is analogous to a precipitate in the fluid DOPC-enriched phase saturated with SM ($[SM]_{sat}$) in stage B. Once an SMase-feature nucleates, which is another form of precipitate, it starts to consume SM and decrease the SM concentration in the fluid DOPC-enriched phase. The SM-enriched domains begin to dissolve once their surrounding SM concentration in the DOPC-enriched phase drops below its solubility limit. With time, more and more SM is consumed at the SMase-feature and thus the $[SM]_{sat}$ front moves away from the SMase domain and more SM-enriched domains dissolve. After SM is converted to Cer at the SMase-feature, the Cer diffuses back to grow Cer-enriched domains. A regular solvent-mediated phase transformation is composed of only the dissolution of a less stable form of precipitate and the growth of a more stable form. The behavior we observed here is further mediated by a chemical reaction.

3.4.5. Potential biological implications of the morphology switches and multiple-time-domain ceramide generation

In the overall process induced by a single addition of SMase, we report that SMase can be actively involved in the membrane phase behavior and induce two phase transformations with disparate time scales to switch a pre-existing raft morphology to a pause morphology with both SM-enriched and Cer-enriched domains, and switch the pause morphology to a post-reaction morphology with only Cer-enriched domains.

The existence of the switches between lipid membrane morphologies could be important since different domain morphologies may assume different functional states. In fact, the different cell membrane morphologies occurring at different time scales have been reported during apoptosis in physiological studies when SMase is activated. In early stage of apoptosis, large micron-sized platforms for protein clustering are observed in cells of diverse origins [35,144-148]. No significant cell membrane morphological response was reported after the large signaling platforms form. In the late stage of apoptosis, some physiological studies report the appearance of membrane bulges whose formation could be facilitated by the existence of Cer-enriched domains.[58,59,149] The similar timing and sequence of these different cell membrane morphologies to the morphology change induced by the SMase in model raft membranes may suggest that the two SMase-induced phase transformations may contribute to cell membrane heterogeneity in apoptosis.

The kinetics of ceramide accumulation in cells undergoing apoptosis have been reported to have multiple time domains [17]. A modest accumulation of ceramide in minutes corresponding to the early stage of apoptosis is observed in some cell systems [28,146,147,150,151], whereas a much more

significant accumulation of ceramide is observed on the hour time scale corresponding to the late stage of apoptosis [58,149,152]. The very different responses, ranging from minutes to hours, have become a major source of confusion [17,153]. In our studies, we observed that only a small amount of SM is converted to Cer in stage A, since SMase cannot easily access the SM once it is trapped in SM-enriched domains. Most of the SM is converted to Cer after the formation of the slowly-nucleating SMase-feature, where SMase appears to process the low SM concentration left in the solvent phase (the DOPC-enriched phase) more efficiently. Questions still remain about the origin of the ceramide accumulation in cells undergoing apoptosis. The multiple-time-domain ceramide generation due the complex phase behavior induced by SMase suggests an alternative possibility that could contribute to the multiple-time-domain ceramide accumulation in cells.

3.5. Conclusion

Here we report that SMase can induce a reaction-induced and a solvent-mediated phase transformation in model raft membranes. SMase can be actively involved in the lipid membrane phase changes and the overall morphology change is caused not only by phase change due to compositional changes by SMase, but also by the selective binding of the SMase and SMase's special phase behavior during the solvent-mediated phase transfromation. The reaction-induced phase transformation, triggered by the addition of SMase, transforms a pre-existing morphology to a pause morphology with coexisting ceramide-enriched (Cer-enriched) and sphingomyelin-enriched (SM-enriched) domains. Later, the solvent-mediated phase transformation, triggered by the formation of a 3-D SMase-feature, occurs to further transform all of the SM-enriched domains into Cer-enriched domains. The results from antibody characterization and confocal

imaging suggest that the 3-D feature is rich in SMase, sphingomyelin (the substrate of the enzyme) and ceramide (the product of the enzyme). The distribution of sphingomyelin in the lipid membrane obtained by the fluorescence intensity profile of lysenin suggests that the SMase at this special feature processes sphingomyelin more efficiently. The existence of the stable pause morphology between the two transformations can be explained by the physical trapping of SM in SM-enriched domains, which SMase cannot easily access. The disparate time-scale of the formation of the SMase-features and the SM-enriched domains allows for developing a significant duration of the middle pause morphology. The occurrence of these two transformations causes switches of three stationary membrane morphologies and the ceramide generation by SMase can be also divided into multiple-time-domains in model raft membranes.

Chapter 4. Domain Dynamics during Reaction-induced Phase Transformation

4.1. Introduction

Physiological studies have reported that large platforms containing ceramide form in a few minutes after sphingomyelinase (SMase) translocates to the cell membrane at the early stage (or induction phase) of apoptosis.[28,35,38,57] These large platforms facilitate the clustering of death receptors for triggering their subsequent cellular pathways. Questions remain about the mechanism underlying the spatial pattern rearrangement between the pre-existing rafts and the later large platform. Although literature has proposed that ceramide generated by SMase drives the pre-existing rafts to coalesce to form the large platform[154], the fact that some membrane proteins found in the conventional rafts are absent in the later ceramide-containing large platforms is inconsistent with the coalescence conjecture.[155]

It has been reported that ceramide can replace cholesterol in the conventional rafts which are rich in sphingomyelin and cholesterol.[156] Some other studies have reported that ceramide can recruit sphingomyelin to form membrane domains rich in sphingomyelin and ceramide in environments with or without cholesterol.[134,155] However, most of the studies have been done in the absence of SMase and have not shown how the domain dynamics proceeds under the competition between ceramide and cholesterol for sphingomyelin after ceramide is generated by SMase *in situ*.

In chapter 3, we have shown that SMase induces a reaction-induced phase transformation to transform a pre-existing raft morphology to a stationary morphology containing micron-sized SM-enriched domains. The SM-enriched domains are suggested to form due to the recruitment of SM by the generated Cer.[157] However, in chapter 3, the pre-existing rafts in the prepared supported lipid bilayers (SLBs) were sub-micron-sized and the detailed morphology evolution during the transformation has not been clearly visualized by fluorescence microscopy.

In this chapter, we prepare both a GUV system and an SLB system with micron-sized pre-existing domains to visualize the domain dynamics during the reaction-induced phase transformation. Giant unilamellar vesicles (GUVs) have been shown to have consistently micron-sized pre-existing rafts.[5,158] The appearance of the pre-existing domains in supported lipid bilayers (SLBs) has been shown to be more complicated and to vary with the thermal history of the preparation.[108-110] We are able to prepare the micron-sized pre-existing domains by adjusting the thermal history during the supported lipid bilayer formation. The overall SMase-induced phase behavior is comparable in both the GUV system and the SLB system in spite of the different mobility of domains. The results show the dynamics of the transformation from pre-existing rafts to SM-enriched domains under the competition between ceramide and cholesterol.

4.2. Methods

4.2.1. Materials

1,2-Dioleoyl-sn-glycero-3-phosphocholine (DOPC), cholesterol (Chol), and brain sphingomyelin (BSM) were purchased from Avanti Polar Lipids (Alabaster, AL). Texas-Red®1,2-dihexadecanoyl-*sn*-glycero-3 phosphoethanolamine triethylammonium salt (Texas Red® DHPE) and Alexa Fluor® 488 goat anti-rabbit IgG were purchased from Invitrogen (Eugene, OR). Lysenin antiserum was purchased from Peptides International, Inc. (Louisville, KY). Sphingomyelinase from *Bacillus cereus* and all other reagents, unless otherwise specified, were purchased from Sigma (St. Louis, MO). The PBS buffer in this paper is 0.01 M phosphate buffered saline (138 mM NaCl/ 27 mM KCl, pH 7.4).

4.2.2. Preparation of giant unilamellar vesicles by electroformation

We prepared giant unilamellar vesicles (GUVs) using the electroformation technique of Angelova and Dimitrov [105] in a temperature-controlled chamber. Approximately 20 μL of lipids dissolved in chloroform at a concentration of 5 mg/mL were spread onto each of two 5cm x 5cm conductive indium tin oxide plates and dried under vacuum. 0.5 mol% Texas-Red® DHPE was incorporated into the lipid mixture (unless otherwise specified). The GUVs were grown in a 270 mM sucrose solution for 1.5 hr at a temperature above the lipid miscibility transition temperature. The buffer with an osmolarity of 270mM (2.5mM $MgCl_2$/125mM NaCl/12.5mM HEPES, PH=7.4) was used to dilute our GUV stock solution in a 4:1 volume ratio in order to make the GUVs' buffer (2mM $MgCl_2$/100mM NaCl/10mM HEPES/54mM sucrose) similar to that used in the SLB system.

4.2.3. Preparation of small unilamellar vesicles (SUVs)

Small unilamellar vesicles (SUVs) were prepared for the vesicle deposition to form supported lipid bilayers (SLBs). SUVs were formed by using the extrusion technique where dried lipids are reconstituted in the buffer (10 mM HEPES, 2 mM $CaCl_2$, and 100 mM NaCl, PH=7.4) at a concentration of 2 mg/mL and then passed 19 times through an 80-nm polycarbonate filter in an Avanti Mini-Extruder (Alabaster, AL). 0.5 mol% Texas-Red® DHPE was incorporated into the lipid mixture (unless otherwise specified). The stock SUV solutions were stored at 4˚C for up to one week before being used. The stock solutions were diluted to 0.2 mg/mL right before being used for the vesicle deposition.

4.2.4. Preparation of supported lipid bilayers

The prepared SUV solutions were flowed into a microchannel and deposited on the glass surfaces in the microchannel. More details can be found in our previous report.[157] Later, water was flowed into the channel to wash away the non-specifically bound vesicles. The deposition process was performed at a temperature above the miscibility transition temperature of the lipid mixture in a temperature-controlled water bath. The supported lipid membranes were stored in water at room temperature and used within two days of preparation. The membranes were heated to and kept at 37˚C for 20 minutes before use.

4.2.5. Characterization of the micron-sized pre-existing domains

To obtain 40/40/20 DOPC/BSM/Chol membranes with large pre-existing domains, water at room temperature instead of at 37˚C was used to wash away the excess vesicles, and the other steps were the same as those described in the last paragraph. We used lysenin to stain the sphingomyelin in lipid membrane systems. Ten μg/ml of lysenin, a sphingomyelin-specific binding protein, in the PBS buffer, was flowed into the channel and incubated with the lipid membrane for 20 min followed by a PBS buffer wash. After the wash, lysenin antiserum from rabbit (diluted 1/1000 with PBS), was flowed into the channel and incubated with the system for another 20 min, followed by another PBS buffer wash. The staining procedure was followed by using 20 μg/ml Alexa Fluor® 488 goat anti-rabbit IgG as labeled secondary antibodies.

4.2.6. Images by fluorescence microscopy

The morphology evolution images were observed using a Nikon TE2000-E inverted microscope with a Plan Neofluor 100X/1.30 oil immersion objective. The lysenin-characterization experiments and the morphology evolution of the SLB with micron-sized pre-existing domains were performed with a Zeiss laser scanning module (LSM) microscope with a Plan-Apochromat 63X/1.4 oil immersion objective. For a two-channel experiment, the excitation light from lasers at 488 and 543 nm was reflected by a dichroic mirror (HFT 488/543) and the emission was split by a second dichroic mirror (NFT 490) into two channels; light was passed through a 505–719 emission filter in the first channel and a 558–719 emission filter in the second channel to detect the Alexa Fluor® 488 and Texas-Red® DHPE, respectively.

4.3. Results

4.3.1. Multi-stage morphology evolution induced by SMase in giant unilamellar vesicles with freely mobile domains

The upper row in Figure 4-1 shows the domain morphology change of a GUV with 40/40/20 molar ratio of DOPC/SM/Chol induced by 0.005 unit/ml SMase at room temperature. Unlike SLBs fixed to solid supports, GUVs move around in solutions. In order to capture the domain dynamics of a GUV, we used a buffer with lighter density than the GUV stock solution to dilute the GUV solutions (while the osmolarity was kept the same). Since the GUV stock solution is a sucrose solution and GUV membrane has limited permeability to sucrose, the addition of lighter buffer (2.5mM $CaCl_2$/125mM NaCl/12.5mM HEPES) results in the density difference between the solutions inside and outside the GUVs. The higher density of the solution inside GUVs (than the density of the buffer outside) can drive the GUVs to settle down to the bottom of an observed well rather than easily move around in the solution.

After the addition of SMase, modulation of the boundaries of the micron-sized pre-existing domains occurred and some small dark domains became visible just beyond the previous boundaries (Figure 4-1(a)). The newly formed dark domains had dynamic movement, which usually lasted for about 10 min. During that period, the dark domains collided with each other, and then the morphology evolution paused after the network morphology formed (Figure 4-1(b)). The network morphology probably formed because these newly formed domains are in gel or solid phase and therefore could not fully coalesce to reduce their line tension when they collided with each other. That is, due to the slow diffusion of the lipid molecules in solid phase, the system was kinetically trapped in the network morphology with the relatively large interface.

The more detailed figures during this early stage are in Figure 4-2 and will be further discussed in the next paragraph. The pause morphology lasted for about 15-30 min, varying with different vesicle samples we observed. Later, as shown in Figure 4-1(c), a bright feature of large extent appeared and the dark domains became dynamic again. At this stage, the vesicle crumpled and completely collapsed after a few minutes. Figure 4-1(d) was taken of a vesicle deposited on a glass surface after its collapse.

In our previous study, we used antibodies and labeled-SMase to characterize the domain identity during the morphology evolution in SLBs and found that the morphology evolution can be divided into stages after the addition of SMase: (A) formation of both SM-enriched domains and Cer-enriched domains; (B) pause morphology; (C) nucleation of an SMase-feature followed by dissolution of the SM-enriched domains and further growth of the Cer-enriched domains; and (D) a stationary morphology with only the Cer-enriched domains present. The representative pictures of each of the stages are shown in the lower row of Figure 4-1. We have not been able to clearly characterize the domain identity in GUVs as we did in SLBs. Thorough washing to remove the background signal during the immunestaining is more difficult to achieve in GUV systems since the GUVs easily break or move around during the multiple washing steps.

However, if we compare the morphology evolution in GUVs (upper row in Figure 4-1) with the one observed in a corralled SLB membrane system (lower row in Figure 4-1), the two have comparable features occurring in the same order. The formation of new dark domains in GUVs can be compared to the stage A observed in SLBs (Figure 4-1(a) and (A)). The major difference is the dynamic movement of the dark domains in GUVs, which is probably due to the lack of

restriction from the solid support. The pause network morphology following the new dark domain formation stage can be compared to the stage B in SLBs (Figure 4-1(b) and (B)). No network morphology is observed in SLBs, probably because the solid support restricts the domains' mobility and thereby limits their chance to collide with each other. In GUVs, some bright features also appear after the pause morphology, which corresponds to the stage C (Figure 4-1(c) and (C)). After the GUVs become crumpled and are deposited on a glass surface, they have almost the same morphology as that observed in the stage D in SLBs (Figure 4-1(d) and (D)).

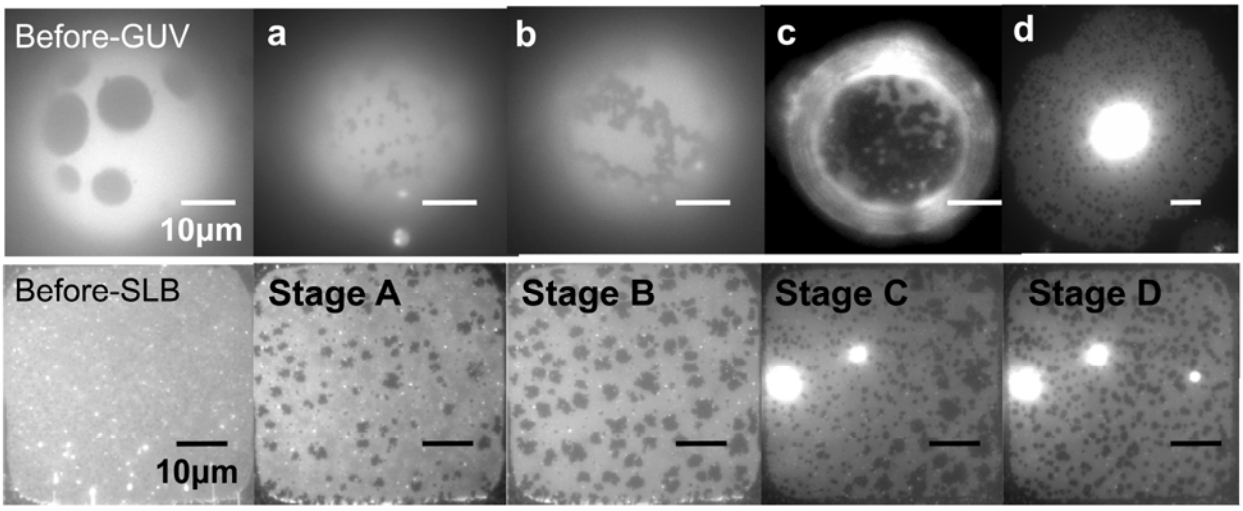

Figure 4-1. Comparable multi-stage morphology evolution induced by 0.005 unit/ml SMase in GUVs and SLBs. Both membrane systems contain a 40/40/20 molar ratio of DOPC/BSM/Chol with 0.5mol% Texas-Red® DHPE. The upper row is the images taken during the morphology evolution of GUVs: (a) is the image taken 4 min after the addition of SMase; (b) 10 min after the addition; (c) 30 min after the addition; (d) 50 min after the addition. The scale bar indicates the length of 10 μm. The scale bar is much shorter in (d) than in others, since the membrane has been deposited on the surface and thereby the lateral projection area became larger. The lower

row is the representative images in each stage of the morphology evolution of SLBs: (stage A) 2 min after the addition of SMase; (stage B) 17 min after the addition; (stage C) 45 min after the addition; (stage D) 80 min after the addition.

4.3.2. Detailed early-stage morphology evolution in a GUV

The domains in a GUV move around on the 3-D shell. Although the 3-D morphology image can be obtained by confocal microscopy, it takes a few minutes to scan a GUV's 3-D shell, which is not fast enough to capture the rapid dynamics of domains in the early stage. To observe how pre-existing rafts transformed to later new dark domains by using a regular microscope with a fixed focal plane, we chose a GUV with the pre-existing domain configuration in a way that we can clearly visualize and distinguish both a pre-existing raft and newly formed domains (Figure 4-2).

The pre-existing raft is the dark region enclosed by a white circle on the left of the vesicle. After the addition of SMase, we observe the modulation of the boundary of the pre-existing rafts. Some small dark domains (1-2 μm) separate out from the boundary of the pre-existing large raft. The separated-out domains move fast and are difficult to trace. Later, some domains start to stick to each other and form larger dendritic entities. These larger dendritic entities move more slowly than the smaller entities, and they also stick to each other if they collide. Finally, all of the domains are stuck to each other and the network morphology forms.

The small bright spots occurring in this early stage are thought of as small vesicles or lipid probe aggregates adsorbed on the GUV. They have been observed quite often in GUV systems even

before the addition of SMase. Unlike the extensive bright features that appeare after the pause morphology, these small bright spots do not significantly change their sizes and locations during the overall process. These small bright spots are thought not to be involved in the overall process and their relatively fixed position can also be used as a reference to see the relative motion of domains on a GUV surface.

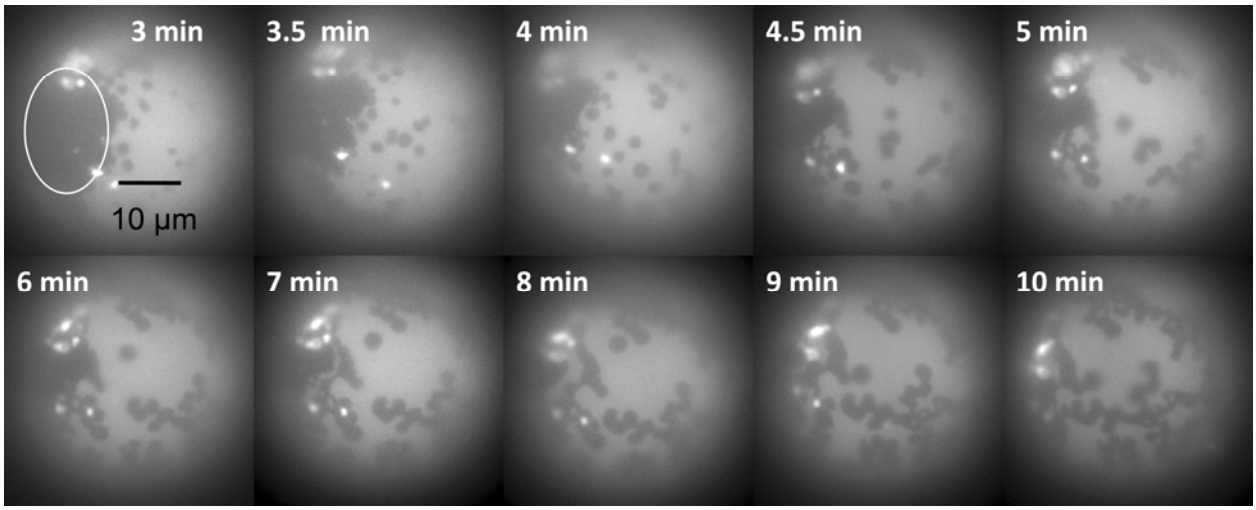

Figure 4-2. Early-stage SMase-induced morphology evolution in a GUV. The membrane system contains 40/40/20 DOPC/BSM/ Chol and was exposed to 0.005 unit/ml SMase.

4.3.3. Detailed early-stage morphology evolution in SLBs

The pre-existing domain morphology in SLBs is more complex and varies with the thermal history during the bilayer formation. Here, we prepared two SLB membrane systems: one with sub-micron-sized pre-existing domains and the other with micron-sized pre-existing domains, and observed their early-stage morphology evolution (stage A).

Figure 4-3(a) shows the early morphology evolution in an SLB membrane system with sub-micron-sized pre-existing domains. At t=0, the immobile sub-micron-sized dark domains are probably the rafts rich in SM and Ch according to the lipid probe's partition behavior.[5,159] The small bright dots are probably the adsorbed small vesicles which were found not to influence the overall morphology evolution. After the addition of SMase, the immobile sub-micron-sized dark domains became fuzzy (comparing the pictures at t=0, 0.5, and 1.5 min). At t=1.5 min, the boundary of the original sub-micron-sized domains could no longer be easily distinguished and what we observed was the gray fuzziness in the light background phase. The fuzziness in the light background phase indicates that the composition in that region is different from the composition of the light background phase or that there are very small domains which cannot be easily resolved by a microscope. At the same time, some new dark domains nucleated and grew with time (comparing the pictures at t=1.5, 2, 2.5, and 6 min). These new dark domains in this SLB system have been characterized in chapter 3 as micron-sized SM-enriched domains and sub-micron-sized Cer-enriched domains. The formation of these new dark domains seemed to consume the gray fuzziness since the region surrounding the domains in the background phase is lighter, and the gray fuzzy area in the background phase diminished with the growth of these domains. Eventually, all of the fuzziness was gone and the background phase looked uniform.

Figure 4-3(b) shows the early morphology evolution in an SLB membrane system with micron-sized pre-existing domains. The new dark domains were clearly shown to nucleate in a region other than where the pre-existing domains were located, and the pre-existing domains gradually dissolved. At an early time, the new dark domains primarily nucleated in most of the region in the DOPC-enriched phase but not in the region close to the pre-existing domains. While the pre-existing domains faded away, some new dark domains also started to nucleate at the boundaries

of fading pre-existing domains. Eventually, all of the pre-existing domains dissolved and the new dark domains stopped growing. We observed higher density of new dark domains in the region close to where pre-existing domains had been present. The observation is reasonable since the pre-existing rafts have a higher content of SM than the pre-existing light background phase does. The larger supply source of SM can locally provide more SM or Cer, resulting in higher density of new domains if the diffusion of lipid molecules is not fast enough.

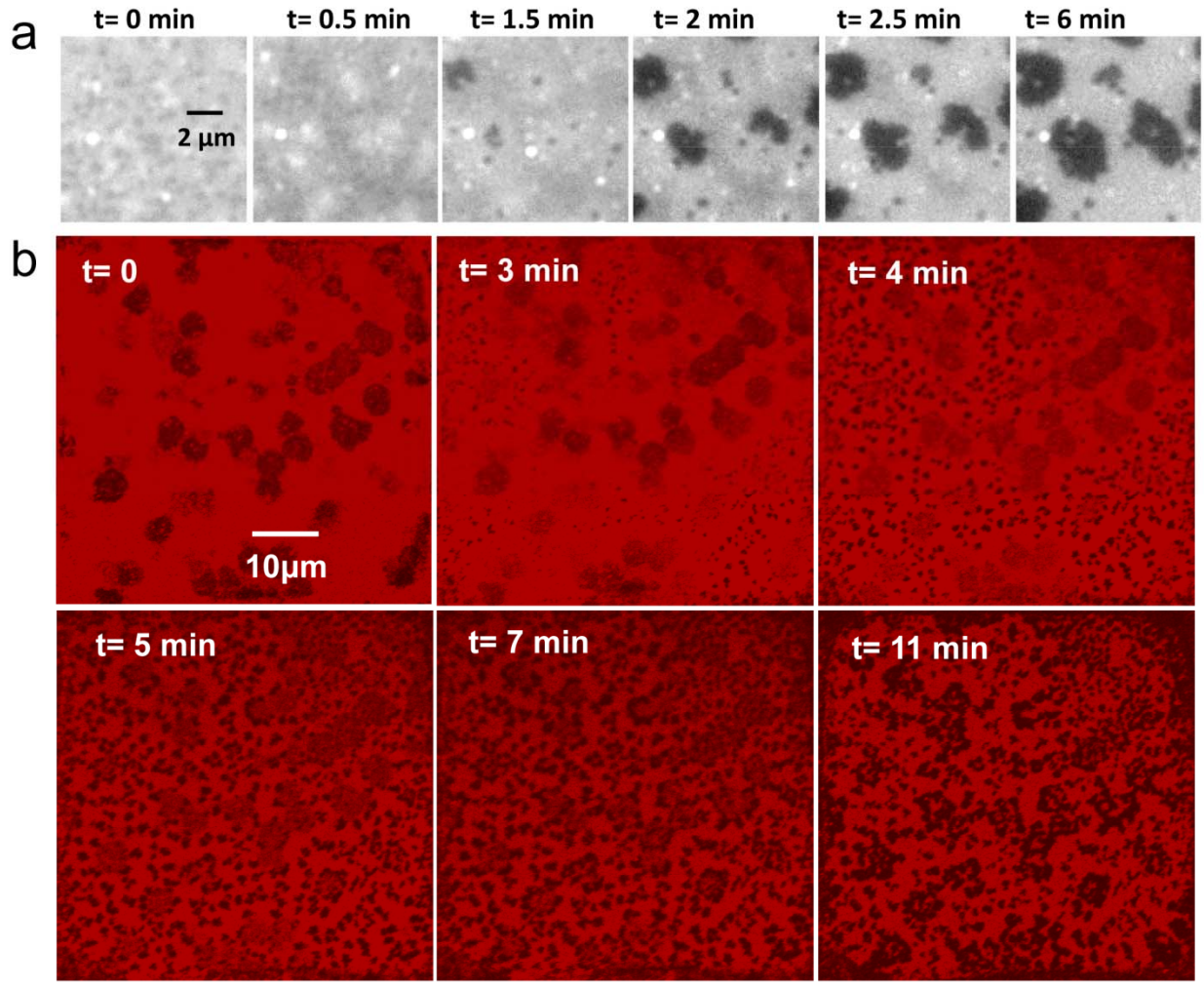

Figure 4-3. Early-stage SMase-induced morphology evolution in SLB systems (a) with sub-micron-sized pre-existing domains and (b) with micron-sized pre-existing domains. Both

membrane systems contain 40/40/20 DOPC/BSM/ Chol and 0.5 mol% of Texas-Red® DHPE and were exposed to 0.005 unit/ml SMase. (a) was obtained by a regular Nikon TE2000-E inverted microscope with a Plan Neofluar 100X/1.30 oil immersion objective. (b) was obtained in a Zeiss laser scanning module microscope with a Plan-Apochromat 63X/1.4 oil immersion objective.

The larger pre-existing domains seemed to influence the transformation time. All of the dark domains in the system with sub-micron-sized pre-existing domains were observed to nucleate and fully grow at similar times (at around t=1.5 min and t=6 min, Figure 4-3(a)). However, in the system with micron-sized pre-existing domains, we observed that the new dark domains in the region not close to those micron-sized domains nucleated at around t=2 min and grew to their full size at around t=5 min, while those new dark domains close to the micron-sized pre-existing domains started to nucleate later, at around t=4.5 min and grew to their full size at around t=10 min (supplementary Figure 4-1). The two groups of formation times probably result from the heterogeneity of SM supply. The pre-existing domains have higher SM content and can supply more SM than the background light phase can. The new domain formation depends on the local concentration of SM and Cer. If the length scale of the heterogeneity of the SM supply source is longer than the diffusion length scale during the domain formation time, the domain formation can be heterogeneous depending on the heterogeneity of SM supply. This can explain why we observed a more uniform formation of new domains in the system with sub-micron-sized pre-existing domains (shorter length scale of the heterogeneity of SM supply), but the two groups of formation time in the system with micron-sized pre-existing domains (longer length scale of the heterogeneity). In addition, the sizes of the new dark domains in the system with micron-sized

pre-existing domains are observed to be much smaller than the domains in the system with sub-micron-sized pre-existing domains. The influence of the pre-existing domain size on the spatio-temporal morphology change during the transformation will be discussed in section 4.4.2.

4.3.4. Characterization of the pre-existing domains in SLBs.

Although dark domains in model raft membranes with Texas-Red® DHPE are usually thought to be the conventional rafts rich in SM and Chol, most of the characterizations have been done in GUVs without solid support effects. The pre-existing domain morphology in SLBs has been shown to be more complex and the defects sometimes appearing in SLBs also look dark. Here, we used lysenin, a sphingomyelin-specific binding protein, to further examine the relative SM content in different phases and whether the pre-existing large dark domains in Texas-Red® DHPE images are rich in SM. Figures 4-4(d)(e)(f) shows the lysenin images of the membranes with pure DOPC and 40/40/20 molar ratio of DOPC/BSM/Chol with sub-micron-sized pre-existing domains, and the same composition with large micron-sized domains; Figures 4-4(a)(b)(c) are their corresponding images under the illumination of 0.5 mol% of Texas-Red® DHPE in the membrane. Figures 4-4(a) and (d) are used as controls to show that no labeled lysenin can be observed under the exposure time and experimental conditions we used. Figures 4-4(c) and (f) show that the micron-sized dark pre-existing domains are rich in SM and that the light background phase also contains a significant amount of SM. Comparing with the previous phase studies with GUVs[5,159], we think these large pre-existing domains are the conventional rafts rich in sphingomyelin and cholesterol, and the light background phase is the DOPC-enriched phase. When the pre-existing domains are sub-micron-sized (Figure 4-4(b)), the

resolution of the domains in the lysenin image is not sufficient and the intensity of labeled lysenin is probably the average of the intensities from the two coexistent phases (Figure 4-4(e)).

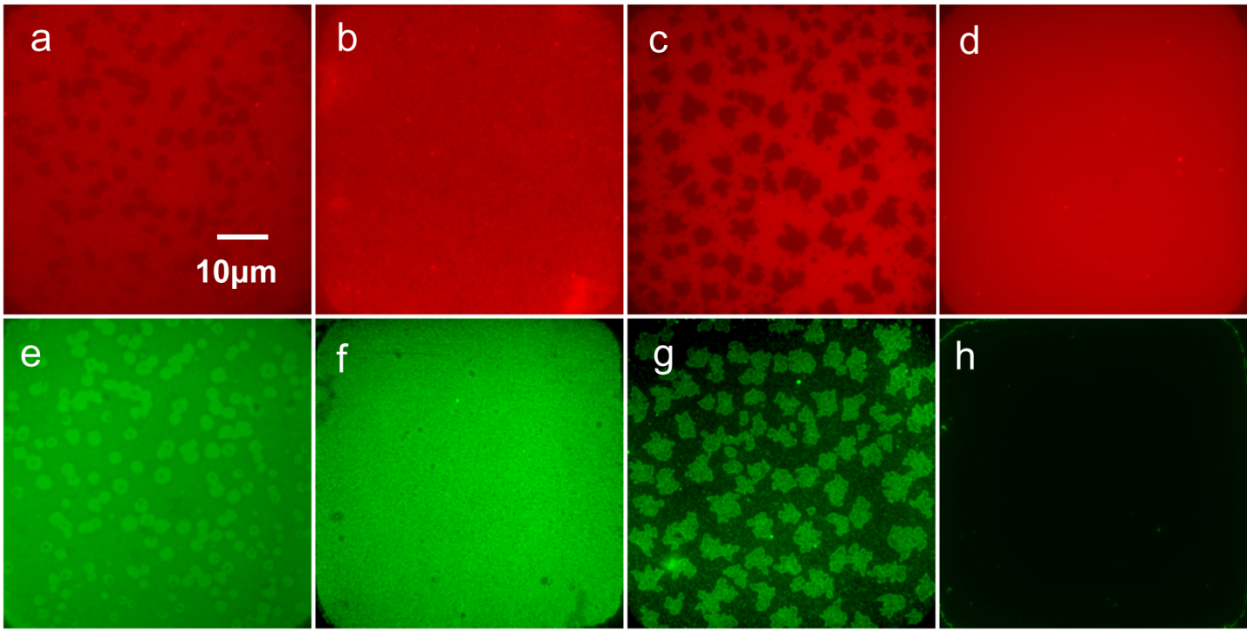

Figure 4-4. Characterization of the large micron-sized pre-existing domains in a 40/40/20 DOPC/BSM/Chol membrane and of other membrane systems for comparison. The upper row shows the images under the illumination of Texas-Red® DHPE. The lower row shows the images from the excitation of Alexa Fluor® 488-labeled lysenin, a sphingomyelin-specific binding protein. (a)(e) the 40/40/20 DOPC/BSM/Chol membrane with large micron-sized pre-existing domains; (b)(f) the 40/40/20 DOPC/BSM/Chol membrane with sub-micron-sized pre-existing domains; (c)(f) the membrane with the pause morphology after the 40/40/20 DOPC/BSM/Chol membrane was exposed to 0.005 unit/ml SMase; (d)(h) the pure DOPC membrane.

4.4. Discussion

4.4.1. The comparable SMase-induced multi-stage morphology evolution in GUVs and SLBs

We observe comparable stages of phase behavior in SLBs and GUVs. The primary difference is the mobility of domains, which is consistent with the observations in previous studies.[89,138] The high mobility of domains in GUVs provides domains the opportunity to collide with each other. Since the SM-enriched domains are probably gel domains (or solid phase), they do not coalesce but become faceted on collision, leading to the network morphology in the corresponding stage B in GUVs. On the other hand, in SLBs, the domains are pinned and do not have a chance to collide with each other, creating separated domains in stage B. One potential explanation for the pinning of domains is that the domain is a group of molecules having strong interaction with each other and their interaction with the solid support is greater than that of an individual molecule. The multibody interaction with the solid support significantly reduces the mobility of a domain in SLBs, while the mobility of each lipid molecule is less influenced. Since the overall phase changes strongly depend on the mobility of an individual molecule, they can be similar in GUVs and SLBs, while the mobility of domains in the two systems is different.

4.4.2. Transformation of pre-existing SM-Chol-rafts to SM-Cer-enriched domains

In GUV systems with micron-sized pre-existing rafts, the new dark domains separate out from the modulating pre-existing domains after the addition of SMase (Figure 4-2). The pre-existing domains are thought to be SM-Chol-enriched rafts and the new dark domains are thought to be SM-Cer-enriched domains (the SM-enriched domains introduced in chapter 3). The separating-

out observation can be explained by the competitive Chol-SM-Cer interactions. After SMase generates Cer from SM inside or at the boundary of the pre-existing SM-Chol rafts, the Cer concentration starts to be increased. Once a local Cer concentration is increased to a regime where SM-Cer-enriched domains can form, SM-Cer-enriched domains separate out from the SM-Chol-enriched rafts. This observation is consistent with the previous study reporting that Cer can replace Chol in the lipid rafts[156] and the study showing that Cer thermodynamically forms a stable phase with SM[160]. Here, we further directly visualize how the domain dynamics proceed during the competition between Chol and Cer for SM.

In SLB membranes where domains are immobile, we observe that the pre-existing domains dissolve, and the new domains nucleate in regions other than where the pre-existing rafts locate. This dissolution-nucleation observation is shown clearly in the system with large micron-sized pre-existing domains (Figure 4-3(b)). In the sub-micron-sized pre-existing-domain SLB system, the fuzziness of the pre-existing domains after the addition of SMase also indicates the domains' dissolution or disintegration. In the lysenin characterization experiment, we further confirm that the pre-existing rafts and later domains have different lysenin intensity, indicating their different SM content or different physical states. The characterization results support that the pre-existing domains in SLB systems are SM-Chol-enriched rafts, and that the later new domains are SM-Cer-enriched domains, similar to those observed in GUV systems.

Observations in both GUVs and SLBs consistently show that new SM-Cer domains form and pre-existing SM-Chol rafts disintegrate. However, unlike in GUV, where SM-Cer-enriched domains separate out from the SM-Chol-enriched rafts, the SM-Chol domains dissolve and the

SM-Cer-enriched domains nucleate in SLBs. This difference can be explained by solid support effects. The solid support has attractive forces with the lipid molecules, which may result in an energy barrier to lipids diffusing laterally to nucleate new domains. Therefore, the new SM-Cer domains do not form as readily as those in GUV systems without solid support effects. The generation of Cer from SM disturbs the interaction between SM and Chol in the pre-existing SM-Chol rafts, resulting in their dissolution or disintegration. Since the nucleation of new SM-Cer domains probably requires more energy, the released SM and Cer molecules would tend to attach to the already-nucleated SM-Cer domains and make them grow instead of nucleating to form more domains.

Another way to explain the difference is that the solid support alters the SM-Chol-Cer-DOPC phase diagram. The alteration results in the membrane system entering into a meta-stable regime when Cer is generated by SMase, and the domain formation occurs by nucleation and growth; while in GUVs, the system enters into an unstable regime and the domain formation occurs by spinodal decomposition. Blanchette et al. have reported that the domain formation in SLBs when the system temperature is decreased below the miscibility transition temperature, follows the nucleation and growth mechanism[161]; spinodal decomposition has also been reported in GUVs before[159]. Although the domain formation in our systems is induced by the composition change due to the reaction instead of by decreasing the system temperature through a thermotropic transition, the observations in the previous literature support that the two different formation mechanisms in SLBs and GUVs in our system are probably due to solid support effects.

These observations are all consistent in showing the competition between Chol and Cer for SM and exclude the possibility of the direct coalescence of the pre-existing rafts to form later large platforms. Instead, there is a reshuffling of lipid molecules during the transformation from the pre-existing morphology with SM-Chol rafts to the next morphology with SM-Cer-enriched domains. If different membrane proteins have different partition behavior in different types of domains[6,7], the reshuffling of lipid molecules also implies that the membrane proteins can easily reshuffle during the reaction-induced phase transformation. This reshuffling phenomenon can explain why the membrane proteins found in the conventional cholesterol rafts are absent in the later ceramide-containing large platforms, which could not be explained by the previous coalescence conjecture.[155]

The pre-existing raft morphology has been shown to influence the transformation rate. The SLB system with larger prepared pre-existing rafts has a slower transformation rate than the one with smaller prepared rafts does (Figure 4-3). These observations can be explained by the fact that the reshuffling of lipid molecules is limited by the interface extent of the rafts. The morphology with larger rafts contains less interface between the rafts and the DOPC-enriched phase. No matter whether Cer is generated inside a raft or at the boundary of a raft, Cer, Chol, and SM molecules need to cross through the interface to reshuffle. It can be expected that the high concentration of Chol would hinder the rate for Cer to recruit SM due to the competition. The escape of SM and Cer, or the expelling of cholesterol from the rafts, could facilitate the formation of SM-Cer enriched domains. Since a larger pre-existing domain has a smaller original interface, it is less efficient for the molecules to reshuffle and that could delay the formation rate of SM-enriched domains.

4.5. Conclusion

The overall multi-stage morphology evolution in GUVs is comparable to the one we observed in SLBs. Similar features are observed in the same order and the primary difference is the mobility of domains. The early-stage morphology evolutions in GUVs and SLBs consistently show the formation of SM-Cer-enriched domains and the disintegration of the pre-existing SM-Chol rafts.

In SLBs, the new domains are observed to form by nucleation and growth, while in GUVs, the new domains are observed to separate out from the pre-existing domains. We suggest that the solid support may alter lipid membrane's phase diagram by its attractive force with the lipid membrane and makes the system to enter into a meta-stable regime after the system composition is changed by SMase, while the system can enter into an unstable regime and undergo spinodal decomposition if there is no solid support effect. The comparisons of the morphology evolution between the SLBs with micron-sized and with sub-micron-sized pre-existing domains demonstrate that the size of pre-existing domains can influence the phase transformation rate. The influence is attributed to the reasons that the size of the pre-existing domains rich in SM can influence the length scale of heterogeneity of the SM supply, and that the size is correlated to the amount of interface where lipid molecules can exchange during the phase change.

We show how the domain dynamics proceed during the competition between Chol and Cer for SM. The results exclude the possibility of the direct coalescence of the pre-existing rafts to form later large platforms containing SM and Cer. Instead, there is a reshuffling of lipid molecules during the transformation from the pre-existing morphology with SM-Chol rafts to the next morphology with SM-Cer-enriched domains. According to the raft hypothesis, the reshuffling of

lipid molecules implies that the membrane proteins can easily reshuffle. This reshuffling phenomenon can explain why the membrane proteins found in the conventional cholesterol rafts are absent in the later ceramide-containing large platforms, which could not be explained by the previous coalescence conjecture.

Chapter 5. Tunable Spatio-temporal Membrane Morphology of Sphingomyelinase-induced Phase Transformations

5.1. Introduction

We have previously reported in chapter 3 that SMase can induce two phase transformation processes in model raft membranes, causing spatial morphology switches and multiple-time-domain ceramide generation.[157] We are further interested in how the physiologically relevant factors can tune the two phase transformation processes and thereby tune the spatio-temporal morphology change. Literature reports have suggested that lipid microdomains can influence cell signaling by creating different local environments suitable for signal transduction.[6,7,162,163] The domain types and spatial patterns appear to influence signaling quality and strength.[164-168] The sustained interval of a stationary spatial morphology could influence the signal duration.[165,169,170] The dynamics during the microdomain reorganization could also influence the kinetics of membrane protein recruitment by different microdomains. Therefore, knowledge about the spatio-temporal morphology tuning by physical processes occurring in lipid membranes may be able to provide insights into novel therapeutic opportunities. [12,154,171]

Different cell morphology at different times and multiple-time-domain ceramide accumulation[17] have been reported after SMase is activated during apoptosis in physiological studies. For the cell morphology change in the early stage of apoptosis, large micron-sized platforms for protein clustering are observed in cells of diverse origins.[35,144-148] No significant cell membrane morphological response has been reported after the large signaling platforms form. In the late stage of apoptosis, some physiological studies report the appearance of membrane bulges whose formation could be facilitated by the existence of Cer-enriched domains. [58,59,149] For the ceramide accumulation, a modest accumulation of ceramide in minutes corresponding to the early stage of apoptosis is observed in some cell systems [28,146,147,150,151], whereas a much more significant accumulation of ceramide is observed on the hour time scale corresponding to the late stage of apoptosis.[58,59,149,152] These studies indicate that the multiple-time-domain phenomena may be required for different functionality at different times in the cellular process.

The timing and sequence of these phenomena observed in cells are similar to those of the morphology switches and ceramide generation by SMase in our model systems. Although the cell morphology change and ceramide accumulation in cells could originate from many different sources in complex cell systems, their consistent timing and sequence with those observed in our model systems (with only basic components of cell membranes and SMase) suggests that the SMase's special behavior may be a contributing factor to the multiple-time-domain phenomena in cells.

Lipid membrane composition and SMase concentration have been shown to vary in different cells or under different stimulation [17,19,34,172-174], and to cause different ceramide responses [17] and

morphology change dynamics in cells.[148] In this chapter, we are interested in studying whether and how these two physiologically relevant factors can tune the spatio-temporal membrane morphology change induced by SMase in the cell-free model system with only lipid membranes and SMase.

In this study, we demonstrate that lipid membrane compositions and the concentration of SMase can be used to adjust the kinetic processes of the two SMase-induced phase transformations and therefore to the intervals and spatial patterns of the multi-stage morphology change. A wide distribution of induction time of SMase-feature nucleation is observed. The stochastic nature of the nucleation makes it difficult to quantify and compare the membrane responses caused by the different factors. In order to statistically describe SMase-feature's nucleation, we constructed a platform where numerous separated membrane systems are corralled to a size mimicking the plasma membrane size of a cell and can be observed in a single set of experiments. At a physiologically relevant concentration of SMase, the membrane composition is found to tune the formation time of SM-enriched domains and the nucleation time of SMase-feature to different extents and thereby significantly tune the stable duration of the middle pause morphology. In addition, the induction time of SMase-feature nucleation time can be significantly tuned by the concentrations of SMase-features' components. Furthermore, during the solvent-mediated phase transformation, the dissolution of SM-enriched domains is shown to be influenced by the combined effects of the reaction of SM at an SMase-feature, the diffusion of SM from SM-enriched domains to an SMase-feature, and the dissolution of SM-enriched domains.

5.2. Methods

All of the materials and methods used in this chapter are the same as those used in chapter 3 (section 3.2).

5.3. Results

5.3.1. Intervals of multi-stage morphology evolution influenced by membrane compositions

Four membrane compositions were chosen to probe the effects of the amount of sphingomyelin and the presence of cholesterol on the dynamics of the multi-stage membranes. 40 mol% SM and 20 mol% SM were chosen, based on the plasma membrane compositions in nature.[174] Cholesterol has been shown to regulate the physical properties of cell membranes primarily due to its strong interaction with sphingomyelin.[175] Therefore, to investigate the role of cholesterol in the complex phase behavior induced by SMase, we prepared lipid membrane systems with and without cholesterol.

Figure 5-1 demonstrates that the four different compositions all showed the same qualitative phenomena with distinct evolutionary stages as we reported in chapter 3: (A) growth of both SM-enriched domains and Cer-enriched domains; (B) pause morphology; (C) nucleation of an SMase-feature followed by dissolution of the SM-enriched domains and further growth of the Cer-enriched domains; (D) a stationary morphology with only the Cer-enriched domains present. In addition, the change in the relative amount of SM-enriched domains and Cer-enriched

domains with time follow the same trend as illustrated in Figure 5-2. However, the interval over which each stage persists varies significantly with the composition.

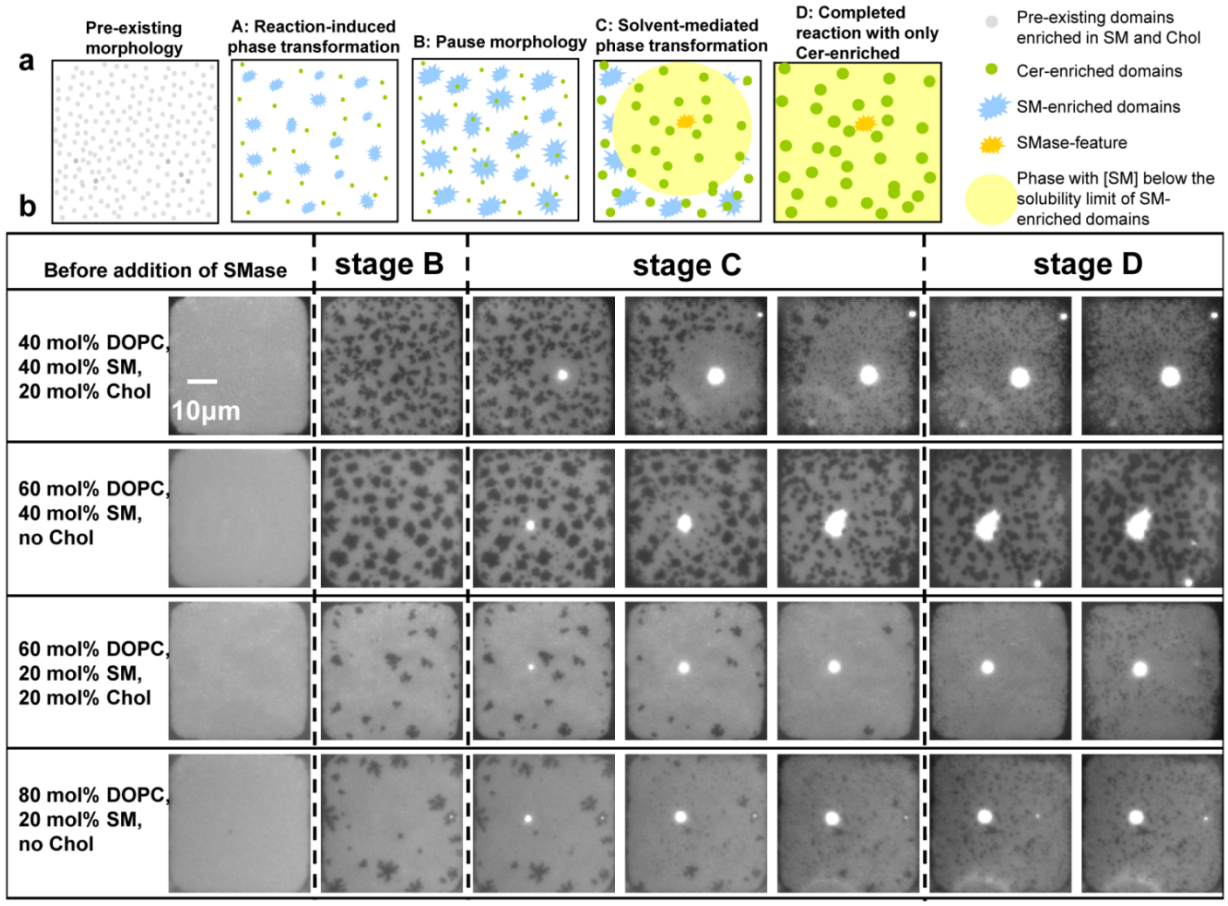

Figure 5-1. (a) Schematic illustration of the multi-stagged morphology induced by SMase. (b) Morphology evolution of lipid membranes with several physiologically relevant compositions treated with 0.005 unit/ml SMase. The features and characteristics of all four stages (A, B, C, and D) can be observed with each of the four different compositions. The duration of each of the stages was influenced by lipid membrane compositions as shown in Table 5-1.

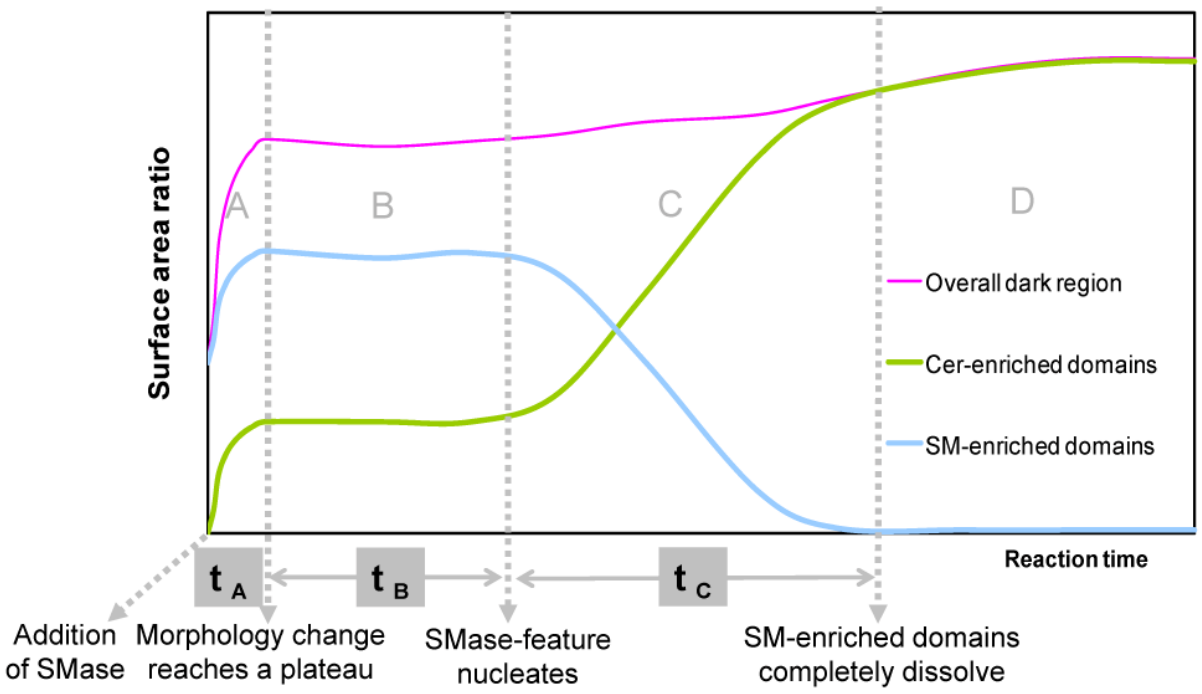

Figure 5-2. Schematic illustration of how the extents of Cer-enriched domains and SM-enriched domains in a corralled membrane system change with the stages (A, B, C, D).

Table 5-1. The duration of each stage of morphology evolution for lipid membranes with four different compositions treated with 0.005 unit/ml SMase at 37ºC. The definitions of t_A, t_B, t_C , A_B and A_D are illustrated in Figure 5-2.

Composition (mol%) (DOPC/SM/Chol)	t_A (min)	$t_{B(1/2)}$ (min)	t_C (min)
40/40/20	4.5 ± 0.3	19.5 ± 1.8	50.0 ± 4.3
60/40/0	3.2 ± 0.7	48.4 ± 2.3	48.4 ± 1.4
60/20/20	3.0 ± 0.1	60.0 ± 2.96	12.6 ± 0.9
80/20/0	2.0 ± 0.1	149.2 ± 3.7	84.4 ± 8.1

In order to compare quantitatively the durations of each of the stages in systems with different conditions, we defined t_A, t_B, and t_C, obtained as follows: t_A is the duration of stage A, and characterizes the rate at which the pre-existing morphology is transformed to the pause morphology. We used Matlab to process the morphology evolution images as described in section 5.2.5. t_A is selected to be the time at which the change of the dark region fractional area per minute became less than 2% of the overall change until that time. t_B represents the interval during which the pause morphology is sustained, and was obtained by subtracting t_A from the time of the nucleation of an SMase-feature. The transformation time of the pause morphology to the next constant morphology, t_C, was obtained by measuring the time required for all of the SM-enriched domains in a 50 μm x 50 μm corral to completely dissolve following the nucleation of the SMase-feature. Table 5-1 shows the comparison of these intervals for the four different compositions.

All of the data reported were from at least three different experiments. A single set of experiment with one composition included averages over forty-nine 50 μm x 50 μm membrane systems in separated corrals, as shown in Figure 2-10. The t_A values in Table 5-1 are the averages over nine membrane systems, three randomly picked corrals from each of the three sets of experiments. Although we found that the growth of domains in stage A is quite consistent in all of the forty-nine membrane systems, the time for SMase-features to nucleate had a wide distribution.

As introduced in section 2.6, we use the numerous number of corralled membrane systems in a single platform to capture the stochastic nature of the SMase-feature nucleation. Figure 2-10 is an example showing the images taken when only a few SMase-features had nucleated, when

SMase-features had already nucleated in half of the corrals, and when SMase-features had nucleated in all of the corralled membrane systems. Since the distribution of the induction time of SMase-feature nucleation is wide, it can cause the difficulty to compare the effects caused by different factors. By counting the number of corrals which already had SMase-features with time, we can obtain the overall statistical distribution of the induction time of the nucleation as shown in Figure 5-3. Obtaining the overall statistic distributions can allow us to fairly compare the influences from different factors, which cannot be achieved by observing only few systems. Each line in Figure 5-3 is from three sets of forty-nine-corral experiments with the same composition. The four lines represent the four different compositions. For the convenience of the quantitative comparisons, we defined $t_{B(1/2)}$ as the time when SMase-features have appeared in half of the forty-nine corrals. $t_{B(1/2)}$ of a certain composition in Table 5-1 is the $t_{B(1/2)}$ averaged over three sets of experiments.

SMase-features were found to nucleate at different locations in a corral and sometimes multiple nucleations occurred in a corral. The dissolution rate and pattern change were shown to be consistent in all of the corralled membranes with same composition until the dissolution pattern reaches the corral boundaries. However, the overall dissolution time, t_C, varies with the location of SMase in a corral. For comparison, the t_Cs in Table 5-1 were obtained from the 50 μm x 50 μm membrane systems with only one SMase-feature nucleating within the middle region of the membrane, within a radius of 10 μm from the center of a corral. The location of an SMase-feature in a corral can influence the time needed for all of the SM-enriched domains in a corral to dissolve when the diffusion is limited in the solvent-mediated phase transformation, which is a topic elaborated on in chapter 6.

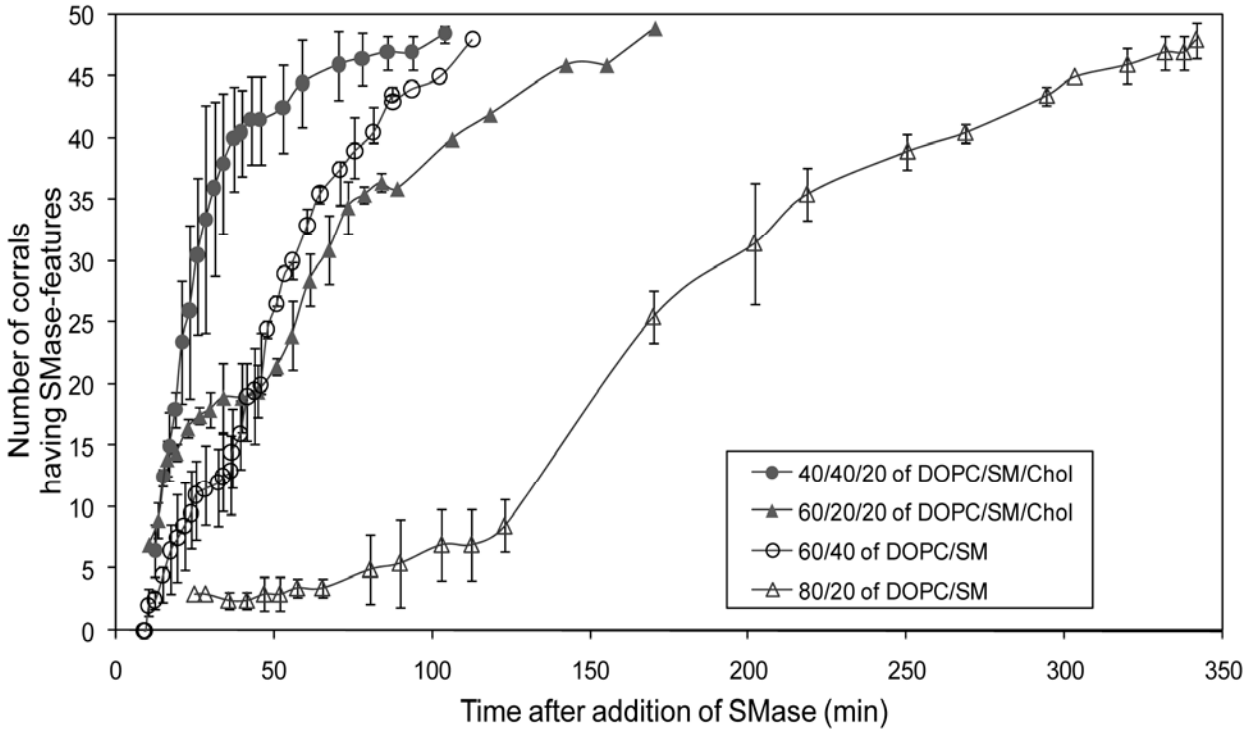

Figure 5-3. How the number of corrals having SMase-features changes with time in a set of experiment with forty-nine corrals. Each line is from three sets of forty-nine-corral experiments with the same composition. The four lines represent the four different compositions.

As shown in Table 5-1, the membrane composition influenced t_A, t_B, and t_C to different extents. All of the compositions treated with 0.005 unit/ml SMase concentration had values of t_A in the range of a few minutes. In these few minutes, all of the SM-enriched domains had already almost grown into the full size they have in the pause morphology. In addition, we observed that the SMase-features in the systems with cholesterol have significantly shorter induction time compared to those systems in the absence of cholesterol. The induction time is also shorter in membranes with 40 mol% of SM than with 20 mol% of SM. Under this SMase concentration

(0.005unit/ml), the four different compositions cause very different induction times of SMase-feature nucleation, ranging from 25 min to 2.5 hr, while only cause the formation time of SM-enriched domains ranging from 2 min to 4.5 min. The combination of the influences causes these systems to have significantly different durations of the middle pause morphology between the two transformations (represented as the values of t_B). Furthermore, we observed that the values of t_C exhibited a peculiar trend: they were similar in systems with 40 mol% SM with or without cholesterol, but quite different in the systems with 20 mol% SM. The peculiar trend can be explained by the combined effects of the SMase reaction at SMase-feature, the diffusion of SM, and the dissolution of SM-enriched domains during the solvent-mediated phase transformation process at stage C, as will be discussed later.

Another interesting thing to mention is that the appearance of the SMase-features is different in membranes with and without cholesterol. We have previously shown that the SMase-feature in 40/40/40 DOPC/SM/Chol membranes is a 3-D feature extruded out from the membrane into its solution side and has a smooth outer surface (Figure 3-10). Here, using the low exposure time of Texas-Red ® DHPE images, we observed that the outer surface of an SMase-feature in 60/40 DOPC/SM membranes is needle-shaped (Figure 5-4(b)). An SMase-feature in 40/40/20 DOPC/SM/Chol membranes observed under the same conditions is also shown here for the comparison (Figure 5-4(a)).

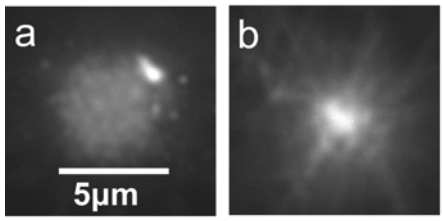

Figure 5-4. The appearance of SMase-features in stage D in the membranes treated with 0.005 unit/ml SMase. The images were obtained by incorporating 0.5 mol% of Texas-Red® DHPE into membranes before the SMase reaction. (a) The membrane contains 40/40/20 DOPC/SM/Chol before addition of SMase. (b) The membrane contains 60/40 DOPC/SM in the absence of cholesterol before addition of SMase.

5.3.2. Induction time of SMase-feature nucleation

The formation of SMase-features usually takes minutes to hours. The induction time for the SMase-feature is important since it triggers the domain reorganization and determines how long the pause morphology can be sustained. The observed time elapse prior to the formation of an appreciable amount of the new phase after the initial supersaturation of the components in the parent phase is a characteristic feature of first-order phase transitions in three-dimensional systems. It is attributed to the threshold nature of the dependence of nucleation rate on the degree of supersaturation.[142] We have reported previously that SMase-features are composed of SMase, Cer and SM, and they nucleate in the DOPC-enriched phase. Here, we are interested in whether the higher supersaturation of the substances composing the SMase-features can increase the nucleation rate and reduce the induction time in this two-dimensional lipid membrane system.

5.3.2.1. Influence of SMase concentration on the induction time

First, we examined the influence of different SMase concentrations, ranging from 0.001-0.05 unit/ml, to 40/40/20 DOPC/SM/Chol membranes. The induction time is shown to decrease from 95 min to 10 min while the SMase concentration was increased (Table 5-2(a)-(d)). The increased SMase concentration in 60/20/20 DOPC/SM/Chol membranes is also shown to decrease the induction time (Table 5-2(f)-(g)).

In most of the experiments, we removed SMase from the bulk solution after the membrane is exposed to the SMase solution for two minutes (Table 5-2(a)-(d), (f)-(g)). The procedure is probably more physiologically relevant than immersing the membrane systems under a SMase solution over the whole process, since SMase translocates to the plasma membrane only upon stimulations in nature.[22] In this procedure, the supply of SMase to form the SMase-features can only be from the SMase binding to the membrane during this two-min period and remaining after the washing step. The high binding rate and slow dissociation rate of SMase[126,127] probably allow a significant amount of SMase still binding to the membrane after the washing step. Although we do not know how much SMase binds to the membrane with this experimental procedure, we applied the same procedure to all of the SMase concentrations we tested to ensure that the bulk concentration can have a positive correlation to the amount of SMase binding to the membrane if the membrane had not saturated with SMase. We also prepared a system exposed to 0.05unit/ml SMase for the overall process (Table 5-2(e)). Immersing the membrane in SMase solution results in faster nucleation and shorter induction time than exposing the membrane to the same concentration for two minutes does. This result is probably due to the fact that immersing SMase

in bulk solution can keep the equilibrium of SMase binding and prevents the extent of dissociation occurring after the SMase solution is removed.

The average number of SMase-features in a corral is found to increase with the SMase concentration we used (Figure 5-5 and Table 5-2). The trend is the opposite to the trend of induction time. It is noteworthy that the overall extent of all of the SMase-features in a corral is quite consistent in the systems with different SMase concentrations, even in the membrane system immersed in an SMase solution for the duration of the overall process (Figure 5-5). The consistent extents are found in confined corrals with same membrane composition but the extent is less in the membranes with less pre-existing SM content (Figure 5-5, the comparison between (a)-(e) and (f)-(g)).

Table 5-2. The induction time for SMase-feature nucleation and the number of SMase-feature per 50 μm x 50μm corral in the final constant morphology: (a)-(d) when the 40/40/20 DOPC/SM/Chol membranes were exposed to different SMase concentrations (0.001-0.05 unit/ml) for 2 min; (e) when the 40/40/20 DOPC/SM/Chol membrane was exposed to 0.05 unit/ml SMase during the overall process; (f)-(g) when the 60/20/20 DOPC/SM/Chol membranes were exposed to different SMase concentrations (0.001 and 0.005 unit/ml) for 2 min.

Composition	40/40/20 of DOPC/SM/Chol					60/20/20 of DOPC/SM/Chol	
SMase concentration (Unit/ml)	**(a)** 0.001 two min	**(b)** 0.005 two min	**(c)** 0.01 two min	**(d)** 0.05 two min	**(e)** 0.05 Overall	**(f)** 0.001 two min	**(g)** 0.005 two min
$t_B(1/2)$ (min)	95	20	15	11	10	> 360	60
Average # of SMase-features	1	1.4	2.3	2.8	4.5	1	1

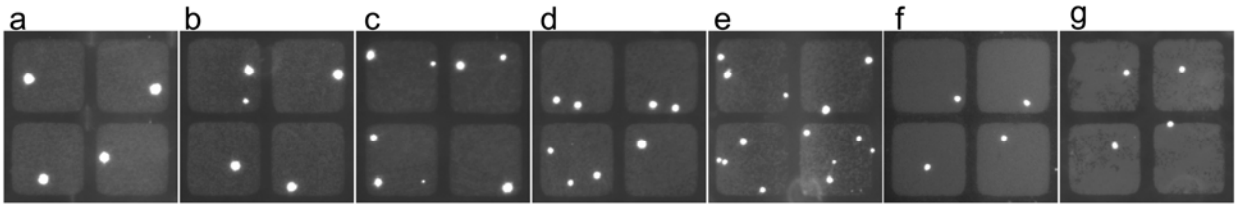

Figure 5-5. The representative corralled membrane images of the final constant morphology when the membranes are exposed to the different conditions listed in Table 5-2. The bright ring in (e) is the diffraction pattern from the SMase-feature on the opposite surface of the 50 μm height microchannel.

5.3.2.2. Influence of ceramide, and sphingomyelin on the induction time

We examined the influence from ceramide and sphingomyelin by preparing a series of membranes with different amounts of pre-existing Cer, ranging from 5 mol% to 20 mol% with the total amount of Cer and SM equal to 40 mol%. We assumed that the Cer concentration in the DOPC-enriched phase would also increase with the prepared Cer content. The induction time is about 4 min in 20 mol% Cer membranes, 10 min in 10 mol% Cer membranes, and 20 min in 5 mol% Cer membranes. SMase-features formed almost immediately in 20 mol% Cer membranes, and the induction time increased with the decreased in pre-existing Cer (Figure 5-6). All of the membrane systems with pre-existing Cer have shorter induction times than the system without any pre-existing Cer (t_A+t_B~ 24 min for 404020 DOPC/SM/Chol membranes from Table 5-1). It was difficult to obtain stable supported lipid bilayers with more than 20 mol% Cer due to Cer's special molecular shape and hydrophobicity. We were not able to further increase the Cer content in the system with Cer and SM equal to 40 mol% to further explore whether the induction time would start to increase when the SM amount became the limiting factor in the

system instead of the Cer amount. However, when we reduced the SM content to zero, we did not observe the formation of SMase-features up to 3 hr in membranes with 60 mol% of DOPC and 20 mol% of Cer and 20 mol% of cholesterol (Figure 5-7), indicating that the presence of SM is also crucial for the formation of an SMase-feature.

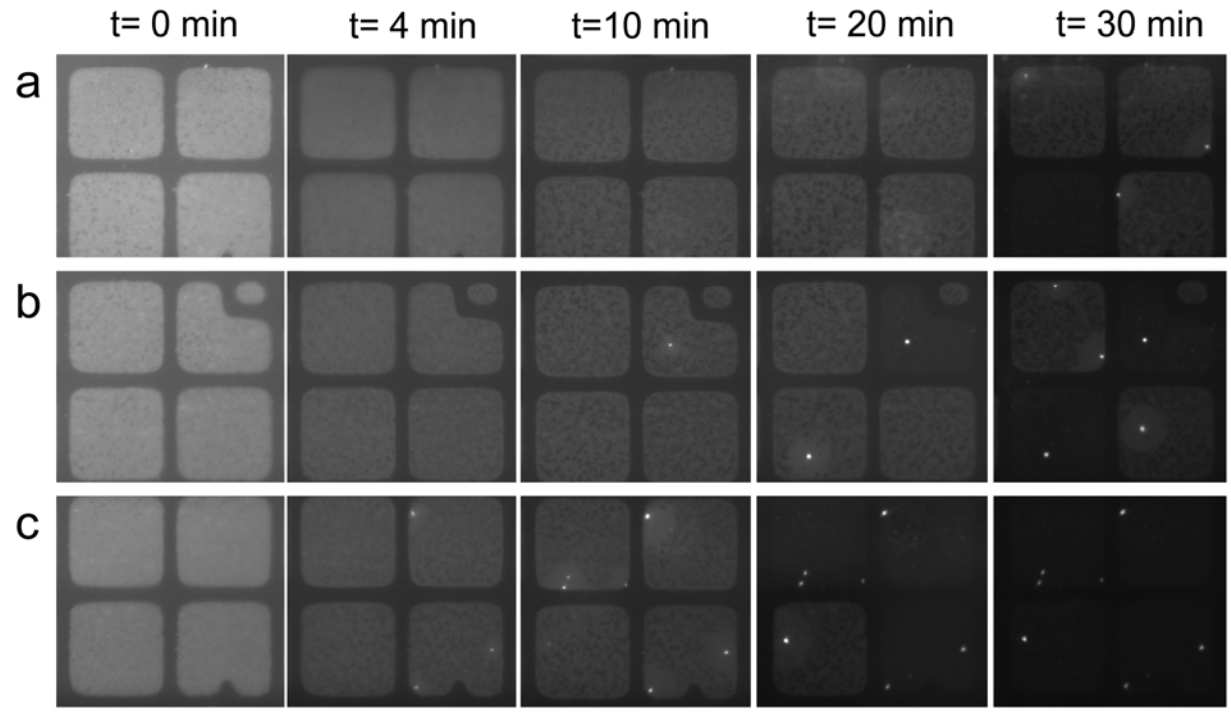

Figure 5-6. Morphology evolution of membranes with various amount of pre-existing ceramide after addition of 0.005 unit/ml SMase. All of the membrane systems contain 40/40/20 molar ratio of DOPC/(SM+Cer)/Chol, and having (a) 5 mol% Cer, (b) 10 mol% Cer, and (c) 20 mol% Cer. The darkness occurring in the late stage after SMase-features form is probably due to the instability of the membranes.

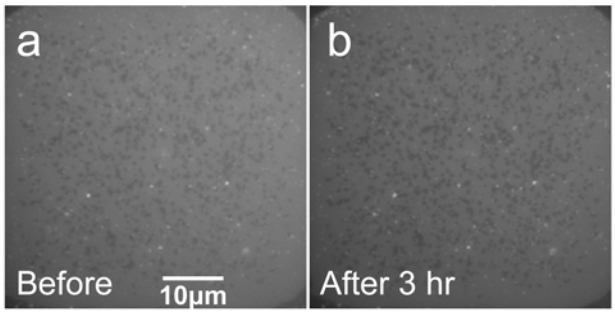

Figure 5-7. No SMase-features can be observed three hours after the addition of 0.005 unit/ml SMase to the membrane containing 20 mol% of ceramide but no sphingomyelin (60/20/20 molar ratio of DOPC/Cer/Chol). The small bright spots were probably the non-specifically bound small vesicles which had existed before the addition of SMase. The dark domains shown in both before and after addition of SMase are probably ceramide-enriched domains since no domains can be observed in the control (DOPC membranes containing 20 mol% of cholesterol).

5.4. Discussion

5.4.1. Influence of cholesterol on the duration of middle pause morphology

The t_As of the four different compositions (40/40/20, 60/40/0, 60/20/20, and 80/20/0 molar ratio of DOPC/SM/Chol) are all in the range of a few minutes. The membranes with cholesterol have statistically longer t_As than those without cholesterol (about 1 minute difference) (Table 5-1). London et al. have shown that Cer can replace Chol in rafts where SM and Chol originally had strong interaction.[156] Recent studies have also shown that Cer can recruit SM to form SM-enriched domains.[134,155] The longer t_A may be due to the fact that competition between ceramide and cholesterol for SM delays the formation process of SM-enriched domains. The pre-existing

rafts in supported lipid bilayers in this study are too small to demonstrate how the pre-existing rafts are transformed to SM-enriched domains. We will in the future use giant unilamellar vesicles with larger pre-existing rafts and supported lipid bilayers with larger annealed pre-existing rafts prepared by a different protocol to further investigate the transformation process of pre-existing rafts to SM-enriched domains.

The membranes with cholesterol are shown to have much shorter induction time of SMase-feature nucleation than the membranes without cholesterol (Table 5-1). In contrast to the minute-scale differences of t_As, these induction times have hour-scale differences. Figure 5-4 also shows that cholesterol influences the appearance or shape of SMase-features. The different shape suggests that cholesterol involves the phase behavior of SMase-features and probably reduces the energy barrier of the nucleation. In addition, as we will show in a more complete analysis in the next paragraph, when we applied the Avrami equation (describing the appearance rate of a new phase from a previous one) to the nucleation of SMase-feature, the Avrami exponents (an indication of nucleation type, dimensionality and geometry of the formed entities) are shown to be different in the membranes with and without cholesterol. The difference of the Avrami exponents also suggests that cholesterol influences the formation mechanism of SMase-features.

Overall, the presence of cholesterol seems to delay the formation of SM-enriched domains and speed up the SMase-feature nucleation at physiologically relevant concentrations of SMase. The combination of the influences leads to a decrease of the stable duration of the middle pause morphology between the two SMase-induced phase transformations. In addition, the influence of cholesterol on the induction time of SM-enriched domain nucleation is at the time scale of hours,

which is more significant than the influence on the formation time of SMase-enriched domains (at the time scale of minutes).

5.4.2. Analyses of distribution of induction time of SMase-feature nucleation by Avrami equation

The Avrami equation has been used widely to describe the kinetics of the appearance of a new phase from a parent phase upon change of conditions. It is originally derived using the general geometry of growing precipitates and includes the effect of depletion of the parent phase during the transformation.[176] Thereby, it provides a quantitative description of the kinetics of a transformation in a medium where the total amount of reactants is restricted. The equation follows the general form:

$$f = 1 - exp(-kt^n) \tag{5-1}$$

where f is the transformed fraction, t is time after the transformation starts, k is a constant usually depending on the overall transformation rate, and n is the Avrami exponent which is usually an indication of nucleation type, dimensionality and geometry of the formed entities. For fitting data, the equation is usually rearranged to the following form:

$$log\big(-ln(1-f)\big) = logk + n\,log(t) \tag{5-2}$$

In this study, we would like to describe the kinetics of the appearing time of SMase-features (the distribution of the induction time). In our systems, we have forty-nine corrals in a set of experiment, and each corral region can be viewed as a discrete region with the same initial condition. Once the SMase, SM, and Cer in the DOPC-enriched phase are transformed to an

observable-sized SMase-feature in a corral, we view that the parent phase in that corral is already transformed to its new phase. Figure 5-3 is the transformation-time curve obtained under this definition for the four different membrane compositions. We plot the data in a ln(-ln(1-f)) vs. ln(t) plot (Figure 5-8(a)). We found that the data between -0.6 and 0.6 in the y axis, ln(-ln(1-f)), (corresponding to the nucleation occurring in the 20^{th} corral and in the 41^{th} corral in a 49-corral-membrane system) can be fitted well to straight lines in a ln(-ln(1-f)) vs. ln(t) plot (Figure 5-8(b)). In addition, the two membrane compositions with 20 mol% cholesterol have similar Avrami exponents close to 1.5 (the slopes), and the two with no cholesterol have similar Avrami exponents close to 1.9.

In phase transformation of systems with simple components, the Avrami exponent (n) is directly related to nucleation type, dimensionality and geometry of the formed entities. The intercept (k) is viewed as a transformation rate constant.[176] In our systems with multiple complex-molecular-structured reactants, we have not been able to tell the meanings of these numbers. However, it is interesting that the Avrami exponents of the two membrane systems with cholesterol are consistent and so do the two with no cholesterol (Figure 5-8(b)). The shift of Avrami components from 1.9 to 1.5 in the presence of cholesterol suggests that cholesterol may influence the structure of the formed SMase-feature. The obtained intercepts probably reflect the averaged induction time and their numbers are consistent with the representative induction times ($t_{B(1/2)}$s) shown in Table 5-1.

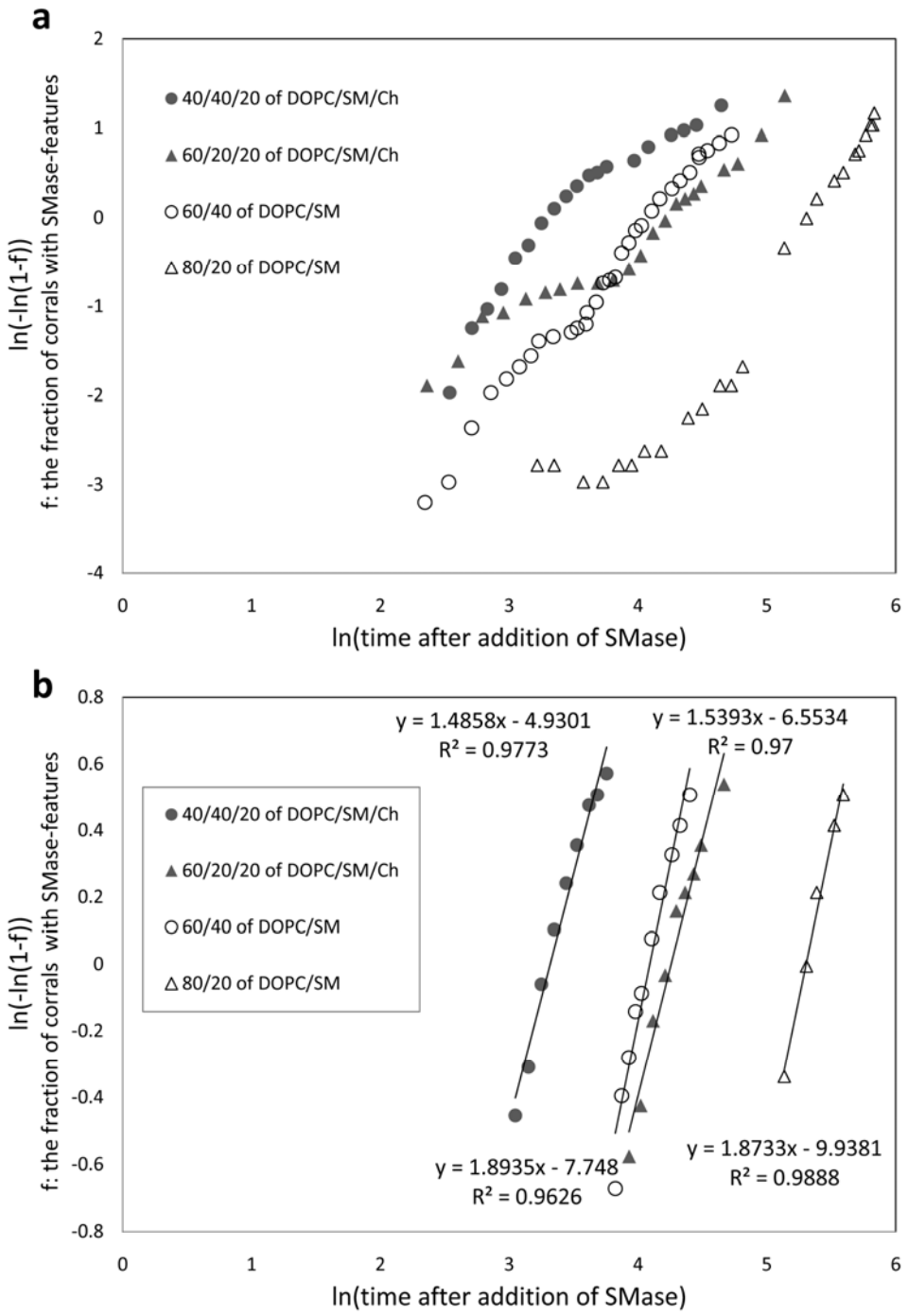

Figure 5-8. Fitting the kinetics of the appearing time (or the induction time) of SMase-features in forty-nine corralled membranes to the Avrami equation. The fraction of corrals with SMase-features (f) is averaged from three sets of experiments corresponding to the averaged number of corrals having SMase-features in the transformation-time plot in Figure 5-3 but in a fraction form.

(a) The plot describing the transformation of all of the forty-nine corralled membranes. (b) Part of the plot with the data between -0.6 and 0.6 in the y axis (corresponding to the nucleation occurring in the 20th corral and in the 41th corral in a forty-nine-corral-membrane system). The upper two linear fitting equations and R-squared values are for 40/40/20 and 60/20/20 DOPC/SM/Ch membranes (from left to right, respectively). The lower two fitting equations are for 60/40 and 80/20 DOPC/SM/Ch membranes (from left to right, respectively).

The data obtained before the nucleation occurring in the 20th corral and after the 41th corral are found to have smaller slopes than those between the 20th corral and 41th corral, especially for those membrane systems with 20 mol% of SM. The multiple segments of this type of graph have been observed in previous studies in materials with more complex molecular structures, such as polymers, lipids, and proteins.[177-179] In our systems, the early deviation and inconsistency may be due to the impurity existing in some of the corrals. The impurity may be able to serve as nuclei and reduce the energy barrier of nucleation in some of the corrals, causing them to have SMase-features earlier than the case if no impurity exists. The impurity effect could become more obvious in the systems with longer intrinsic induction times, and could become embedded in the major transformation events in the shorter-induction-time systems. This conjecture explains why the membrane systems with longer induction times (membranes with 20 mol% of SM), would have small-slope lines before the 20th corral, but the membrane systems with smaller induction times would not (Figure 5-8(a)).

5.4.3. Tuning of induction time of SMase domain's nucleation by SMase, Cer, and SM.

The induction time for the SMase-feature is important since it determines when the morphology can be further transformed by the SMase-induced solvent-mediated phase transformation. We have reported previously that SMase-features are composed of SMase, Cer and SM, and they nucleate in the DOPC-enriched phase. In this study, we further demonstrate that the induction can be tuned by the concentrations of its components. Increasing the concentrations of SMase solutions in a physiologically relevant range or increasing a pre-existing ceramide amount is shown to significantly reduce the induction time (Table 5-2 and Figure 5-6). In addition, no SMase-features can be observed in 60/20/20 DOPC/Cer/Chol membranes, indicating that the presence of SM is also required for the formation of SMase-features (Figure 5-7). One thing to notice is that there are still some experimental difficulties in decoupling the effects from SM and Cer. Although we can control pre-existing membrane compositions and SMase bulk concentrations, we have not been able to control the concentrations of SM and of Cer in the DOPC-enriched phase in the pause morphology stage, which depends on the DOPC-SM-Cer-chol phase diagram and the kinetic process of the reaction-induced phase transformation. In this study, we assume that increasing the pre-existing ceramide content can also increase the Cer concentration in the DOPC-enriched phase, but the exact concentration would require a technique to quantify the composition in a single bilayer. Despite the experimental difficulty, we demonstrate that the induction time of SMase-feature nucleation is tunable by the concentration of its components.

The number of SMase-features may be different in each corral but the overall extent of SMase-features is found to be consistent in the membrane systems with same composition even if

treated with different SMase concentrations (Table 5-2). However, the overall extent is significantly less in the membranes with less pre-existing SM (Table 5-2, the comparison between the 40/40/20 and 60/20/20 DOPC/SM/Chol membrane sets). In the membrane systems confined to a certain size with certain amount of lipids, this situation indicates that SM but not SMase is the limiting substance for the formation of SMase-features in the range of SMase concentrations we used. The average number of SMase-features in a corral is found to increase with the SMase concentration, which suggests that the nucleation rate is increased with the increased SMase concentration. This result is consistent with the general correlation obtained in the nucleation of substances in three-dimensional systems: the faster nucleation rate corresponds to a shorter induction time.[142] Once an SMase-feature nucleates, it grows and consumes SM. The decreased supersaturation level of SM and SMase probably makes it more difficult for additional SMase-features to nucleate in the same corral, which could explain why only one SMase-feature was observed per corral in many of the systems.

5.4.4. Spatial morphology change during the solvent-mediated phase transformation

We observe the dissolution of SM-enriched domains starts from the region where SMase-features locate and the dissolution propagates in the radial direction away from the SMase-features in all of the four compositions we tested. However, a sharp dissolution ring is only observed in the membranes with 40 mol% of SM (with or without cholesterol), while a more gradual dissolution occurs in membranes with 20 mol% of SM (Figure 5-1, stage C; or the illustration in Figure 5-9). Since SM-enriched domains can start to dissolve only when the surrounding SM concentration gets below the solubility limit, we can approximately tell where

the saturating concentration front already reached by observing how far the SM-enriched domains were affected and started to dissolve. Conceptually, a sharp dissolution ring implies that the dissolution rate is fast so that once the concentration is below the saturating point, the domains can readily dissolve. The gradual dissolution implies that the dissolution is not fast enough compared to the change rate of saturating concentration front. In the next paragraph, we will use a simple model to describe the spatial concentration profile of SM and discuss how the SM-enriched domain morphology would change in the extreme cases when different kinetic factors in the solvent-mediated phase transformation are limited.

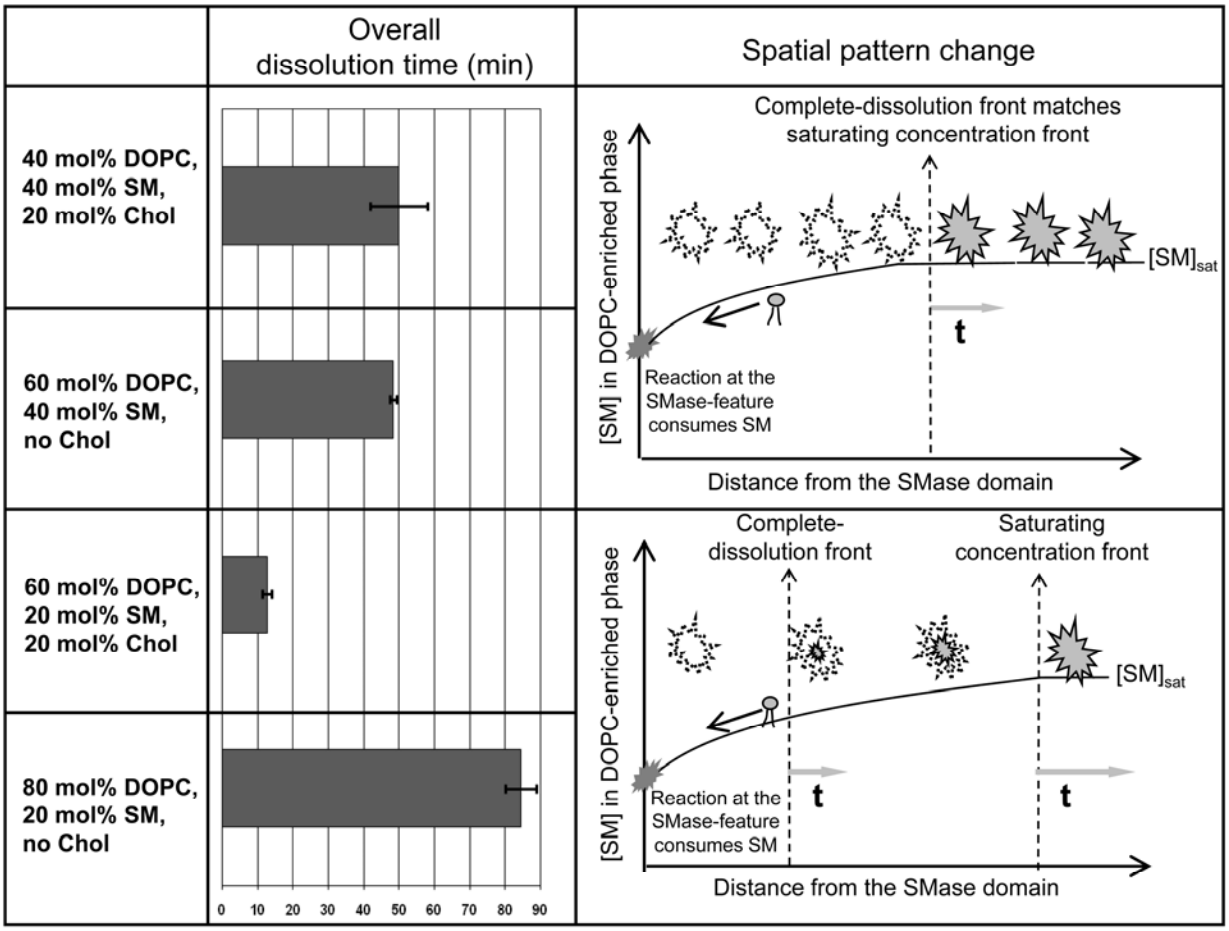

Figure 5-9. Comparison of how the spatial morphology change and the interval for all of the SM-enriched domains to dissolve during the solvent-mediated phase transformation. The

illustrations in the right column show the spatial morphology changes and SM concentration profile in the DOPC-enriched phase along the radial direction from an SMase-feature. The solid irregular objects represent SM-enriched domain, and the dashed irregular lines are used to indicate the SM-enriched domains which have dissolved. The object at y axis represents an SMase-feature. The black arrow indicates the diffusion direction of SM molecules. The gray arrows indicate the movement direction of the concentration front and the completely dissolution front. SM-enriched domains start to dissolve when they are exposed to SM concentration below their solubility. The sharp dissolution front occurs only when the saturating SM concentration front matches the completely-dissolution front. If the saturating SM concentration front moves faster than the completely-dissolution front, shrinkage of SM-enriched domains from their entire boundaries can be observed.

To discuss the spatial morphology change, which is directly correlated to spatial SM concentration profile, we use the conservation equation of SM molecules and apply Fick's law to describe the diffusion flux of SM molecules in the 2-D fluid DOPC-enriched phase. We have shown in our previous study that the reaction occurring in the DOPC-enriched phase is negligible during the solvent-mediated phase transformation and that there is no flow in the DOPC-enriched phase to cause convection. Therefore, only the accumulation term and the diffusion flux term need to be considered in the conservation equation. If we assume this system is analogous to dilute binary mixture solutions, the conservation equation of SM in the 2-D polar coordinate may be expressed as [180]:

$$\frac{\partial[SM]}{\partial t} = D\left(\frac{\partial^2[SM]}{\partial r^2} + \frac{1}{r}\frac{\partial[SM]}{\partial r}\right) \tag{5-1}$$

where t is time after an SMase-feature nucleates, r is the distance from the center of the SMase-feature, and D is the diffusion coefficient of SM in the DOPC-enriched phase.

We have shown in our previous study that the reaction is found to primarily occur at SMase-features, the dissolution occurs at the boundaries of SM-enriched domains, and the resulting concentration gradient drives the diffusion of SM molecules from the SM-enriched domains to SMase-features[157]. In this simplified model, we assume there is no accumulation of SM molecules on the interfaces and that SM molecules do not diffuse on the interfaces. Therefore, based on the conservation of SM, at a point on the interface of the SMase-feature and the DOPC-enriched phase, the diffusion flux of SM to the SMase-feature should be equal to the consumption rate of SM due to the enzymatic reaction. At a point on the interface of the SM-enriched domains and the DOPC-enriched phase, the diffusion flux of SM from the SM-enriched domains should be equal to the releasing rate of SM due to the dissolution of SM-enriched domains. Therefore, at the boundaries, the following equations need to be satisfied:

$$-D\frac{d[SM]}{dn_G}\Big|_{\mathrm{G}} = -f_G(k_G,[SM]_G) \tag{5-2}$$

$$-D\frac{d[SM]}{dn_D}\Big|_{D} = f_D(k_D,[SM]_D,[SM]_{sat}) \tag{5-3}$$

where $[SM]_G$ and $[SM]_D$ are, respectively, the SM concentrations at the interface of the SMase-feature and the DOPC-enriched phase, and at the interface of the SM-enriched domains and the DOPC-enriched phase. n_G and n_D are the normal vectors pointing outwards from the SMase-

feature and the SM-enriched domains at their boundaries. $[SM]_G$, $[SM]_D$, n_G , and n_D are all functions of locations of the boundaries. They can be expressed as functions of *r*, and θ in the polar coordinate, and change with time due to SMase-feature's growth and SM-enriched domains' dissolution. f_G represents the consumption rate of SM at the interface of the SMase-feature and the DOPC-enriched phase due to the enzymatic reaction, and is probably a function of $[SM]_G$ and the catalytic rate constant of the SMase-feature (k_G). f_D represents the releasing rate of SM at the interface of the SM-enriched domains and the DOPC-enriched phase due to the dissolution, and is probably a function of $[SM]_D$, the saturating SM concentration ($[SM]_{sat}$), and the dissolution constant of SM-enriched domains (k_D).

This problem is complicated by the moving boundaries due to the dissolution, the complex geometry of the boundaries, and the lack of knowledge of the reaction kinetics of SM at SMase-features and of the dissolution kinetics of SM-enriched domains. Here, we make the subsequent assumptions and simplifications in order to obtain an approximate correlation of the SM concentration profile to the rate constants of the three major events in the solvent-mediated phase transformation process. First, although we lack knowledge of the reaction kinetics and the dissolution kinetics, the higher SM concentration should increase the reaction rate and the lower SM concentration should provide a larger driving force for dissolution. We assume first-order kinetics of reaction and dissolution, and f_G and f_D may be expressed:

$$f_G = k_G[SM]_G \tag{5-4}$$

$$f_D = k_D([SM]_{sat} - [SM]_D) \tag{5-5}$$

Second, we assume that the process is at pseudo-steady state, which is valid when the boundaries move sufficiently slowly and the diffusion profile is similar to that found at a stationary interface; therefore, the left term of Equation 5-1 is set to be zero. Furthermore, to simplify the geometry, we set the center of the SMase-feature as the origin, and that the SMase-feature has an average size with average radius equal to R_G. The geometry of SM-enriched domains is simplified by only considering the points on the boundary of SM-enriched domains whose normal vector is towards the origin, and by setting the boundary at an average distance from the origin (R_D). In addition, since we assume that the boundaries move sufficiently slowly, the boundary conditions may be expressed as:

$$\text{at } r = R_G,\ [SM] = [SM]_G \qquad (5\text{-}6)$$
$$r = R_D,\ [SM] = [SM]_D$$

where $[SM]_G$ and $[SM]_D$ need to satisfy Equations 2 and 3.

After Equation 1 is solved based on the simplified boundary conditions, the concentration profile in the DOPC-enriched phase in the radial direction away from the SMase-feature can be expressed as:

$$[SM] = \frac{[SM]_D \ln(\frac{r}{R_G}) + [SM]_G \ln(\frac{R_D}{r})}{\ln(\frac{R_D}{R_G})} \qquad (5\text{-}7)$$

Substituting Equation (7) into Equations (2) and (3) at the boundaries, we obtain

$$\frac{[SM]_D - [SM]_G}{[SM]_G} = \frac{k_G}{D} R_G \ln(\frac{R_D}{R_G}) \quad (5\text{-}8)$$

$$\frac{[SM]_D - [SM]_G}{[SM]_{sat} - [SM]_D} = \frac{k_D}{D} R_D \ln(\frac{R_D}{R_G}) \quad (5\text{-}9)$$

We use the simplified model to consider the extreme cases when the processes are reaction-limited, diffusion-limited, or dissolution-limited. The SM concentration profiles and their corresponding spatial morphology changes in the three extreme cases are illustrated in Figure 5-10. When the overall process is limited by diffusion (or $D << k_D, k_G$), the concentration difference ($[SM]_D$-$[SM]_G$) needs to be large, the SM concentration at the SMase-feature ($[SM]_G$) needs to be low, and the SM concentration at the SM-enriched domain ($[SM]_D$) needs to be close to the saturating SM concentration ($[SM]_{sat}$) to satisfy Equation 8 and 9. Similarly, when the process is limited by reaction (or $k_G << D, k_D$), the concentration difference needs to be small, and both $[SM]_G$ and $[SM]_D$ need to be large but cannot exceed $[SM]_{sat}$; therefore, the concentration profile is relatively uniform and stays at its high level close to $[SM]_{sat}$. When the process is limited by dissolution (or $k_D << D, k_G$), the concentration difference needs to be small, and both $[SM]_G$ and $[SM]_D$ need to be low; therefore, the concentration profile is relatively uniform and stays at its low level.

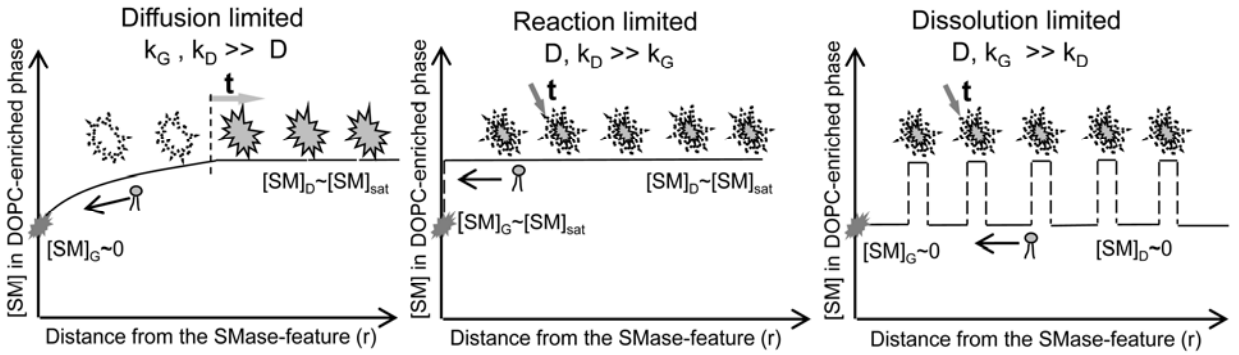

Figure 5-10. Illustrations of the SM concentration profile with the corresponding spatial morphology changes in the extreme cases when the solvent-mediated phase transformation process is limited by the diffusion, by the reaction at SMase-features, or by the dissolution at the boundaries of SM-enriched domains based on pseudo-steady state analysis. The gray irregular objects represent SM-enriched domain, and the dashed irregular lines are used to indicate the part of the SM-enriched domains which have dissolved.

The simplified pseudo-steady state model suggests that the sharp dissolution front can be observed when the process is limited by diffusion. The amount of SM that can be transferred is limited, so that SM concentration around the SM-enriched domains remains at its highest level, the saturating SM concentration, until the material fully dissolves and is transferred away. When the reaction and/or dissolution become more dominant in the process, the model suggests that the concentration becomes more homogenized. Consequently, a more isotropic dissolution should be observed.

Therefore, the observed sharp dissolution front (the anisotropic dissolution in the membrane systems with 40 mol% of SM) probably indicates that their solvent-mediated phase transformation process is limited by diffusion of SM molecules in the DOPC-enriched phase.

However, the sharp dissolution front was not observed in the membrane systems with 20 mol% of SM. The SM-enriched domains do not just dissolve primarily from the side facing the SMase-feature, but dissolve from the entire boundaries, although the SM-enriched domains closer to the SMase-feature still dissolve completely earlier than those farther from the SMase-feature (illustrated in Figure 5-9). Therefore, the process is no longer just limited by diffusion, and either reaction or dissolution or both processes become important in influencing the spatial change and the overall transformation rate. This situation is intuitively reasonable since the changed composition might alter the composition of the SMase-feature and hence reduce its catalytic performance, and the dissolution capability can also be decreased due to the reduced interface for dissolution, while the diffusion coefficients are similar in all of our membrane systems. According to the pseudo-steady state model, if the reaction is relatively important or limited in the system, we should observe the entire concentration profile to be closer to the saturating SM concentration; if the dissolution is more important, we should observe the entire concentration profile to be quite low. However, we have not been able to measure the SM concentration profile in membranes with 20 mol% SM by the intensity of labeled-lysenin due to the large background noise compared to the signal. More advanced techniques for characterizing the spatial compositions of lipid membranes would provide additional insights into the governing processes.

Although both the anisotropic dissolution and isotropic dissolution of SM-enriched domains are observed, Cer-enriched domains are observed to grow isotropically in all of the compositions we experimented on. The uniform growth indicates that the ceramide concentration is quite homogeneous in a corral. Because the ceramide is primarily supplied from the SMase-feature where SM can be converted to Cer, the Cer needs to diffuse to other region to homogenize its

concentration in a corral. The observation, therefore, indicates that the growth rate of the Cer-enriched domains is relatively slower than the diffusion rate of ceramide molecules in the DOPC-enriched phase.

5.4.5. Temporal control during the solvent-mediated phase transformation

It takes about 50 min to dissolve all of the membranes with 40 mol% SM with and without Chol (Table 5-1 or Figure 5-9). We have shown that the process in the membranes with 40 mol% SM is limited by diffusion. We measured the lateral diffusion coefficient of lipid molecules in the SLBs by fluorescence recovery after photobleaching (FRAP) and found that it is 1.91 μm^2/sec for the membrane with 40/40/20 molar ratio of DOPC/SM/Chol, and 2.45 μm^2/sec for the membrane with 60/20/20 molar ratio of DOPC/SM/Chol. According to the pseudo-steady state analysis, the characteristic time for the concentration profile with 25 μm penetration depth, half length of a corral, to have significant change is about five minutes. The t_Cs we obtained in the membranes with 40 mol% SM are much longer than the characteristic time. These results are reasonable and expected since the SM-enriched domains store large amounts of SM and release SM only when the surrounding SM concentration is below the solubility limit. The driving force of diffusion depends on SM concentration in the DOPC-enriched phase but not on the overall amount of SM. Since SM concentration in the DOPC-enriched phase cannot be higher the saturating SM concentration, the overall diffusion rate is limited by the saturating SM concentration no matter how much SM stored in SM-enriched domains. Therefore, more time is needed to deliver the extra amount of SM released from SM-enriched domains to SMase-features.

We expect membranes with 20 mol% of SM to have the transformation intervals shorter than the intervals in membranes with 40 mol% of SM, since less SM needs to be processed. For 60/20/20 DOPC/SM/Chol membranes, the t_C is 12 min, which is larger than 5 min and less than 50 min, as expected. However, the t_C of the membranes without cholesterol is 84 min, longer than 50 min. Our conjecture is that the catalytic performance of their SMase-features may be much lower in 80/20 DOPC/SM membranes due to the change of the SMase-features' composition.

5.5. Conclusion

We have previously reported that SMase can induce a reaction-induced phase transformation and a solvent-mediated phase transformation, causing membrane switches and multiple-time-domain ceramide generation in model raft membranes. Herein, we further demonstrate that the interval and the spatial change of the stages in the overall process can be adjusted by physiologically tunable parameters, specifically, membrane composition and SMase concentration, based on the two identified phase transformation processes. A platform with large numbers of corralled membranes in parallel enabled us to overcome the difficulties of quantification and comparison of the phenomena between different systems caused by the large variation of the SMase-feature nucleation time.

At a physiologically relevant concentration of SMase, the presence of cholesterol seems to delay the formation of SM-enriched domain and speed up the SMase-feature nucleation, leading to a

shorter duration of the middle pause morphology. The outer appearance of SMase-features and the fitting of induction time distribution of SMase-feature nucleation to the Avrami equation suggest that cholesterol influences the formation mechanism of SMase-features.

We have previously shown that SMase-features, which can trigger the solvent-mediated phase transformation, contain SMase, sphingomyelin, and ceramide. Here, we further show that the induction time of SMase-feature nucleation decreases with the increased supersaturating level of SMase and with the increased pre-existing ceramide amount. Sphingomyelin is also required for the formation of the SMase-feature. The result suggests that the starting time of the morphology reorganization in a 2-D membrane system could be also tuned by the supersaturating level of its components, which is similar to the nucleation of substances in 3-D systems.

Furthermore, the interval of the solvent-mediated phase transformation is suggested to be primarily influenced by the interplay of the reaction rate of SM at SMase-features, the diffusion rate of SM from SM-enriched domains to SMase-feature, and the dissolution rate of SM-enriched domains. When decreasing SM content in the lipid membrane from 40 mol% to 20 mol%, the physiologically relevant range, the spatial pattern change shifts from anisotropic dissolution of SM-enriched domains to a more isotropic dissolution. The pseudo-steady state model suggests that the anisotropic dissolution indicates the solvent-mediated phase transformation process in the 40 mol% SM membrane is limited by diffusion, and the more isotropic dissolution in the 20 mol% SM membrane indicated that reaction and dissolution could also become important in that case.

Chapter 6. Modeling of the SMase-induced Solvent-Mediated Phase Transformation

6.1. Introduction

During the solvent-mediated phase transformation (stage C), we have primarily observed the occurrence of three processes. The first one is the dissolution of SM-enriched domains. The second one is the reaction at an SMase-feature. This reaction is thought to occur primarily at the SMase-feature during stage C, since the other features except the SMase-feature are also observed in the previous pause morphology (stage B) but no significant generation of product can be found. The third process is the diffusion of SM molecules from SM-enriched domains to the SMase-feature. The lysenin characterization in chapter 3 showed that there is a decrease of SM concentration from the dissolving SM-enriched domains towards the SMase-feature. The SM concentration in the DOPC-enriched phase changes from an initial uniform saturating SM concentration at stage B to a final uniform lower concentration at stage D.

We generally observe that the dissolution of SM-enriched domains starts from the region where SMase-features locate, and propagates in the radial direction away from the SMase-features. However, the dissolution pattern change has been observed to vary with membrane composition. A sharp dissolution ring is observed in the membranes with 40 mol% of SM (60/40/0 and 40/40/20 DOPC/SM/Chol), while a more gradual dissolution occurs in membranes with 20

mol% of SM (80/20/0 and 60/20/20 DOPC/SM/Chol) (chapter 3). We developed a simple pseudo-steady-state model in chapter 5 to provide a possible explanation for the observations. However, the model did not consider the system's complex geometry and was used to describe the concentration qualitatively in the extreme cases when any one of the three kinetic processes is dominant.

To further discuss the spatial pattern change of SM-enriched domains, which is directly correlated to the spatial SM concentration profile, we use the conservation equation of SM molecules to solve the time-dependent SM concentration profile in the 2-D fluid DOPC-enriched phase. We solve the model numerically instead of analytically due to the complex geometry and the moving boundary of the system. The multiple and dispersed interfaces of the interested DOPC-enriched region with the SM-enriched domains cause the difficulty in describing the boundary of the relevant region in mathematical equations. In addition, the extent of the boundaries with the SM-enriched domains decreases with time. The boundary moving with time is implicit since it depends on the local SM concentration, which changes while the boundary moves. In this chapter, we use Comsol software to numerically solve the spatial concentration profile. This software uses finite element method, a numerical technique for finding the approximate solution of partial differential equations. The method tessellates the relevant region into meshes and updates the variables at each mesh spatio-temporally according to the governing equations and boundary conditions.

There are two methods which can be combined with Comsol software to deal with moving boundary problems. One is the updating marker point method and the other is the level set

method. The updating marker point is a conventional method in which the boundaries are discretized into many marker points, whose locations are updated after each time step.[181,182] The level set method views the boundary as the zero-level set of a function describing the global boundary change trajectory.[182] The traditional updating method can be accurate for the small-scale motions of interface, but suffers from the topological changes if the morphology change is complex, resulting in local singularity problems during the simulation. The level set method is more powerful for dealing with all kinds of interface motions, including the appearance and disappearance of the interface. However, the level set method usually requires a larger number of meshes around the moving boundary than the updating method.

In this study, we choose to use the updating marker point method since it was expected to take less computing time than the level set method in our system with numerous moving boundaries. Since the boundary motion in our system is relatively predictable, we incorporate remedy algorithms in Matlab coding to solve the potential singularity problems in the traditional marker point method. Under the condition that the rate constants associated with the intrinsic enzymatic reaction at an SMase-feature and with the dissolution of SM-enriched domains are still unknown, the non-dimensionalization helps us to obtain a general model and insights into how each of the kinetic processes in the solvent-mediated phase transformation can influence the morphology change. We demonstrate the characteristics of all the possible scenarios of the model. Our experimental observations can be fit well to the modeling results. The modeling results also provide inights into parameters which is difficult to measure.

6.2. Model Description

6.2.1. 2-D membrane morphology description

The solvent-mediated phase transformation starts after an SMase-feature nucleates. Figure 6-1 illustrates a typical membrane morphology we observe at the beginning of the phase transformation. The membrane system is confined in a corral. The blue objects are SM-enriched domains and the yellow object is an SMase-feature. To simplify the system, both the domains are set to be round and the SMase-feature is set to nucleate at the center of the membrane system. The normal directions of the corral boundary, the SMase-feature boundary, and the SM-enriched domain boundary are set as n_1, n_2, and n_3, respectively. The normal directions vary with the geometry of the objects and are functions of the coordinates.

In this model, we have the dissolution occurring at the boundaries of the SM-enriched domains, the enzymatic reaction at the boundary of the SMase-feature, and the diffusion in the DOPC-enriched phase. The overall phase transformation occurs in 2-D. Although we have shown that the SMase-feature has a 3-D structure, it connects to the DOPC-enriched phase in the membrane through a 2-D boundary (shown in the characterization results by confocal microscopy in chapter 3). Here, we only consider the flux of SM from the 2-D boundary as the effective reaction consumption from the SMase-feature.

We assume that the dissolution is first-order and its driving force is the difference between the local SM concentration, to which the SM-enriched domains are exposed, and the saturating SM concentration. Therefore, the dissolution rate (R_D) per unit length of SM-enriched domain boundary can be expressed as $R_D=k_D([SM]_{sat}-[SM])$, where k_D is the rate constant of the first-

order dissolution, $[SM]_{sat}$ is the saturating concentration of the SM-enriched domains, and [SM] is the local SM concentration in the DOPC-enriched phase. During the dissolution of SM-enriched domains, the rates of motion of the boundaries depend on their local [SM]. For a certain portion of boundary with small length Δs, there is a movement of Δh in Δt in the normal direction of the local interface, as illustrated in Figure 6-1.

We assume that the enzymatic reaction is also first-order and proportional to the local SM concentration in the DOPC-enriched phase once the concentration is above a threshold. Therefore, the consumption rate (R_G) per unit length of SMase-feature boundary can be expressed as $R_G=k_G([SM]-[SM]_0)$, where k_G is the effective rate constant of the first-order reaction, $[SM]_0$ is the threshold concentration, and [SM] is the local SM concentration in the DOPC-enriched phase. We further assume that the 2-D boundary of the SMase-feature does not change significantly through the whole process and therefore hold it constant.

The consumption of SM at the SMase-feature boundary decreases its local SM concentration and the resulting concentration gradient drives the diffusion of SM molecules from the SM-enriched domains to SMase-features.

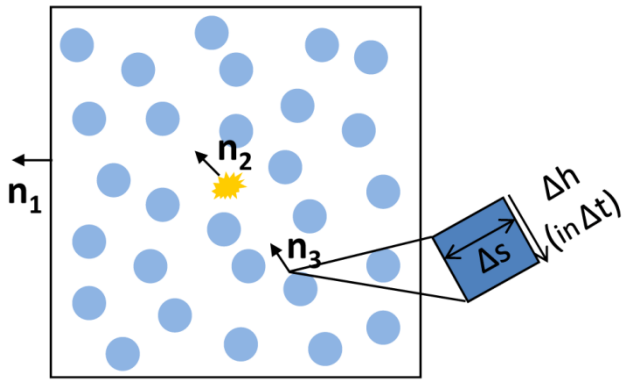

Illustration object	Phase identity	Sphingomyelin concentration	Outward normal direction at the boundary	Associated rate constant	Associated rates
White region	DOPC-enriched phase	[SM]	N/A	N/A	N/A
|	Corral boundary	no flux	n1	N/A	N/A
✸	SMase-feature	$[SM]_0$	n2	k_G	$k_G([SM]-[SM]_0)$
●	SM-enriched domains	$[SM]_{solid}$	n3	k_D	$k_D([SM]_{sat}-[SM]_0)$

Figure 6-1. Schematic illustration of the model of a system during the solvent-mediated phase transformation.

Table 6-1. Definition of the symbols used in the model.

Symbol	Meaning	Unit	Property
[SM]	Sphingomyelin concentration in DOPC-enriched phase	Amount/area	Dependent variable (function of location and time)
$[SM]_{sat}$	Sphingomyelin concentration in the DOPC-enriched phase at the boundary equilibrating with SM-enriched domains	Amount/area	Fixed parameter
$[SM]_0$	The threshold sphingomyelin concentration for the enzymatic reaction to occur at an SMase-feature	Amount/area	Fixed parameter
$[SM]_{solid}$	Density of SM inside SM-enriched domains	Amount/area	Fixed parameter
k_G	First-order enzymatic reaction rate constant at the 2-D boundary of SMase-features	Length/time	Fixed parameter
k_D	First-order dissolution rate constant of SM-enriched domains	Length/time	Fixed parameter
D	Diffusivity of SM in the DOPC-enriched phase	Area/time	Fixed parameter
h	Motion of the interface of SM-enriched domains in the normal direction	Length	Dependent variable (function of

			location and time)
Δs	Arc length of the local boundary of SM-enriched domains	Length	Fixed parameter
n_1	Normal direction of corral boundaries	Length	Variable (function of location)
n_2	Normal direction of SMase-feature boundaries	Length	Variable (function of location)
n_3	Normal direction of SM-enriched domain boundaries	Length	Variable (function of location and time)

6.2.2. Governing Equations

The aim of this model is to obtain the SM concentration profile in the DOPC-enriched phase, which is directly related to the dissolution and therefore the spatial pattern change of membrane morphology. We use the conservation equation of SM molecules and apply Fick's law to describe the diffusion flux of SM molecules in the 2-D fluid DOPC-enriched phase. There is no convection flow in the DOPC-enriched phase in the corralled membrane system. Only the accumulation term and the diffusion flux term need to be considered in the conservation equation. If we assume this system is analogous to dilute binary mixture solutions, the conservation equation of SM in the 2-D polar coordinates may be expressed as [180]:

$$\frac{\partial[SM]}{\partial t} = D\left(\frac{\partial^2[SM]}{\partial r^2} + \frac{1}{r}\frac{\partial[SM]}{\partial r}\right) \tag{6-1}$$

where t is time after an SMase-feature nucleates, r is the distance from the center of the SMase-feature, and D is the diffusion coefficient of SM in the DOPC-enriched phase. The initial condition (at t= 0) of this solvent-mediated phase transformation can be expressed as:

$[SM]=[SM]_{sat}$ (everywhere in the DOPC-enriched phase) (6-2)

There are three sets of boundary conditions, and we assume that there is no accumulation of SM molecules on the interfaces and that SM molecules do not diffuse on the interfaces. First, there is no SM flux through the corral boundaries (Equation 6-3). Second, at any point on the interface of the SM-enriched domains and the DOPC-enriched phase, the diffusion flux of SM from the SM-enriched domains should be equal to the releasing rate of SM due to the dissolution of SM-enriched domains (Equation 6-4). Third, at a point on the interface of the SMase-feature and the DOPC-enriched phase, the diffusion flux of SM to the SMase-feature should be equal to the consumption rate of SM due to the enzymatic reaction (Equation 6-5).

$$-D\frac{d[SM]}{dn_1}\Big|_{corral} = 0 \tag{6-3}$$

$$-D\frac{d[SM]}{dn_2}\Big|_{SMase-feature} = -R_G = k_G([SM]_0 - [SM]) \tag{6-4}$$

$$-D\frac{d[SM]}{dn_3}\Big|_{SM-domains} = R_D = k_D([SM]_{sat} - [SM]) \tag{6-5}$$

The meanings of the symbols can be found in Table 6-1. The normal vectors, n_2 and n_3, point outwards from the SMase-feature and the SM-enriched domains at their boundaries, respectively. The normal vector, n_1, of the corral boundaries points outwards from the membrane system. These normal vectors are all functions of locations of the boundaries and can be expressed as functions of r and θ in polar coordinates. The vector n_3 also changes with time due to SM-enriched domains' dissolution.

During the dissolution of the SM-enriched domains, we assume that SM molecules do not accumulate at and diffuse tangentially along the interfaces. The local disappearing rate of the SM-enriched domains times the SM density in the SM-enriched domains should be equal to the local dissolution rate or the local releasing rate of SM per unit length of the boundary, which is driven by the concentration below the saturating concentration. The motion rate of a local boundary with length Δs can be expressed as:

$$\left.\frac{\partial h}{\partial t}\right|_{\substack{\text{at a point at the boundary}\\ \text{of SM-enriched domains}\\ \text{with their geometry at time t}}} \Delta s([SM]_{solid} - [SM]_{sat}) = k_D([SM]_{sat} - [SM])\Delta s \tag{6-6}$$

where the symbols are defined in Table 6-1.

6.3. Non-Dimensionalization

The derivation in the previous section yields four variables: concentration, time, the distance from the SMase-feature, and the dissolution length, and three important constants associated with the dissolution, the reaction, and the diffusion: k_D, k_G, and D. Although the diffusivity of the lipids in the membrane system is known, the dissolution rate constant of SM-enriched domains and the effective intrinsic reaction rate constant at the boundary of SMase-feature are unknown. To obtain a generalized model and to gain further insight into the interplay of the three rates, we apply non-dimensionalization to analyze how the change of the ratio of the reaction rate, the dissolution rate, and the diffusion rate can influence the process. The introduced non-dimensional variables and parameters are shown in Table 6-2.

Table 6-2. Summary of the scaled variables and model parameters for analyzing the overall pattern change. The definitions of the other symbols can be found in Table 6-1.

Variables	$C = \frac{[SM]-[SM]_0}{[SM]_{sat}-[SM]_0}$	Scaled SM concentration in the DOPC-enriched phase
	$\tau = \frac{t}{R^2/D}$	Scaled time
	$\eta_1 = \frac{n_1}{R}$	Scaled length in the normal direction of the corral boundary
	$\eta_2 = \frac{n_2}{R}$	Scaled length in the normal direction of the SMase-feature boundary
	$\eta_3 = \frac{n_3}{R}$	Scaled length in the normal direction of the SM-enriched domain boundary
	$\hbar = \frac{h}{R}$	Scaled displacement of the SM-enriched domain boundary
Parameters	$Da_G = \frac{k_G}{(D/R)}$	Ratio of reaction rate to diffusion rate
	$Da_D = \frac{k_D}{(D/R)}$	Ratio of dissolution rate to diffusion rate
	$K = \frac{[SM]_{sat}}{[SM]_{solid}-[SM]_{sat}}$	Ratio of amount of SM stored in the SM-enriched domains to amount stored in the fluid DOPC-enriched phase

After the non-dimensional variables and parameters are substituted into the equations introduced in the last section, the governing equation can be rewritten as:

$$\frac{\partial^2 C}{\partial \eta^2} + \frac{1}{\eta}\frac{\partial C}{\partial \eta} = \frac{\partial C}{\partial \tau} \tag{6-7}$$

The initial condition can be rewritten as:

$$c = 1 \tag{6-8}$$

The boundary conditions can be expressed as:

$$\left.\frac{\partial C}{\partial \eta_1}\right|_{\substack{corral \\ boundary}} = 0 \tag{6-9}$$

$$\left.\frac{\partial C}{\partial \eta_2}\right|_{\substack{SMase-feature \\ boundary}} = \frac{k_G}{(D/R)} C = Da_G C \tag{6-10}$$

$$\left.\frac{\partial C}{\partial \eta_3}\right|_{\substack{SM-domain \\ boundary}} = \frac{k_D}{(D/R)}(1-C) = Da_D(1-C) \tag{6-11}$$

The equation of motion of the SM-enriched domain boundary can be expressed as:

$$v_n = \frac{\partial \hbar}{\partial \tau} = \frac{k_D}{(C_{solid}-1)R(D/R^2)}(1-C) = \frac{1}{(C_{solid}-1)} Da_D(1-C) = KDa_D(1-C) \tag{6-12}$$

6.4. Algorithms for tracking boundary and redistributing marker points

To solve the moving boundary problem, we combine Comsol, which solves the spatial concentration profile by finite element method, with the algorithms for tracking boundary and redistributing marker points in Matlab coding (as shown in Appendix). After discretizing the boundary into a set of marker points, we obtain the final solutions by iteratively following several steps: (1) Sending the geometry of the interested region to Comsol solver in order to obtain the spatial concentration profile; (2) Updating the location of each marker point by the equation of motion of the boundary, dependent on the concentration; (3) Redistributing the marker points to increase the robustness of simulation and to prevent local singularity problems.

6.4.1. Comsol solver for the spatial concentration profile

The initial morphology and three sets of boundary conditions are entered into a Comsol software: the insulation condition for the corral boundary; the leaving SM flux equal to the effective reaction rate at the SMase-feature boundary; and the entering SM flux equal to the dissolution rate of SM-enriched domains at the SM-enriched domain boundary. The Comsol software is used to solve the spatial concentration profile developed after a small time step with the temporarily fixed boundaries. After the concentration profile is obtained, the boundaries can be updated with the algorithms introduced in the following sections. The new boundaries result in a new geometry of the region of interest, which will be entered into the Comsol solver again to obtain the concentration profile after another smaller time step. This iterative process discretizes the concentration profile development and the dissolution process with time steps. The smaller time steps typically result in more accurate results, although more computation time is required.

6.4.2. Updating the marker points by the equation of motion of the boundary

The displacement of each marker point on the boundary is calculated by the equation of motion of the SM-enriched domain boundary (Equation 6-6). The updating in the numerical method is implemented by discretizing the Lagrangian form of the equation of motion.

$$\Delta h = k_D \frac{([SM]_{sat} - [SM])}{([SM]_{solid} - [SM]_{sat})} \Delta t \tag{6-19}$$

The above equation can provide the magnitude of the displacement, which is in the normal direction of the local interface, towards SM-enriched domains. We approximate the normal

direction of the interface at a marker point (P_i) by using the two neighboring marker points (P_{i-1} and P_{i+1}). First, the two neighboring marker points can be used to approximate the tangential unit vector ($n_{i,t}$).

$$n_{i,t} = \frac{P_{i+1} - P_{i-1}}{|P_{i+1} - P_{i-1}|} \quad (6\text{-}20)$$

Then, since the normal vector and the tangential vector are perpendicular to each other, their inner product is zero. The direction of the normal vector can be calculated by the following equation:

$$n_{i,t} \times n_{i,n} = 0 \quad (6\text{-}21)$$

Finally, whether the normal vector is towards SM-enriched domains can be judged by the clockwise or counterclockwise order of the marker points.

6.4.3. Redistributing the marker points

Initially, we have *n* marker points at the boundary of each SM-enriched domain. After the locations of marker points are updated, they may become closer together or further apart. Sometimes, undesired topological changes also occur. To ensure robust simulation, we adapt the algorithms developed by Chen et al.[181] to check and redistribute the marker points each time they are updated (Figure 6-3).

When the two consecutive marker points, P_i and P_{i+1}, are too far apart, a new marker point is added and the marker point numbering is updated using the following algorithm (Figure 6-3(a)):

$$P_{j,new} = P_{j,old} \quad \text{for } 1 \leq j \leq i \quad (6\text{-}22)$$

$$P_{j,new}=(P_{j,old}+P_{j+1,old})/2 \quad \text{for } j = i+1 \tag{6-23}$$

$$P_{j,new}=P_{j-1,old} \quad \text{for } j \geq i+2 \tag{6-24}$$

When the two consecutive marker points, P_i and $P_{i+1,}$ are too close together, they are replaced by one new marker point and the marker point numbering is updated using the following algorithm (Figure 6-3(b)):

$$P_{j,new}=P_{j,old} \quad \text{for } 1 \leq j \leq i-1 \tag{6-25}$$

$$P_{j,new}=(P_{j,old}+P_{j+1,old})/2 \quad \text{for } j = i \tag{6-26}$$

$$P_{j,new}=P_{j+1,old} \quad \text{for } j \geq i+1 \tag{6-27}$$

If a topological change occurs between P_i and P_{i+m}, all of these points are eliminated and replaced with a new marker point at their algebraic average position. The marker point numbering is updated using the following algorithm (Figure 6-3(c)):

$$P_{j,new}=P_{j,old} \quad \text{for } 1 \leq j \leq i \tag{6-28}$$

$$P_{j,new} = \sum_{k=i+1}^{i+m-1} P_{k,old}/(m+1) \quad \text{for } j = i+1 \tag{6-29}$$

$$P_{j,new}=P_{j+m,old} \quad \text{for } j \geq i+2 \tag{6-30}$$

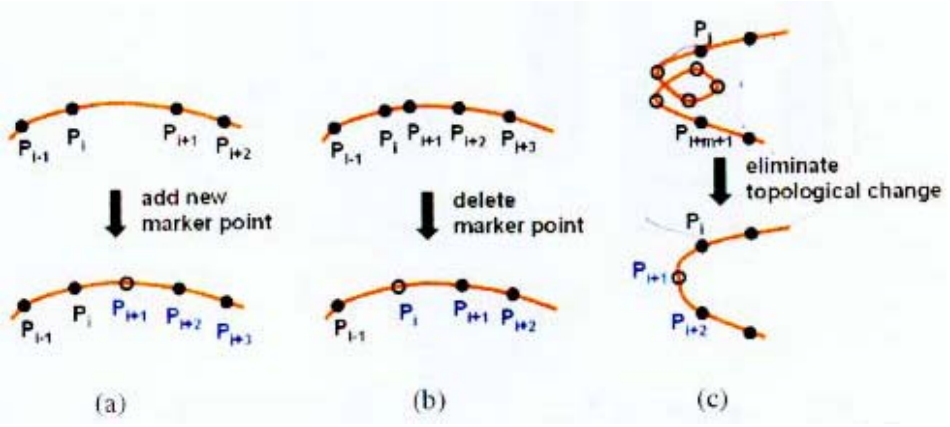

Figure 6-2. Algorithms for redistributing of marker points.[181]

After updating the marker points each time, we use an algorithm to check whether the number of marker points is already less than a certain threshold number. Since the redistributing algorithms shown above have ensured a moderate density of marker points on a boundary, the decreasing number of marker points generally indicates the reduction of the boundary. If the number of marker points drops below a certain threshold, we can expect that the corresponding SM-enriched domain will fully dissolved in the next time step. In this case, we can remove all of the marker points for that boundary to prevent potential singularity problems. These singularity problems can occur if the displacements of the marker points cross over the previous boundaries in the next time step, which is due to the artifact from discretization and does not occur in reality. It can be expected that the threshold number depends on the interval of the time step used. In our algorithm, we usually set the threshold number as one-twentieth of the number of original marker points, while the interval of the time step is set to be one-hundredth of the overall simulation time.

6.5. Results

After using non-dimensionality in equations to solve the overall spatial pattern change of SM-enriched domains in a corral (section 6.3.1, Equations 6-7 to 6-12), we only have three parameters to describe our systems: Da_G (representing the reaction rate constant to the diffusivity), Da_D (representing the dissolution rate constant to the diffusivity), and K (representing the SM amount stored in SM-enriched domains compared to the amount which can be stored in the DOPC-enriched phase). These three parameters all have their important physical meanings and can be used to divide system phenomena into groups. Here, we study how these

three parameters can influence the spatial pattern change. The modeling results are compared with the morphology changes observed in our experiments to further understand the physical processes occurring in the SMase-induced solvent-mediated phase transformation.

6.5.1. Varying Da_D and Da_G: the ratio of the reaction, dissolution, and diffusion rates

In our model of the solvent-mediated phase transformation, there are three kinetic processes occurring in series: reaction, diffusion and dissolution. Since these steps are in series, the rate-limiting step(s) will determine the performance of the overall phase transformation. There are seven scenarios to cover all of the possibilities: three scenarios when any of the three kinetic processes are limited, three scenarios when two of the three processes are limited, and one scenario when three processes are all important. Da_D and Da_G are the two independent parameters, which determine the relative importance of the reaction, dissolution, and diffusion processes. We keep K as a constant and vary Da_D and Da_G to obtain the seven scenarios mentioned above.

6.5.1.1. Distinct characteristics when any of the three processes dominates

Figure 6-3 shows the modeling results obtained when any of the three processes is limited. We use a system with Da_D=100 and Da_G=100 to represent the situation when the diffusion process dominates ($D << k_G, k_D$); a system with Da_D=0.01 and Da_G=1 to represent the situation when the dissolution process dominates ($k_D << k_G, D$); and a system with Da_D=1 and Da_G=0.01 to represent the situation when the reaction process dominates ($k_G << D, k_D$).

The initial geometry of membrane morphology is set to mimic the experimental observations in the 40 mol% SM systems at the beginning of the solvent-mediated phase transformation. The small white region in the middle is an SMase-feature, and the other white regions are SM-enriched domains, which dissolve with time. The color shows the scaled SM concentration as shown in the color bar on the right side of the pictures. A color towards red indicates a higher concentration and a color towards blue indicates a lower concentration.

The results show that the morphology evolution has distinct characteristics when different processes are dominant, as summarized in Table 6.3. When the diffusion is limited ($D << k_G, k_D$), there is a sharp dissolution ring and the SM concentration spans the whole scaled range from the reaction site to the dissolution site. When the dissolution is limited ($k_D << D, k_G$), the domains dissolve uniformly while the SM concentration in the DOPC-enriched phase is relatively low. When the reaction is limited ($k_G << D, k_D$), the domains dissolve relatively uniformly while the SM concentration is relatively high. In addition, the overall dissolution time in the reaction-limited system is longer than in the dissolution-limited system. This occurs because the interface of SM-enriched domains where dissolution can occur is much larger than the SMase-feature interface where the reaction can occur in our model, and the rate constants we use are represented as per unit interface.

The numerical results match the qualitative analyses in the pseudo-steady-state model in chapter 5. In a diffusion-limited system, the concentration gradient in the DOPC-enriched phase is high to increase the diffusion driving force so that the three processes can balance. In a reaction-

limited system with small reaction rate constant, the concentration is high to enhance the reaction process. In a dissolution-limited system, the concentration tends to become low to increase the driving force for the dissolution process.

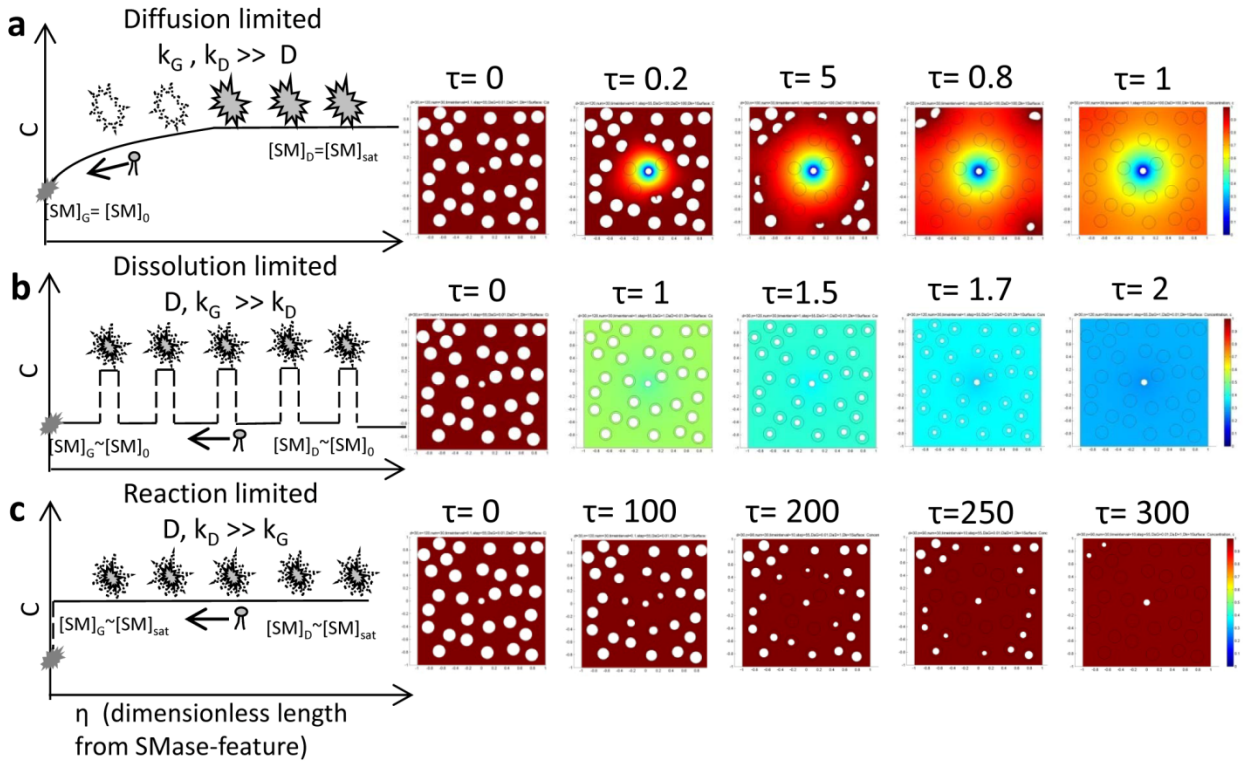

Figure 6-3. Modeling results with varying Da_D and Da_G, and fixed K from the non-dimensional model for studying the overall spatial pattern change. (a) shows a system with Da_D=100 and Da_G=100; (b) shows a system with Da_D=0.01 and Da_G=1; (c) shows a system with Da_D=1 and Da_G=0.01. All of the systems have K=1. The cartoons on the left illustrate the results we obtained from the pseudo-steady state model developed in chapter 5, which are consistent with the numerically solved modeling results obtained by the way introduced in this chapter.

Table 6-3. The parameter settings and distinct characteristics when the system is diffusion-limited, dissolution-limited, or reaction-limited.

Limited Process	Parameter Setting	Dissolution type	Averaged Concentration	Concentration Gradient
Diffusion($D << k_G , k_D$)	Da_G=100 Da_D=100	Sharp	Medium	Large
Dissolution($k_D << D, k_G$)	Da_G=1 Da_D=0.01	Uniform	Low	Small
Reaction($k_G << D, k_D$)	Da_G=0.01 Da_D=1	Gradual	High	Small

6.5.1.2. Dissolution behavior of each SM-enriched domain when any of the three processes dominates

We have discussed the overall spatial pattern change in section 6.5.1.1, and in this section, we examine the shape change of each SM-enriched domain at different locations relative to an SMase-feature. We simplify the system by constructing an initial morphology with ordered SM-enriched domains as shown in the left side of Figure 6-4. The domains are arranged in an ordered structure so that each domain with a diameter, d_i, is apart from the next one by two times d_i from center to center, where the SMase-feature is located, and each domain has a similar neighbor structure. The diameter of a domain (d_i) is set to be one-tenth of the overall system's size (R). The morphology is symmetric and the figures on the left of Figure 6-4 show just a quarter of the morphology and we measure the motion of the alphabetically named portions of the interfaces. The initial distances of these portions of the interfaces from the SMase-feature (r) are set to be d_i, $2d_i$, $3d_i$, $4d_i$, $5d_i$, and $6d_i$.

The plots on the right of Figure 6-4 show the displacement versus time of the labeled portions in their local normal directions towards SM-enriched domains. In a diffusion-limited system (Figure 6-4(a)), the shape change of each domain is significantly isotropic. The displacement velocity significantly varies with locations of the portions of the interfaces. The portions do not start to dissolve significantly before the previous portion fully dissolved. For example, the displacement of portion C starts to increase significantly not until portion A fully dissolved.

In a dissolution-limited system (Figure 6-4(b)), the shape change of each domain is isotropic, and the displacement velocities are similar in all of the portions of the interfaces.

In a reaction-limited system (Figure 6-4(c)), the displacement velocity also varies with locations. However, unlike the sequencing characteristic we observed in a diffusion-limited system, the velocities of different portions have a similar trend. In addition, although the shape change of each domain is anisotropic in domains close to SMase-feature, the shape change of those distant domains is relatively isotropic.

The shape change of each domain and the displacement velocity in the diffusion-limited and the dissolution-limited system are expected and consistent with the results from the pseudo-steady state model shown in chapter 5. The pseudo-steady state model is qualitatively consistent with the overall pattern change and average concentration of a reaction-limited system; however, it was not able to capture the difference of the portions with difference distances from an SMase-

feature. This is because we did not consider the geometry factor in the pseudo-steady model, which can be incorporated into our current numerically-solved model.

The different displacement velocity of different portions of the interfaces in a reaction-limited system comes from the SM concentration gradient in the fluid DOPC-enriched phase. Although we have shown that the concentration profile is relatively uniform in Figure 6-3(c), the concentration gradient still exist so that the diffusion occurs to transfer SM molecules towards the SMase-feature located in the center of a corral. The concentration decreases towards the SMase-feature. The displacement velocity of a portion of a SM-enriched domain boundary depends on its local concentration. Therefore, the portions closer to the SMase-feature dissolve more quickly since they expose to a lower concentration, which is equivalent to larger driving force for dissolution. In addition, we observe that those portions closer to the SMase-feature start to dissolve earlier than distant ones because the concentration profile gradually propagated away from an SMase-feature after the reaction initiates the overall process. The closer the portions, the earlier their surrounding concentrations are affected. Furthermore, we observe the distant domains dissolve more isotropically than closer domains. The isotropic dissolution of a domain indicates that all of the portions on the boundary of the domain have a similar displacement velocity. According to the conservation equation in r-θ coordinate, the concentration profile in the r-direction away from the SMase-feature is in log form. The concentration gradient dramatically decreases with r. That is, the concentrations of two fixed-distance portions are more similar at larger r than at smaller r. Therefore, the portions of a distant domain have more a similar concentration and thereby a more similar displacement velocity than the portions of a domain closer to the SMase-feature, which is shown on the right plot of Figure 6-4(c).

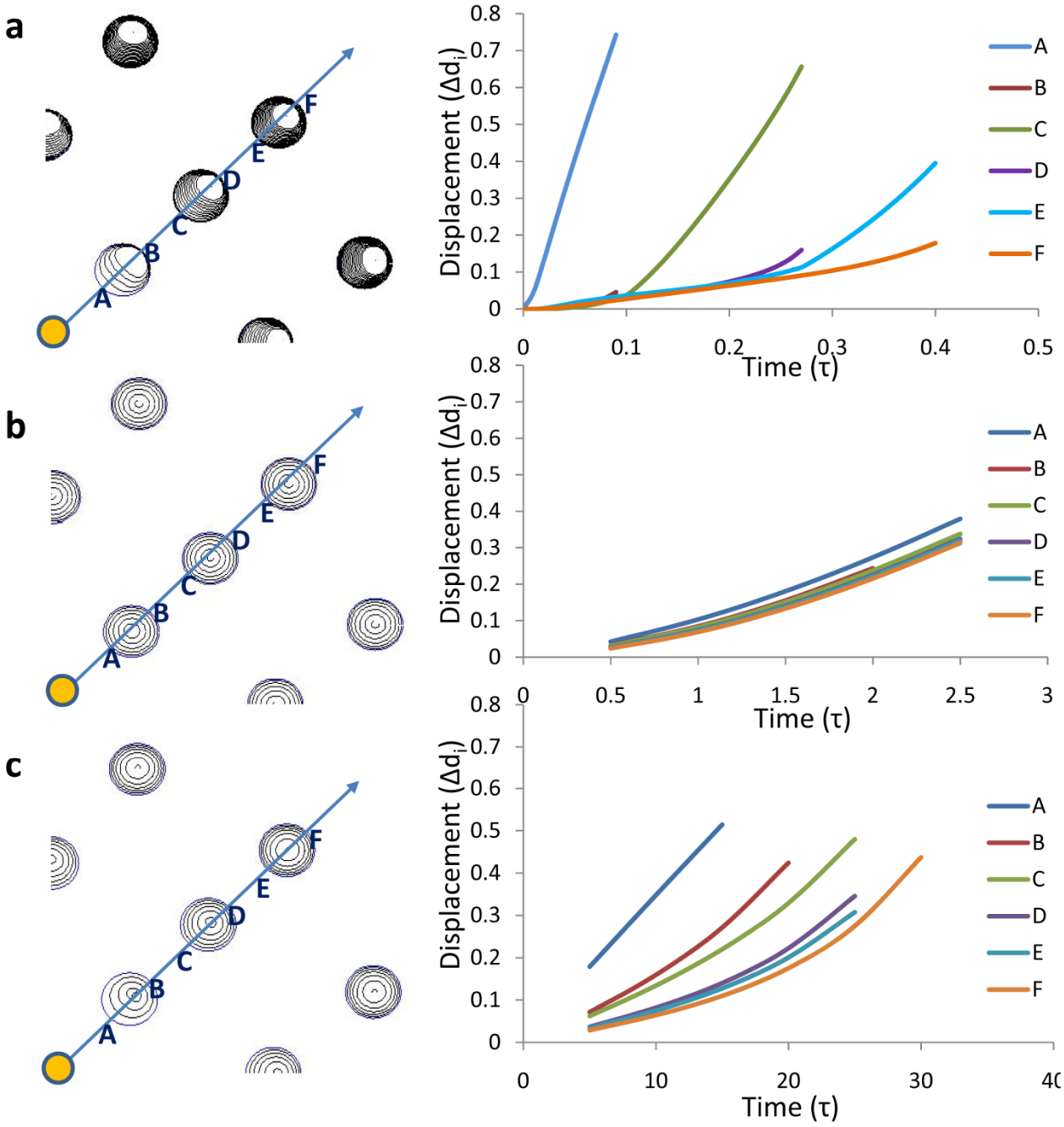

Figure 6-4. Dissolution pattern of each SM-enriched domain when any one of three kinetic processes is limited. The round yellow object is an SMase-feature while the other objects are SM-enriched domains at different locations relative to the SMase-feature. The dark lines indicate the location of the SM-enriched domain interface after each time step. The distance of the

adjacent two dark lines indicates the motion of the SM-enriched domain interface during the interval of a time step. The alphabets label the portions of interfaces where we measure the motion rate. The initial distances of A, B, C, D, E, and F from the SMase-feature are set to be d_i, $2d_i$, $3d_i$, $4d_i$, $5d_i$, and $6d_i$. The motion rates at theses portions of the interfaces are plotted on the right. (a) shows a system with Da_D=100 and Da_G=100, and the interval of each time step is 0.05 τ; (b) shows a system with Da_D=0.01 and Da_G=1, and the interval of each time step is 0.5 τ; (c) shows a system with Da_D=1 and Da_G=0.01, and the interval of each time step is 5 τ. All of the systems have K=1.

6.5.1.3. Combined characteristics when more than one of the processes dominate

When more than one of the kinetic processes dominate, the modeling results show that the system has combined characteristics of the distinct characteristics of each of the limited scenarios (Figure 6-5). For example, when three processes all dominate, we observe that the system has a gradual dissolution pattern instead of a sharp dissolution ring, and the dissolution time and the concentration profile are also between the characteristics of the three extreme cases shown in section 6.5.1.1 (Figures 6-5(a)(e)). Overall, there are four scenarios: one case when three processes all dominate and three cases when any two of the three processes dominate. Table 6-4 shows the parameter settings and the characteristics of the four scenarios.

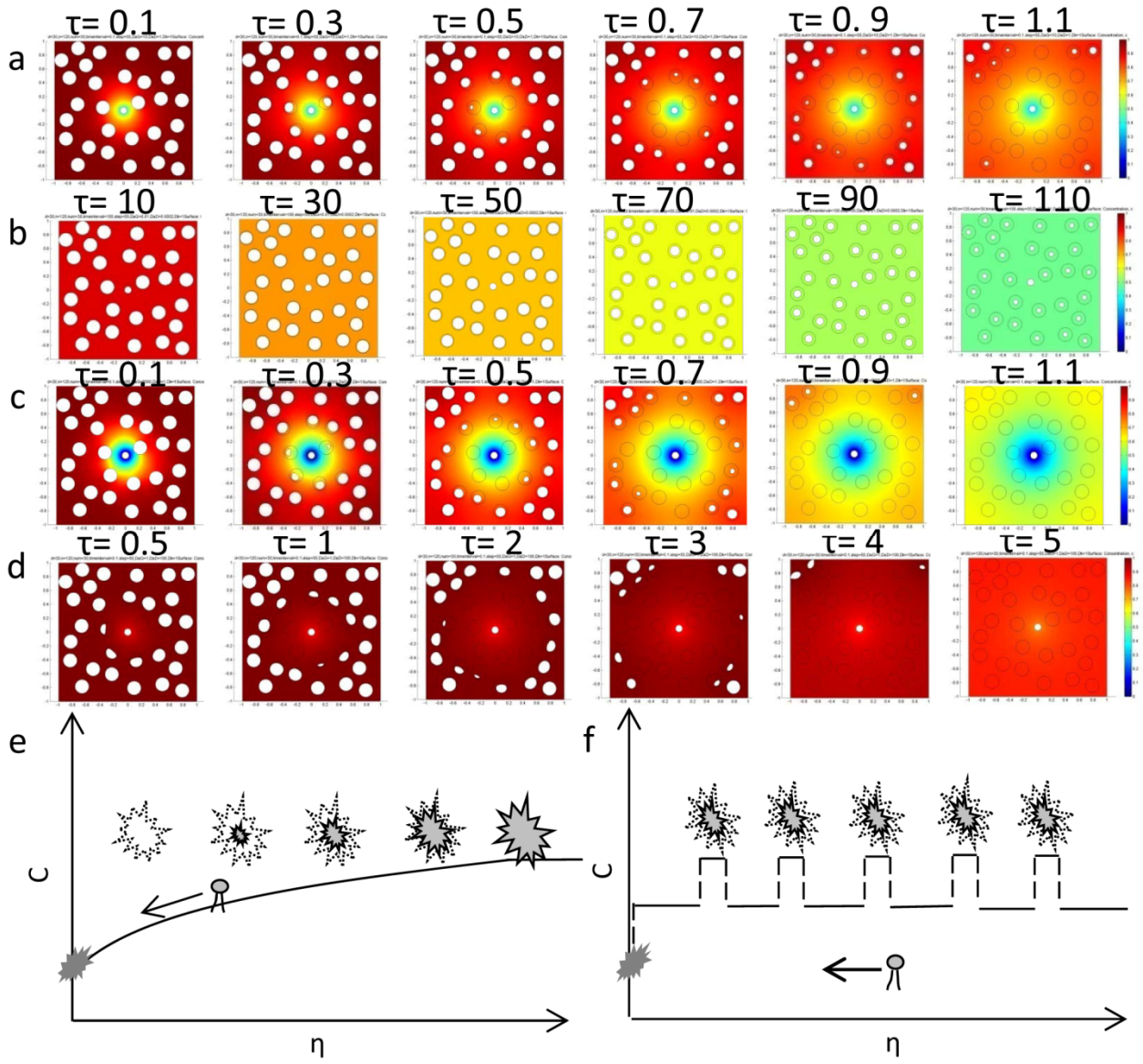

Figure 6-5. Modeling results with varying Da_D and Da_G, and fixed K (K=1) from the non-dimensional model for studying the overall spatial pattern change. (a) shows a system with Da_D=1 and Da_G=1 (dissolution, reaction, and diffusion processes all dominate); (b) shows a system with Da_D=0.01 and Da_G=0.01 (dissolution and reaction processes dominate); (c) shows a system with Da_D=1 and Da_G=100 (dissolution and diffusion processes dominate); (d) shows a system with Da_D=100 and Da_G=1 (reaction and diffusion processes dominate). (e) is the cartoon showing the gradual dissolution of (a) along the radial direction away from the central SMase-

feature. (f) is the cartoon showing the uniform dissolution of (f). The concentration is in the medium range which is the combination of the high concentration characteristic of a reaction-limited system and the low concentration characteristic of a dissolution-limited system.

Table 6-4. The parameter settings and distinct characteristics when more than one of the kinetic processes are limited.

Limited Process	Parameter Setting	Dissolution type	Averaged Concentration	Concentration Gradient
Diffusion, Reaction, Dissolution ($D \sim k_G \sim k_D$)	$Da_G=1$ $Da_D=1$	Gradual	Medium	Medium
Reaction, Dissolution ($k_G, k_D \ll D$)	$Da_G=0.01$ $Da_D=0.01$	Uniform	Medium	Small
Reaction, Diffusion ($k_G, D \ll k_D$)	$Da_G=1$ $Da_D=100$	Gradual	High	Large
Dissolution, Diffusion ($k_D, D \ll k_G$)	$Da_G=100$ $Da_D=1$	Gradual	Low	Large

6.5.2. Varying K: the ratio of SM content in the DOPC-enriched phase to the content in SM-enriched domains

K represents the SM which can be stored in DOPC-enriched phase ($[SM]_{sat}$) compared to the SM stored in the SM-enriched domains ($[SM]_{solid}$). If the SM amount stored in SM-enriched domains is the same as the one in the DOPC-enriched phase, the concentration is uniform in the initial condition (and $K \rightarrow \infty$). If the SM releasing from the SM-enriched domain regions is not constrained in this case (i.e., the dissolution is not limited), the system should perform similarly to the system with only the DOPC-enriched phase with saturating SM. On the other hand, if there is a high density of SM stored in the domains, more SM needs to be processed and delivered and therefore more time is needed for the overall process to be completed.

Figures 6-6, 6-7, and 6-8 show the modeling results with varying K in to shown in diffusion-limited, dissolution-limited, and reaction-limited systems. The results show that K does not influence the distinct characteristics introduced in section 6.5.1.1. The major influence from K is that the overall dissolution time is delayed with decreased K, which is equivalent to increased stored SM density.

While K=10, which means $[SM]_{solid}=1.1[SM]_{sat}$, we observe that the overall concentration profile change is very similar to when there are no SM-enriched domains in both the diffusion-limited system and the reaction-limited system (the first and second rows in Figures 6-6 and 6-7). The comparison in the dissolution-limited system cannot be made since dissolution rate cannot be specified in the system without any domains. However, we can clearly observe that the shrinking

rate of each domain is decreased with the decreased K (or the increased SM density in the domains) in the dissolution-limited system (Figure 6-8).

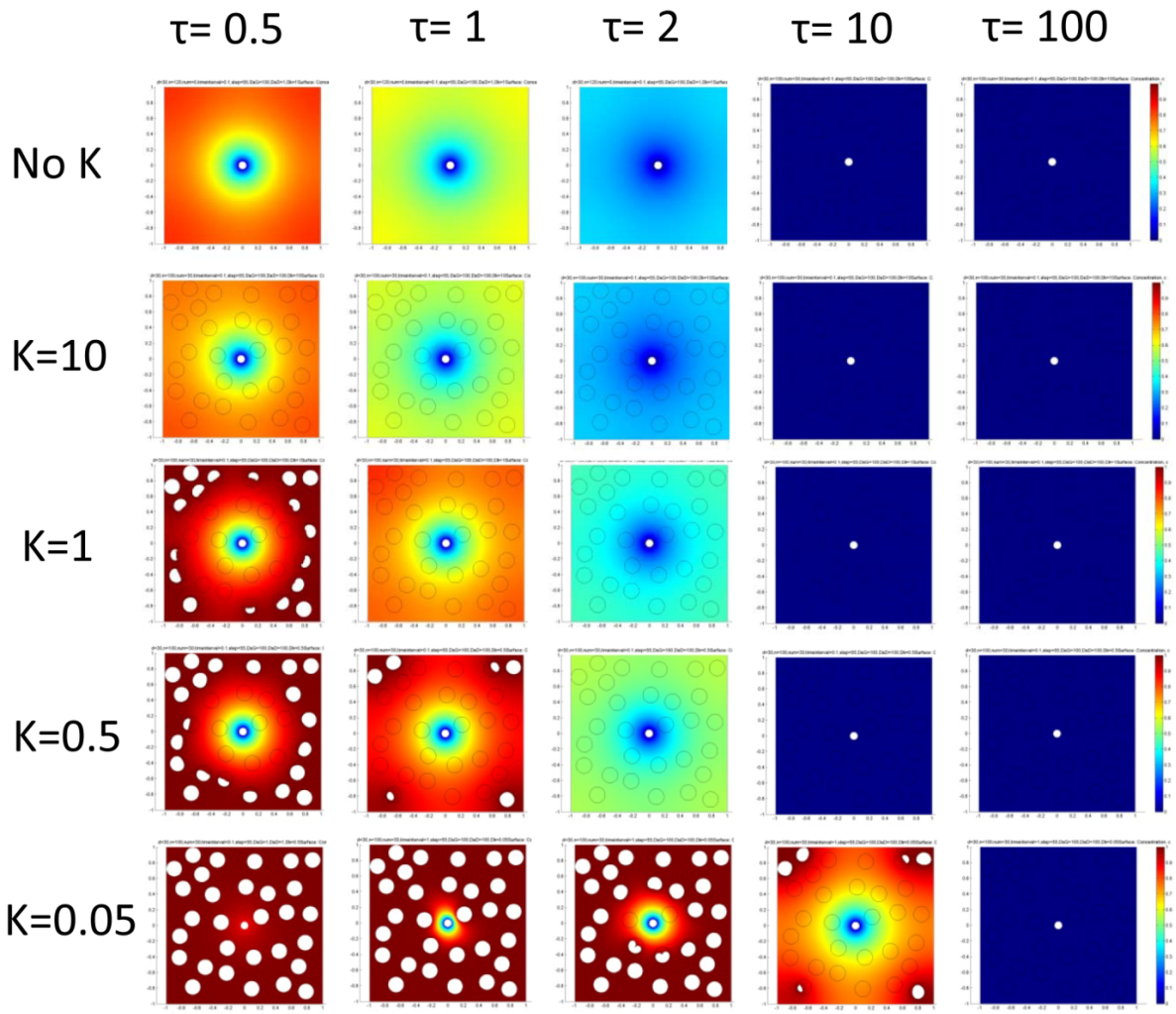

Figure 6-6. Modeling results with varying K in the diffusion-limited system (Da_D=100 and Da_G=100) from the non-dimensional model for studying the overall spatial pattern change. The first row is a system in the absence of any SM-enriched domains.

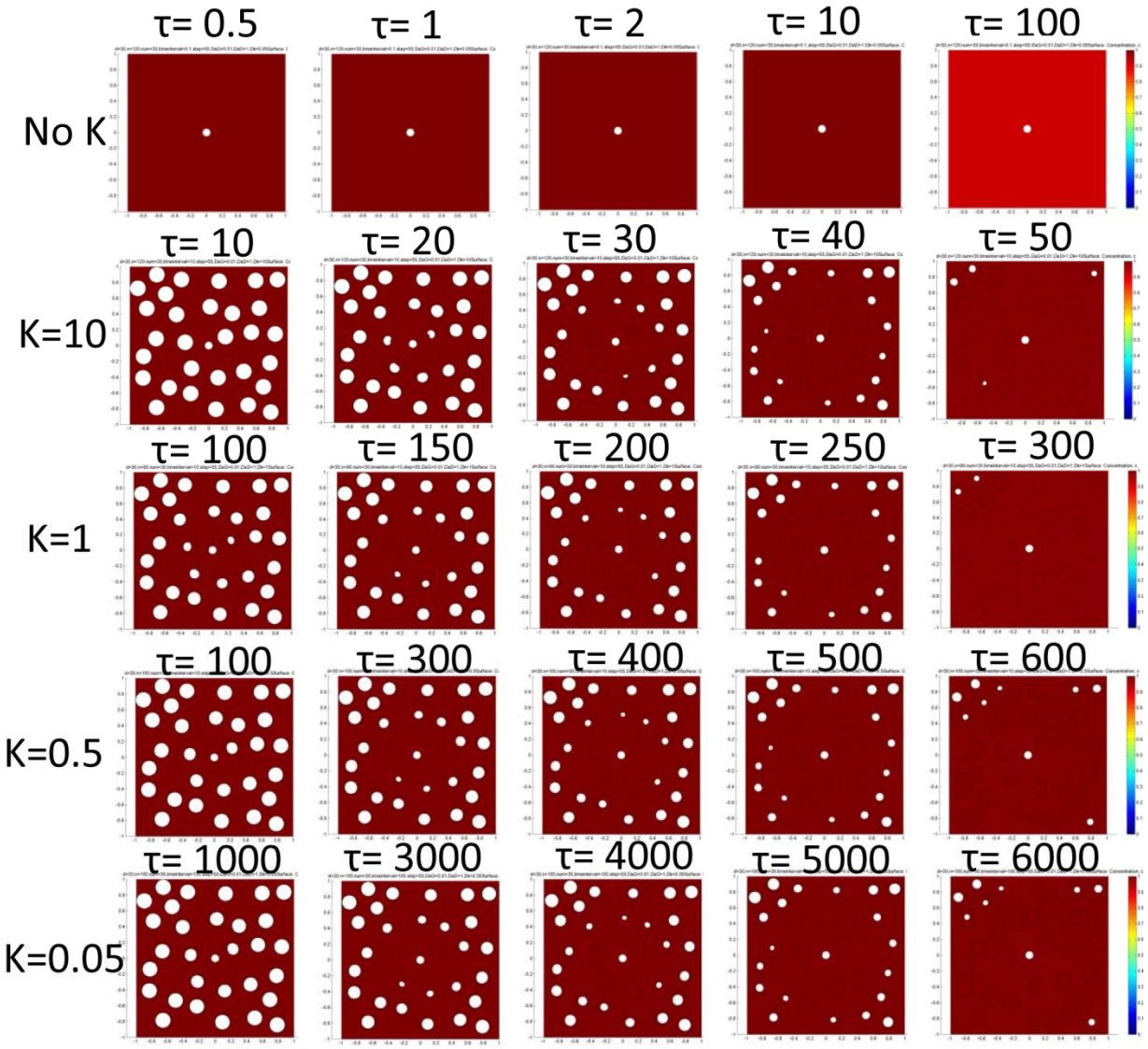

Figure 6-7. Modeling results with varying K in the reaction-limited system (Da_D=1 and Da_G=0.01) from the non-dimensional model for studying the overall spatial pattern change. The first row is a system in the absence of any SM-enriched domains.

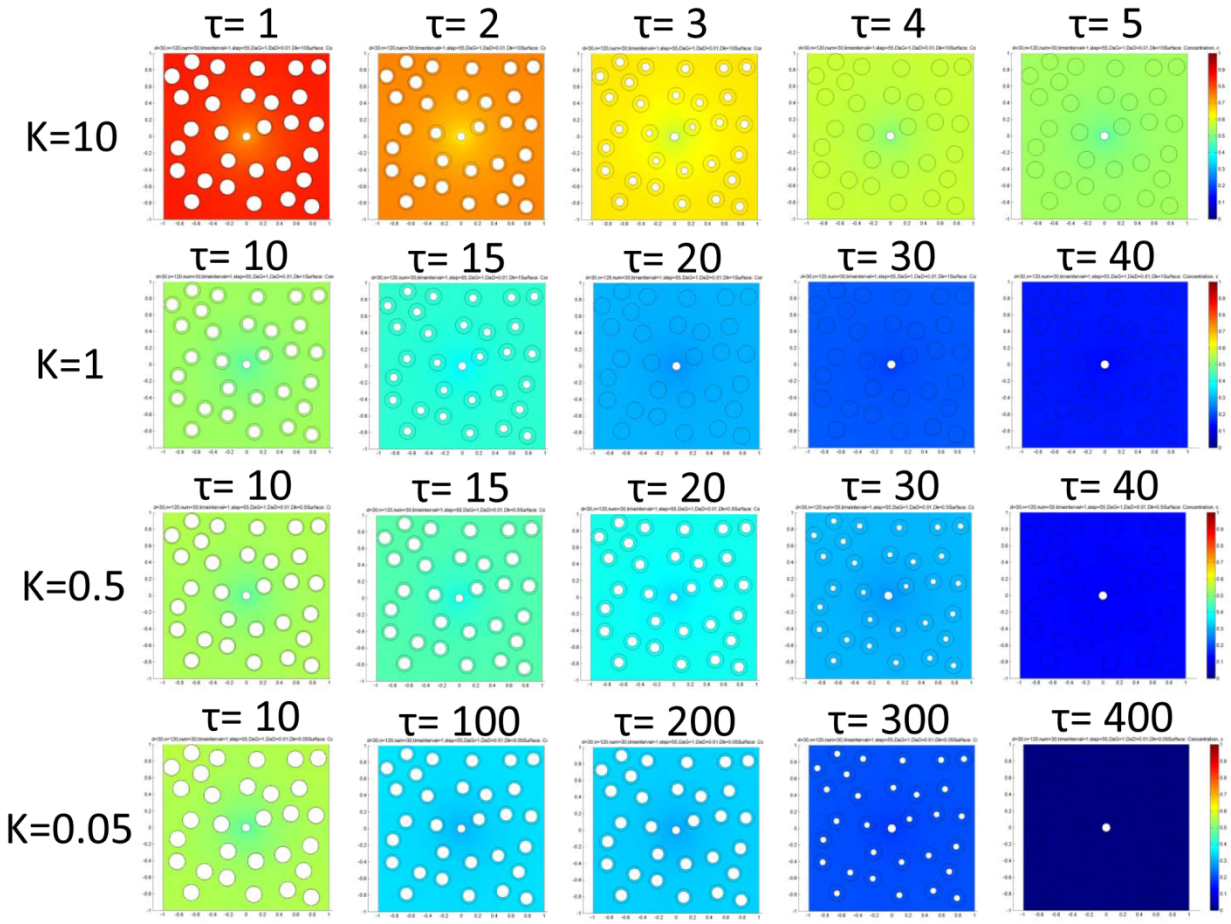

Figure 6-8. Modeling results with varying K in the reaction-limited system (Da_D=0.01 and Da_G=1) from the non-dimensional model for studying the overall spatial pattern change.

6.5.3. Varying the initial geometry: number density of SM-enriched domains

Here, we examine the effects from the initial geometry. Under the same initial geometry, we have shown all of the possible scenarios based on the three parameters in the model in sections 6.5.1 and 6.5.2. The initial geometry in those sections was set to mimic the membrane morphology we experimentally observed in membranes with 40 mol% of SM.

From our experimental observations, when we decreased the pre-existing SM content in the membrane systems containing the same type of SM, we found that the number of domains decreased while the average domain size is still similar. Therefore, in this section, we are particularly interested in how the number of SM-enriched domains in a system can influence the overall dissolution time, since the systems with different numbers of domains in a corral have been observed to have different dissolution times. This information can help us to further understand the overall dissolution behavior, which can be governed by not only the three physical parameters but also by a geometry factor, the number of domains.

The modeling results in Figure 6-9 come from the systems with varying numbers of SM-enriched domains. They show that the overall dissolution time is approximately proportional to the number density of the domains, while these systems' three model parameters are kept the same. The modeling results indicate that even if the physical properties of membrane systems are the same, the numbers of SM-enriched domains can contribute to the delay of the overall dissolution time.

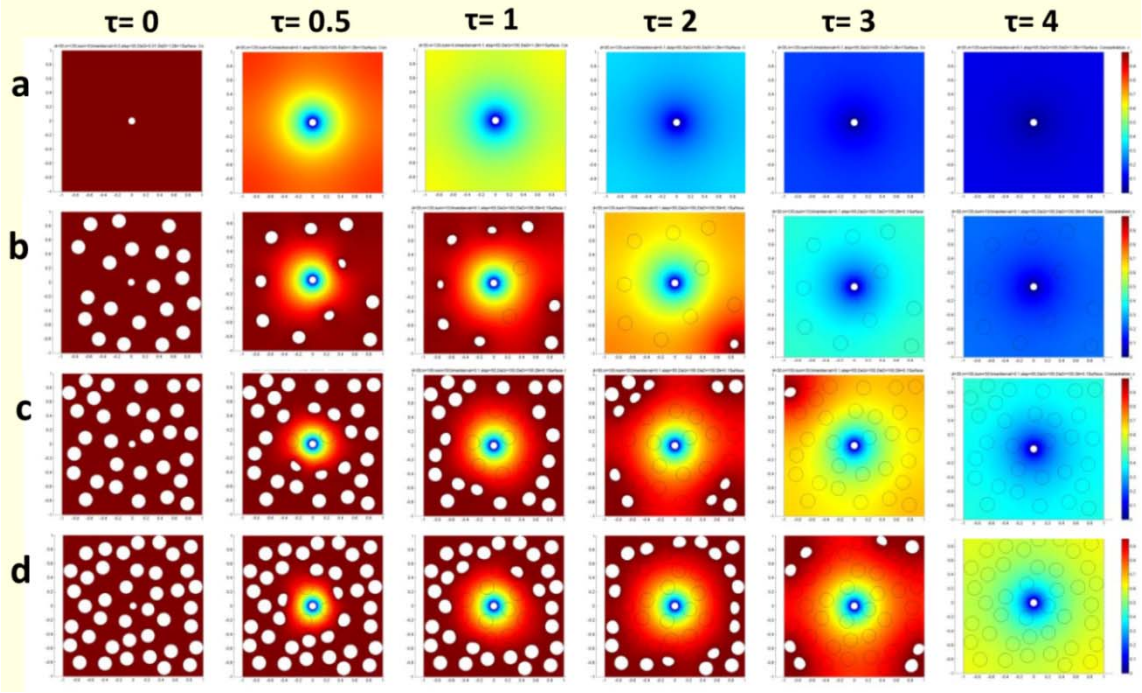

Figure 6-9. Modeling results with varying density of domain number in the diffusion-limited system (Da_D=1 and Da_G=1) from the non-dimensional model for studying the overall spatial pattern change. The number densities of the SM-enriched domains in the systems are (a) 0, (b) 20, (c) 30, and (d) 40 per corral. The diameter of each domain is one-tenth of the corral length.

6.5.4. Comparisons with the experimental results

From our experiments, we have observed sharp dissolution rings in the membrane systems with 40 mol% of SM (40/40/20 and 60/40/0 molar ratio of DOPC/brain SM/Chol) (as shown in chapter 5). If the developed model truthfully describes the system, the modeling result indicates that the membrane systems with 40 mol% of SM are limited by diffusion. That is, the associated reaction constant and dissolution constant are much larger than the diffusivity divided by the corral length. To obtain the corresponding τ of the morphology evolution from our experimental

results, we need to scale the time of the morphology evolution with the diffusion characteristic time (R^2/D). R is the length of a corral, 50 μm. We measured the lateral diffusivity (D) of lipid molecules in the SLBs by fluorescence recovery after photobleaching (FRAP) and found that it is 1.91 μm^2/sec for the membrane with 40/40/20 molar ratio of DOPC/SM/Chol. The morphology evolution with the corresponding τ is shown in Figures 6-10 (a)(b). From our experiments, we have observed that the duration to dissolve all of the SM-enriched domains in the membranes with 40 mol% SM with and without Chol (Table 5-1) is about 50 min, which corresponds to about τ=10.

In the model we develop, Fick's Law is used to describe the diffusion kinetic process; the first-order reaction is used to describe the effective SM consumption at the SMase-feature interface; the first-order dissolution is used to describe the SM releasing from the SM-enriched domain interface. There are only three parameters (Da_G, Da_D, and K) to describe a fixed-initial-morphology system. Varying these three parameters can describe all of the situations that can occur in this model. We have shown in section 6.5.1.1 and 6.5.1.3 that varying Da_G and Da_D produces seven scenarios that cover all of the possibilities. The sharp dissolution ring can only occur in a diffusion-limited system (Da_G >>1 and Da_D >>1). The decrease of either Da_G or Da_D causes a more gradual dissolution. In addition, we have also shown that the distinct dissolution pattern change is not influenced by K (section 6.5.2). Therefore, the sharp dissolution ring in the model occurs if and only if the system is diffusion-limited.

In our model, when a system is diffusion-limited, the pattern change is not influenced much by the exact values of Da_D and Da_G as long as they are both much larger than one. Therefore, we

can use the use the system with Da_D=100 and Da_G=100 to generally represent diffusion-limited systems. K becomes the only parameter left that can influence the overall dissolution time in the model when the model has a fixed initial geometry mimicking the experimental observations. Decreased K results in longer overall dissolution time, since more SM is stored in the SM-enriched domains and requires more time to be processed and delivered, as we have shown in section 6.5.1.2.

If we compare the modeling results with our experimental observations, we find that the overall dissolution interval in the model of a diffusion-limited system with K~0.05 is about τ=10 which is consistent with our observations in the 40 mol% SM experiments. If we examine and compare the detailed morphology evolution, Figure 6-10 shows that the experimental results match well to the modeling results. The consistent results suggest the validity of our model. In addition, K~0.05 suggests that the SM content in the SM-enriched domains is about twenty times of the content in the DOPC-enriched phase. This information is valuable since the composition information in lipid membrane is usually difficult to measure.

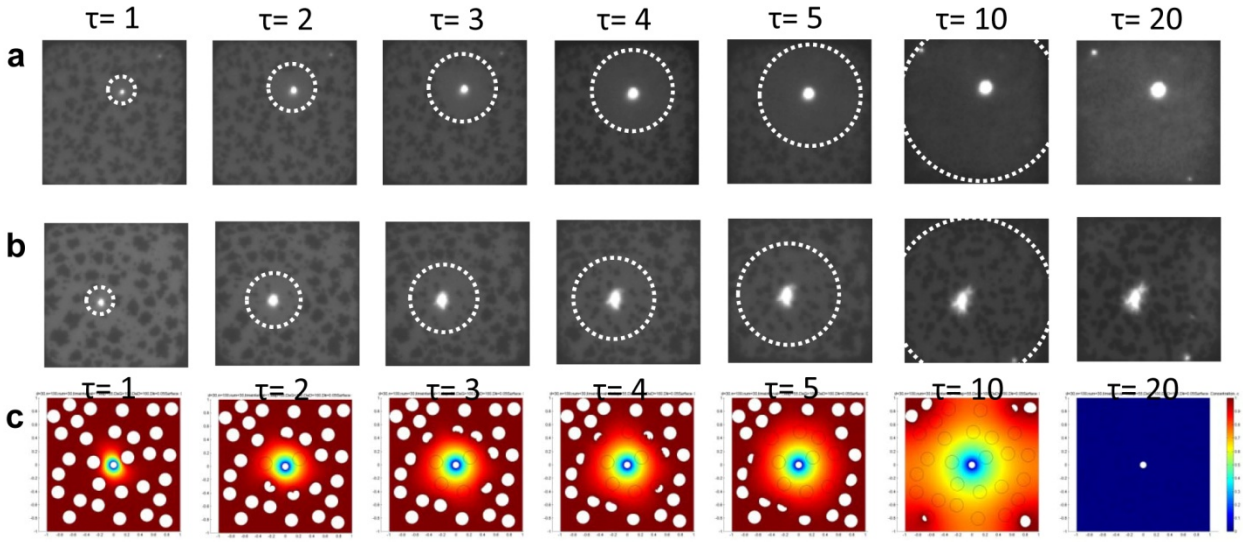

Figure 6-10. Comparison of the dissolution ring growth from modeling result and from experimental results. (a) is the experimental result from the 40/40/20 molar ratio of DOPC/brain SM/Chol membrane treated with 0.005 unit/ml SMase. (b) is the experimental result from the 60/40/0 molar ratio of DOPC/brain SM/Chol membrane treated with 0.005 unit/ml SMase. (c) is the modeling result of the system with K=0.05 in the diffusion-limited system (Da_D=100 and Da_G=100) from the non-dimensional model for studying the overall spatial pattern change.

Chapter 7. Conclusions and Outlook

7.1. Conclusions

Sphingomyelinase (SMase) has been suggested to be involved in a variety of cellular processes by reorganizing the cell membrane heterogeneity. However, the regulation of membrane heterogeneity by SMase was still unclear since the enzymatic reaction has strong interplay with the physical states of lipid membranes. We developed corralled membrane arrays in a microfluidic device to achieve effective control of microenvironment conditions during the enzymatic reaction, which is needed for studying the system with high spatio-temporal resolution information (domain dynamics) embedded in a small amount of materials (lipid bilayers). We reported that SMase can induce a reaction-induced and a solvent-mediated phase transformation, causing switches of three stationary membrane morphologies and multiple-time-domain ceramide generation in model raft membranes. We further demonstrated that lipid membrane composition and SMase concentration can be used to tune the two phase transformation processes and therefore the intervals and spatial patterns of the SMase-induced multi-stage morphology evolution. Furthermore, we modeled the spatio-temporal morphology change during the solvent-mediated phase transformation. The modeling results were shown to be consistent with our experimental results and can provide insights into the system parameters that are difficult to measure.

The overall results showed that SMase can be actively involved in the lipid membrane phase changes. The SMase-induced multi-stage morphology evolution is not only due to compositional changes caused by SMase, but also due to the selective binding of SMase, and the SMase's special phase behavior. The timing and sequence of the morphology switches and ceramide generation by SMase in our model systems were observed to be similar to those of the cell morphology and cell ceramide accumulation observed in physiological studies. Although the cell morphology change and ceramide accumulation in cells could originate from many different sources in complex cell systems, the consistent timing and sequence with that observed in our model systems (with only basic components of cell membranes and SMase) suggests that the lipid membrane phase behavior induced by SMase may be a contributing factor to the multiple-time-domain phenomena in cells. The spatio-temporally tunable SMase-induced multi-stage morphology evolution based on the two phase transformations could also provide a spatio-temporal control mechanism of phase dynamics in the cell membrane.

7.1.1. Development of corralled model membrane arrays in a microfluidic device

We developed a microfluidic platform with model membrane arrays to achieve easy tracking of the observed membrane systems, effective control of reaction conditions, and high-throughput screening of experimental conditions. Corralled supported lipid bilayers allowed the mass balance of lipid molecules during the surface reaction, greatly facilitating the interpretation of the complex phase behaviors induced by SMase. In addition, the model membrane arrays with numerous separated systems in parallel were used to capture the wide distribution of the induction time of domain nucleation, allowing us to compare the effects caused by different

factors. The flow control by a microfluidic device addressed the difficulty of distributing SMase solutions uniformly to the membrane systems, allowing us to obtain robust results from area to area and from sample to sample, which is required for correlating our characterization results to the morphology evolution results.

7.1.2. SMase induces two phase transformations in model raft membranes

The reaction-induced phase transformation, triggered by the addition of SMase, transformed a pre-existing raft morphology to a pause morphology with coexisting ceramide-enriched (Cer-enriched) and sphingomyelin-enriched (SM-enriched) domains. The pause situation was resolved after the solvent-mediated phase transformation occurred to further transform all of the SM-enriched domains into Cer-enriched domains. Labeled SMase experiments suggested that the stable morphology in the middle was due to the physical trapping of SM in the SM-enriched domains that are found to be relatively inaccessible to SMase. The characterization results from confocal fluorescence imaging showed that the trigger of the solvent-mediated phase transformation is the formation of a 3-D feature rich in SMase, sphingomyelin, and ceramide. This 3-D feature was hypothesized as a slowly nucleating phase of SMase with the lipids, where SMase processes sphingomyelin more efficiently. The disparate time-scales of the formation of these SMase-features and the SM-enriched domains allowed for the development of a significant duration of the middle pause morphology between the two transformations.

7.1.3. Tunable intervals and spatial pattern of multi-stage morphology evolution based on the two phase transformations

We demonstrated that lipid membrane composition and SMase concentration can be used to tune the intervals and spatial patterns of the SMase-induced multi-stage morphology evolution. At a physiologically relevant concentration of SMase, we found that membrane composition can tune the formation of SM-enriched domains and the nucleation of SMase-features at different extents of time scale and thus significantly tune the stable duration of the middle pause morphology. In addition, the induction time of SMase-feature nucleation, the trigger of the solvent-mediated phase transformation, decreased with the increased supersaturating level of SMase and increased pre-existing ceramide amount. Sphingomyelin was also required for the formation of the SMase-feature. During the solvent-mediated phase transformation, the interval and the spatial pattern change were suggested to be primarily influenced by the interplay of the reaction of SM at an SMase-feature, the diffusion of SM from SM-enriched domains to an SMase-feature, and the dissolution of SM-enriched domains. The pseudo-steady state model indicated that the anisotropic dissolution occurs when a system is diffusion-limited, while the isotropic dissolution is characteristic of a reaction-limited or dissolution-limited system.

7.1.4. Reshuffling of lipid molecules during the SMase-induced reaction-induced phase transformation

The overall multi-stage morphology evolution in giant unilamellar vesicles (GUVs) with mobile domains was comparable to what we observed in supported lipid bilayers (SLBs) with fixed domains. Similar features occurred in the same order and the primary difference was the mobility

of domains. The early-stage morphology evolutions in GUVs and SLBs consistently showed the formation of SM-Cer-enriched domains and the disintegration of the pre-existing SM-Chol rafts. The results excluded the possibility of the direct coalescence of the pre-existing rafts to form later large platforms containing SM and Cer. Instead, there was a reshuffling of lipid molecules during the transformation from the pre-existing morphology with SM-Chol rafts to the next morphology with SM-Cer-enriched domains. According to the raft hypothesis, the reshuffling of lipid molecules implies that the membrane proteins can easily reshuffle. This reshuffling phenomenon can explain why the membrane proteins found in the conventional cholesterol rafts are absent in the later ceramide-containing large platforms, which could not be explained by the previous coalescence conjecture.

7.1.5. Modeling the spatio-temporal morphology change during the solvent-mediated phase transformation

We built a model to explore the spatio-temporal morphology change during the solvent-mediated phase transformation. Three major kinetic processes were described in the model: the consumption of SM by the enzymatic reaction at an SMase-feature, the diffusion of SM from SM-enriched domains to an SMase-feature, and the release of SM due to the dissolution of SM-enriched domains. We combined MATLAB coding with Comsol to solve the model, with complex geometry and moving boundary. The non-dimensionality of the model allows the system to be characterized by only three non-dimensional parameters. We show all of the possible scenarios of spatial pattern change during the phase transformation. The modeling results were shown to be consistent with our experimental results. Since the phenomena in cells

are more complex and can be contributed to by many factors, such as the force from the cytoskeleton, the present modeling work, which is based on the contribution from the lipid membrane phase behavior can provide a framework for the future incorporation of other identified factors to determine the cell membrane responses.

7.2. Outlook

7.2.1. Monitoring the conversion rate of SM from bulk solutions and the morphology change in parallel

SMase converts SM to hydrophobic Cer and hydrophilic phosphorylcholine. The conventional method to measure the SMase's activity is to measure the increasing phosphorylcholine content in bulk solutions after SMase is added to the solutions containing small lipid vesicles. The commercial assay kit can convert phosphorylcholine to detectable fluorescent resorufin, as shown in Figure 7-1.

We have interpreted the ceramide generation in our model system by observing the extent of labeled anti-ceramide in the system, as shown in chapter 3. Our characterization results have shown that the ceramide generation can be divided into multiple time-domains and ceramide is generated significantly only after an SMase-feature nucleates. In chapter 5, we have further shown that the SMase-feature nucleation has a wide distribution of induction time. We can expect that the overall conversion rate of SM measured from bulk solutions would be the summation of the conversion rates from each membrane system, which has variation in the SMase-feature's nucleation time. One example is shown in Figure 7-2, in which the green color

indicates where ceramide locates, and only those membrane systems that already had SMase-features (the orange-yellow dots) have significant amounts of ceramide.

We would like to observe the morphology evolution and measure the overall conversion rate by the conventional method at the same time. Since we perform our experiments in a microchannel, we can flow the reagents of the assay kit and measure the fluorescence intensity of resorufin directly in the channel. Since resorufin emits fluorescence at red wavelength, we will need to use another type of lipid probe instead of the Texas-Red® DHPE we usually used.

One of the goals is to demonstrate if the overall conversion rate of SM would be a combination of the conversion rates from each of the membrane systems among the membrane array, which has varied SMase-feature nucleation times. The results can be used to link the current studies with a detailed phase change mechanism to conventional bulk SMase activity measurements.

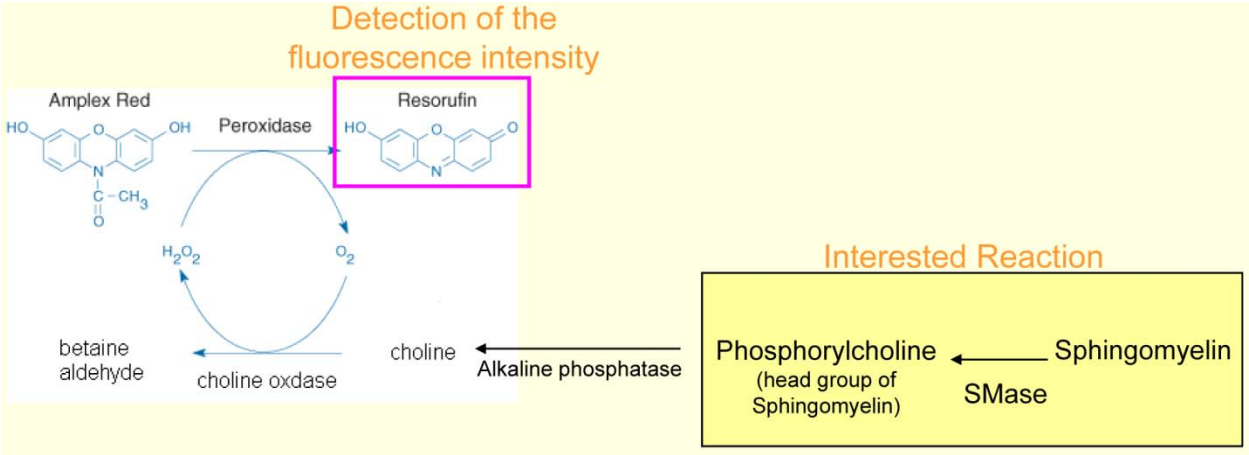

Figure 7-1. The commercial assay kit converts phosphorylcholine to detectable fluorescent resorufin in several steps.

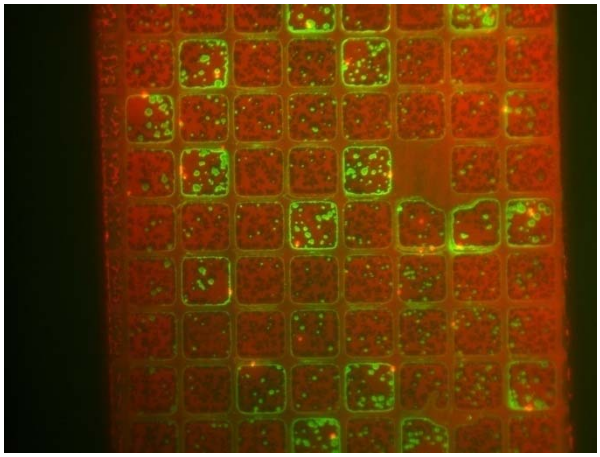

Figure 7-2. The variation of ceramide generation among the model membrane array exposed to the same conditions is displayed by an image illuminated by Alexa Fluor® 488-labeled anti-ceramide. The green color indicates where ceramide locates and only those membrane systems that already had SMase-features (the orange-yellow dots) have significant amounts of ceramide.

7.2.2. Examination of the SMase-induced phenomena in cells

It would be interesting to further examine whether the SMase-induced phase transformations can be observed clearly in cells. The reason we used model membrane systems in this study is that direct cause-effect relationships are difficult to identify in complex cell systems. By using model systems with controlled environments, we are able to study SMase-lipid membrane interactions and identify the contributions of basic components in the cell membrane. Further investigation in cells could allow us to learn if the SMase-lipid membrane interactions can significantly influence the cell morphology and play a dominant role in the cell membrane behavior.

Suitable stimuli can be provided to initiate the translocation of cell-produced SMase to the cell membrane by the protocol in previous physiological studies. Cells with the knockout gene of SMase can be used as a control. Immunostaining can be used to stain where SMase, Cer, and SM locate in the cell plasma membrane in the same way as we did for our model systems.

To examine whether the two SMase-induced phase transformations occur significantly in the cell membrane, we can first quantitatively compare the features and domains observed in cells and in our model systems. Second, we can examine whether the time of occurrence of these features can be tuned in the same way as those in our model systems. We have used membrane composition and SMase concentration in this study to tune the two phase transformations. In cells, different cell membrane compositions can be achieved by using different types of cells, and different amounts of SMase translocating to the cell plasma membranes can be achieved by using different stimuli.

With further investigation in cells, we will be able to learn whether the SMase-induced phase transformations play a dominant role in influencing the cell membrane heterogeneity. The cell signaling always needs to pass through the cell plasma membrane. More and more studies have suggested that the membrane heterogeneity influences the initiation time, signal strength and signal duration. If these phenomena are dominant in the cell membrane, they may serve as spatio-temporal control mechanisms of how the signaling enters the cell. The tunable ability of membrane heterogeneity based on the predictive mechanisms may have therapeutic applications for the SMase-related cellular processes.

REFERENCES

1. Campbell, N. *Biology*, 1999.
2. Pollard, T. D. *Cell Biology*, 2002.
3. Dietrich, C.; Bagatolli, L. A.; Volovyk, Z. N.; Thompson, N. L.; Levi, M.; Jacobson, K.; Gratton, E. *Biophysical Journal* **2001**, *80*, 1417-1428.
4. Simons, K.; Vaz, W. L. C. *Annual Review of Biophysics and Biomolecular Structure* **2004**, *33*, 269-295, 1 plate.
5. Veatch, S. L.; Keller, S. L. *Physical Review Letters* **2005**, *94*, 148101/1-148101/4.
6. Simons, K.; Ikonen, E. *Nature (London)* **1997**, *387*, 569-572.
7. Simons, K.; Toomre, D. *Nature Reviews Molecular Cell Biology* **2000**, *1*, 31-39.
8. Munro, S. *Cell (Cambridge, MA, United States)* **2003**, *115*, 377-388.
9. Mayor, S.; Rao, M. *Traffic (Oxford, United Kingdom)* **2004**, *5*, 231-240.
10. Shaw, A. S. *Nature Immunology* **2006**, *7*, 1139-1142.
11. Chatterjee, S. *Journal of biological chemistry* **1994**, *269*, 879-82.
12. Kolesnick, R. *Journal of Clinical Investigation* **2002**, *110*, 3-8.
13. Marchesini, N.; Hannun, Y. A. *Biochemistry and Cell Biology* **2004**, *82*, 27-44.
14. Tomita, M. *Journal of biochemistry* **1990**, *108*, 811-815.
15. Fujii, S.; Inoue, B.; Yamamoto, H.; Ogata, K.; Shinki, T.; Inoue, S.; Tomita, M.; Tamura, H.-O.; Tsukamoto, K.; Ikezawa, H.; Ikeda, K. *Journal of Biochemistry (Tokyo)* **1998**, *124*, 1178-1187.
16. Fujii, S.; Ogata, K.; Inoue, B.; Inoue, S.; Murakami, M.; Iwama, S.; Katsumura, S.; Tomita, M.; Tamura, H.-O.; Tsukamoto, K.; Ikezawa, H.; Ikeda, K. *Journal of Biochemistry (Tokyo)* **1999**, *126*, 90-97.
17. Hannun, Y. A. *Science (Washington, D. C.)* **1996**, *274*, 1855-1859.
18. Hannun, Y. A.; Bell, R. M. *Science (Washington, DC, United States)* **1989**, *243*, 500-7.
19. Chatterjee, S. *Chemistry and Physics of Lipids* **1999**, *102*, 79-96.
20. Kolesnick, R.; Hannun, Y. A. *Trends in Biochemical Sciences* **1999**, *24*, 224-225.
21. Kolesnick, R. N.; Kronke, M. *Annual Review of Physiology* **1998**, *60*, 643-665.
22. Levade, T.; Jaffrezou, J.-P. *Biochimica et Biophysica Acta, Molecular and Cell Biology of Lipids* **1999**, *1438*, 1-17.
23. Posse de Chaves, E. I. *Biochimica et Biophysica Acta, Biomembranes* **2006**, *1758*, 1995-2015.
24. Hengartner, M. O. *Nature (London)* **2000**, *407*, 770-776.
25. Boucher, L.-M.; Wiegmann, K.; Fuetterer, A.; Pfeffer, K.; Machleidt, T.; Schuetze, S.; Mak, T. W.; Kroenke, M. *Journal of Experimental Medicine* **1995**, *181*, 2059-68.
26. Cain, B. S.; Harken, A. H.; Meldrum, D. R. *Journal of molecular and cellular cardiology* **1999**, *31*, 931-47.
27. Grassme, H.; Jendrossek, V.; Bock, J.; Riehle, A.; Gulbins, E. *Journal of Immunology* **2002**, *168*, 298-307.
28. Grassme, H.; Cremesti, A.; Kolesnick, R.; Gulbins, E. *Oncogene* **2003**, *22*, 5457-5470.
29. Simarro, M.; Calvo, J.; Vila, J. M.; Places, L.; Padilla, O.; Alberola-Ila, J.; Vives, J.; Lozano, F. *Journal of immunology (Baltimore, Md. : 1950)* **1999**, *162*, 5149-55.

30. Santana, P.; Pena, L. A.; Friedman, A. H.; Martin, S.; Green, D.; McLoughlin, M.; Cordon-Cardo, C.; Schuchman, E. H.; Fuks, Z.; Kolesnick, R. *Cell (Cambridge, Massachusetts)* **1996**, *86*, 189-199.
31. Pena, L. A.; Fuks, Z.; Kolesnick, R. N. *Cancer Research* **2000**, *60*, 321-327.
32. Garcia-Barros, M.; Paris, F.; Cordon-Cardo, C.; Lyden, D.; Rafii, S.; Haimovitz-Friedman, A.; Fuks, Z.; Kolesnick, R. *Science (Washington, DC, United States)* **2003**, *300*, 1155-1159.
33. Charruyer, A.; Grazide, S.; Bezombes, C.; Mueller, S.; Laurent, G.; Jaffrezou, J.-P. *Journal of Biological Chemistry* **2005**, *280*, 19196-19204.
34. Grassme, H.; Gulbins, E.; Brenner, B.; Ferlinz, K.; Sandhoff, K.; Harzer, K.; Lang, F.; Meyer, T. F. *Cell (Cambridge, Massachusetts)* **1997**, *91*, 605-615.
35. Grassme, H.; Jendrossek, V.; Riehle, A.; von Kuerthy, G.; Berger, J.; Schwarz, H.; Weller, M.; Kolesnick, R.; Gulbins, E. *Nature Medicine (New York, NY, United States)* **2003**, *9*, 322-330.
36. Hannun, Y. A.; Obeid, L. M. *Journal of Biological Chemistry* **2002**, *277*, 25847-25850.
37. Wang, T.-Y.; Silvius, J. R. *Biophysical Journal* **2003**, *84*, 367-378.
38. Kolesnick, R. N.; Goni, F. M.; Alonso, A. *Journal of cellular physiology* **2000**, *184*, 285-300.
39. Kinnunen, P. K. J.; Koiv, A.; Lehtonen, J. Y. A.; Rytoemaa, M.; Mustonen, P. *Chemistry and Physics of Lipids* **1994**, *73*, 181-207.
40. Ransac, S.; Moreau, H.; Riviere, C.; Verger, R. *Methods in Enzymology* **1991**, *197*, 49-65.
41. Maggio, B.; Bianco, I. D.; Montich, G. G.; Fidelio, G. D.; Yu, R. K. *Biochimica et Biophysica Acta* **1994**, *1190*, 137-48.
42. Honger, T.; Jorgensen, K.; Biltonen, R. L.; Mouritsen, O. G. *Biochemistry* **1996**, *35*, 9003-9006.
43. Wakelam, M. J. O.; Pettitt, T. R.; Kaur, P.; Briscoe, C. P.; Stewart, A.; Paul, A.; Paterson, A.; Cross, M. J.; Gardner, S. D.; et al. *Advances in Second Messenger and Phosphoprotein Research* **1993**, *28*, 73-80.
44. Boguslavsky, V.; Rebecchi, M.; Morris, A. J.; Jhon, D. Y.; Rhee, S. G.; McLaughlin, S. *Biochemistry* **1994**, *33*, 3032-7.
45. Fanani, M. L.; Maggio, B. *Molecular Membrane Biology* **1997**, *14*, 25-29.
46. Maggio, B. *Molecular Membrane Biology* **1996**, *13*, 109-112.
47. Maggio, B. *Journal of Lipid Research* **1999**, *40*, 930-939.
48. Volwerk, J. J.; Filthuth, E.; Griffith, O. H.; Jain, M. K. *Biochemistry* **1994**, *33*, 3464-74.
49. Bianco, I. D.; Fidelio, G. D.; Yu, R. K.; Maggio, B. *Biochemistry* **1991**, *30*, 1709-14.
50. Berg, O. G.; Rogers, J.; Yu, B.-Z.; Yao, J.; Romsted, L. S.; Jain, M. K. *Biochemistry* **1997**, *36*, 14512-14530.
51. Honger, T.; Jorgensen, K.; Stokes, D.; Biltonen, R. L.; Mouritsen, O. G. *Methods in Enzymology* **1997**, *286*, 168-190.
52. Op den Kamp, J. A. F.; Kauerz, M. T.; Van Deenen, L. L. M. *Biochimica et Biophysica Acta* **1975**, *406*, 169-77.
53. Bell, J. D.; Burnside, M.; Owen, J. A.; Royall, M. L.; Baker, M. L. *Biochemistry* **1996**, *35*, 4945-55.
54. Muderhwa, J. M.; Brockman, H. L. *Journal of Biological Chemistry* **1992**, *267*, 24184-92.
55. Fanani, M. L.; Maggio, B. *Journal of lipid research* **2000**, *41*, 1832-40.

56. Ruiz-Arguello, M. B.; Veiga, M. P.; Arrondo, J. L. R.; Goni, F. M.; Alonso, A. *Chemistry and Physics of Lipids* **2002**, *114*, 11-20.
57. Grassme, H.; Schwarz, H.; Gulbins, E. *Biochemical and Biophysical Research Communications* **2001**, *284*, 1016-1030.
58. Tepper, A. D.; Ruurs, P.; Wiedmer, T.; Sims, P. J.; Borst, J.; Van Blitterswijk, W. J. *Journal of Cell Biology* **2000**, *150*, 155-164.
59. Van Blitterswijk, W. J.; Van der Luit, A. H.; Caan, W.; Verheij, M.; Borst, J. *Biochemical Society Transactions* **2001**, *29*, 819-824.
60. Veiga, M. P.; Arrondo, J. L. R.; Goni, F. M.; Alonso, A. *Biophysical Journal* **1999**, *76*, 342-350.
61. Holopainen, J. M.; Lehtonen, J. Y. A.; Kinnunen, P. K. J. *Chemistry and Physics of Lipids* **1997**, *88*, 1-13.
62. Holopainen, J. M.; Subramanian, M.; Kinnunen, P. K. *Biochemistry* **1998**, *37*, 17562-70.
63. Slotte, J. P. *Biochimica et biophysica acta* **1995**, *1235*, 419-27.
64. Fanani, M. L.; Hartel, S.; Oliveira, R. G.; Maggio, B. *Biophysical Journal* **2002**, *83*, 3416-3424.
65. Holopainen, J. M.; Subramanian, M.; Kinnunen, P. K. J. *Biochemistry* **1998**, *37*, 17562-17570.
66. Shah, J.; Atienza, J. M.; Duclos, R. I., Jr.; Rawlings, A. V.; Dong, Z.; Shipley, G. G. *Journal of lipid research* **1995**, *36*, 1936-44.
67. Ruiz-Arguello, M. B.; Basanez, G.; Goni, F. M.; Alonso, A. *Journal of Biological Chemistry* **1996**, *271*, 26616-26621.
68. Montes, L. R.; Ruiz-Arguello, M. B.; Goni, F. M.; Alonso, A. *Journal of Biological Chemistry* **2002**, *277*, 11788-11794.
69. Nurminen, T. A.; Holopainen, J. M.; Zhao, H.; Kinnunen, P. K. J. *Journal of the American Chemical Society* **2002**, *124*, 12129-12134.
70. Zha, X.; Pierini, L. M.; Leopold, P. L.; Skiba, P. J.; Tabas, I.; Maxfield, F. R. *Journal of cell biology* **1998**, *140*, 39-47.
71. Holopainen, J. M.;. Angelova, M. I; Kinnunen, P. K. J. *Biophysical journal* **2000**, *78*, 830-838.
72. Hartel, S.; Fanani, M. L.; Maggio, B. *Biophys. J.*, **2005**, *88*, 287-304.
73. Johnston, I.; Johnston, L. J. *Langmuir* **2006**, *22*, 11284-11289.
74. Chiantia, S.; Kahya, N.; Ries, J.; Schwille, P. *Biophysical Journal* **2006**, *90*, 4500-4508.
75. de Almeida, R. F. M.; Borst, J.; Fedorov, A.; Prieto, M.; Visser, A. J. W. G. *Biophysical Journal* **2007**, *93*, 539-553.
76. Johnston, I.; Johnston, L. J. *Biochim. Biophys. Acta, Biomembr.* **2008**, *1778*, 185-197.
77. Parmar, M. M.; Edwards, K.; Madden, T. D. *Biochimica et Biophysica Acta* **1999**, *1421*, 77-90.
78. Curran, A. R.; Templer, R. H.; Booth, P. J. *Biochemistry* **1999**, *38*, 9328-9336.
79. Steinem, C.; Janshoff, A.; Ulrich, W.-P.; Sieber, M.; Galla, H.-J. *Biochimica et Biophysica Acta* **1996**, *1279*, 169-80.
80. Nielsen, L. K.; Vishnyakov, A.; Jorgensen, K.; Bjornholm, T.; Mouritsen, O. G. *Journal of Physics: Condensed Matter* **2000**, *12*, A309-A314.
81. Ratinov, V.; Plonsky, I.; Zimmerberg, J. *Biophysical Journal* **1998**, *74*, 2374-2387.
82. Salamon, Z.; Huang, D.; Cramer, W. A.; Tollin, G. *Biophysical Journal* **1998**, *75*, 1874-1885.

83. Reviakine, I.; Brisson, A. *Langmuir* **2000**, *16*, 1806-1815.
84. Keller, C. A.; Kasemo, B. *Biophysical Journal* **1998**, *75*, 1397-1402.
85. Salafsky, J.; Groves, J. T.; Boxer, S. G. *Biochemistry* **1996**, *35*, 14773-14781.
86. Nollert, P.; Kiefer, H.; Jaehnig, F. *Biophysical Journal* **1995**, *69*, 1447-55.
87. Cremer, P. S.; Boxer, S. G. *Journal of Physical Chemistry B* **1999**, *103*, 2554-2559.
88. Starr, T. E.; Thompson, N. L. *Langmuir* **2000**, *16*, 10301-10308.
89. Stottrup, B. L.; Veatch, S. L.; Keller, S. L. *Biophysical Journal* **2004**, *86*, 2942-2950.
90. Tampe, R.; Dietrich, C.; Gritsch, S.; Elender, G.; Schmitt, L. *Nanofabrication and Biosystems* **1996**, 201-221.
91. Stelzle, M.; Weissmueller, G.; Sackmann, E. *Journal of Physical Chemistry* **1993**, *97*, 2974-81.
92. Lahiri, J.; Fate, G. D.; Ungashe, S. B.; Groves, J. T. *Journal of the American Chemical Society* **1996**, *118*, 2347-58.
93. Raedler, J.; Strey, H.; Sackmann, E. *Langmuir* **1995**, *11*, 4539-48.
94. Hook, F.; Kasemo, B.; Nylander, T.; Fant, C.; Sott, K.; Elwing, H. *Analytical chemistry* **2001**, *73*, 5796-804.
95. Kiessling, V.; Tamm, L. K. *Biophysical Journal* **2003**, *84*, 408-418.
96. Tamm, L. K.; McConnell, H. M. *Biophysical Journal* **1985**, *47*, 105-13.
97. Tamm, L. K. *Biochemistry* **1988**, *27*, 1450-7.
98. Dietrich, C.; Merkel, R.; Tampe, R. *Biophysical Journal* **1997**, *72*, 1701-1710.
99. Merkel, R.; Sackmann, E.; Evans, E. *Journal de Physique (Paris)* **1989**, *50*, 1535-55.
100. Rinia, H. A.; de Kruijff, B. *FEBS Letters* **2001**, *504*, 194-199.
101. Milhiet, P. E.; Domec, C.; Giocondi, M.-C.; Van Mau, N.; Heitz, F.; Le Grimellec, C. *Biophysical Journal* **2001**, *81*, 547-555.
102. Yip, C. M.; Darabie, A. A.; McLaurin, J. *Journal of Molecular Biology* **2002**, *318*, 97-107.
103. Mou, J.; Yang, j.; Shao, Z. *Journal of Molecular Biology* **1995**, *248*, 507-12.
104. Schneider, J.; Dufrene, Y. F.; Barger, W. R., Jr.; Lee, G. U. *Biophysical Journal* **2000**, *79*, 1107-1118.
105. Angelova, M.; Soleau, S.; Meleard, P.; Faucon, J. F.; Bothorel, P. *Progress in Colloid & Polymer Science* **1992**, *89*, 127-31.
106. Angelova, M.; Dimitrov, D. *Faraday Discussions of the Chemical Society* **1986**, *81*, 303-11.
107. Radhakrishnan, A.; McConnell, H. *Proceedings of the National Academy of Sciences of the United States of America* **2005**, *102*, 12662-12666.
108. Ratto, T. V.; Longo, M. L. *Biophysical Journal* **2002**, *83*, 3380-3392.
109. Stottrup, B. L.; Veatch, S. L.; Keller, S. L. *Biophysical Journal* **2004**, *86*, 2942-2950.
110. Blanchette Craig, D.; Lin, W.-C.; Ratto Timothy, V.; Longo Marjorie, L. *Biophysical journal* **2006**, *90*, 4466-78.
111. Horton, M. R., Massachusetts Institute of Technology, 2006.
112. Duffy, D. C.; McDonald, J. C.; Schueller, O. J. A.; Whitesides, G. M. *Analytical Chemistry* **1998**, *70*, 4974-4984.
113. Bernard, A.; Delamarche, E.; Schmid, H.; Michel, B.; Bosshard, H. R.; Biebuyck, H. *Langmuir* **1998**, *14*, 2225-2229.
114. James, C. D.; Davis, R. C.; Kam, L.; Craighead, H. G.; Isaacson, M.; Turner, J. N.; Shain, W. *Langmuir* **1998**, *14*, 741-744.

115. James, C. D.; Davis, R.; Meyer, M.; Turner, A.; Turner, S.; Withers, G.; Kam, L.; Banker, G.; Craighead, H.; Isaacson, M.; Turner, J.; Shain, W. *IEEE transactions on bio-medical engineering* **2000**, *47*, 17-21.
116. Richter, R. P.; Him, J. L. K.; Brisson, A. *Materials Today (Oxford, United Kingdom)* **2003**, *6*, 32-37.
117. Ekeroth, J.; Konradsson, P.; Hoeoek, F. *Langmuir* **2002**, *18*, 7923-7929.
118. Reimhult, E.; Hook, F.; Kasemo, B. *Journal of Chemical Physics* **2002**, *117*, 7401-7404.
119. Reimhult, E.; Hoeoek, F.; Kasemo, B. *Langmuir* **2003**, *19*, 1681-1691.
120. Sackmann, E. *Science (Washington, D. C.)* **1996**, *271*, 43-8.
121. Reviakine, I.; Simon, A.; Brisson, A. *Langmuir* **2000**, *16*, 1473-1477.
122. Keller, C. A.; Glasmastar, K.; Zhdanov, V. P.; Kasemo, B. *Physical Review Letters* **2000**, *84*, 5443-5446.
123. Puu, G.; Gustafson, I. *Biochimica et Biophysica Acta* **1997**, *1327*, 149-161.
124. Pignataro, B.; Steinem, C.; Galla, H.-J.; Fuchs, H.; Janshoff, A. *Biophysical Journal* **2000**, *78*, 487-498.
125. Reimhult, E.; Hook, F.; Kasemo, B. *Physical review. E, Statistical, nonlinear, and soft matter physics* **2002**, *66*, 051905.
126. Yu, B.-Z.; Zakim, D.; Jain, M. K. *Biochimica et Biophysica Acta, Molecular and Cell Biology of Lipids* **2002**, *1583*, 122-132.
127. Linke, T.; Wilkening, G.; Lansmann, S.; Moczall, H.; Bartelsen, O.; Weisgerber, J.; Sandhoff, K. *Biological Chemistry* **2001**, *382*, 283-290.
128. Moore, D. J.; Rerek, M. E.; Mendelsohn, R. *Journal of Physical Chemistry B* **1997**, *101*, 8933-8940.
129. Goni, F. M.; Alonso, A. *Biochimica et Biophysica Acta, Biomembranes* **2006**, *1758*, 1902-1921.
130. Goni, F. M.; Alonso, A. *Bioscience reports* **2000**, *20*, 443-63.
131. Holopainen, J. M.; Angelova, M. I.; Kinnunen, P. K. J. *Biophysical Journal* **2000**, *78*, 830-838.
132. Basanez, G.; Ruiz-Arguello, M. B.; Alonso, A.; Goni, F. M.; Karlsson, G.; Edwards, K. *Biophysical journal* **1997**, *72*, 2630-7.
133. Silva, L. C.; de Almeida, R. F. M.; Castro, B. M.; Fedorov, A.; Prieto, M. *Biophysical Journal* **2007**, *92*, 502-516.
134. Castro, B. M.; de Almeida, R. F. M.; Silva, L. C.; Fedorov, A.; Prieto, M. *Biophys. J. %R 10.1529/biophysj.107.107714* **2007**, *93*, 1639-1650.
135. Kung, L. A.; Kam, L.; Hovis, J. S.; Boxer, S. G. *Langmuir* **2000**, *16*, 6773-6776.
136. Soille, P. *Morphological image analysis: principles and applications*; Springer-Verlag New York, Inc. : Secaucus, NJ, USA, 2003.
137. Otsu, N. *IEEE Transactions on Systems, Man, and Cybernetics* **1979**, 62–66.
138. Veatch, S. L.; Keller, S. L. *Biochimica et Biophysica Acta, Molecular Cell Research* **2005**, *1746*, 172-185.
139. Ishitsuka, R.; Sato, S. B.; Kobayashi, T. *J Biochem (Tokyo)* **2005**, *137*, 249-254.
140. Yamaji, A.; Sekizawa, Y.; Emoto, K.; Sakuraba, H.; Inoue, K.; Kobayashi, H.; Umeda, M. *J. Biol. Chem.* **1998**, *273*, 5300-5306.
141. Kiyokawa, E.; Makino, A.; Ishii, K.; Otsuka, N.; Yamaji-Hasegawa, A.; Kobayashi, T. *Biochemistry* **2004**, *43*, 9766-9773.
142. Kashchiev, D. *Nucleation: Basic Theory with Applications*; Butterworth-Heinemann, 2000.

143. DW Grainger, A. R., H Ringsdorf, C Salesse *FEBS letters* **1989**
144. *252*, 73-82.
145. Dressler, K. A.; Mathias, S.; Kolesnick, R. N. *Science (Washington, DC, United States)* **1992**, *255*, 1715-18.
146. Cifone, M. G.; De Maria, R.; Roncaioli, P.; Rippo, M. R.; Azuma, M.; Lanier, L. L.; Santoni, A.; Testi, R. *Journal of Experimental Medicine* **1994**, *180*, 1547-52.
147. Haimovitz-Friedman, A.; Kan, C. C.; Ehleiter, D.; Persaud, R. S.; McLoughlin, M.; Fuks, Z.; Kolesnick, R. N. *J Exp Med FIELD Full Journal Title:The Journal of experimental medicine* **1994**, *180*, 525-35.
148. Mathias, S.; Younces, A.; Kan, C. C.; Orlow, I.; Joseph, C.; Kolesnick, R. N. *Science (Washington, DC, United States)* **1993**, *259*, 519-22.
149. Fanzo, J. C.; Lynch, M. P.; Phee, H.; Hyer, M.; Cremesti, A.; Grassme, H.; Norris, J. S.; Coggeshall, K. M.; Rueda, B. R.; Pernis, A. B.; Kolesnick, R.; Gulbins, E. *Cancer Biology & Therapy* **2003**, *2*, 392-395.
150. Kim, M. Y.; Linardic, C.; Obeid, L.; Hannun, Y. *Journal of Biological Chemistry* **1991**, *266*, 484-9.
151. Cremesti, A.; Paris, F.; Grassme, H.; Holler, N.; Tschopp, J.; Fuks, Z.; Gulbins, E.; Kolesnick, R. *Journal of Biological Chemistry* **2001**, *276*, 23954-23961.
152. Grassme, H.; Jendrossek, V.; Riehle, A.; von Kurthy, G.; Berger, J.; Schwarz, H.; Weller, M.; Kolesnick, R.; Gulbins, E. *Nat Med FIELD Full Journal Title:Nature medicine* **2003**, *9*, 322-30.
153. Tepper, C. G.; Jayadev, S.; Liu, B.; Bielawska, A.; Wolff, R.; Yonehara, S.; Hannun, Y. A.; Seldin, M. F. *Proceedings of the National Academy of Sciences of the United States of America* **1995**, *92*, 8443-7.
154. Liu, P.; Anderson, R. G. W. *Journal of Biological Chemistry* **1995**, *270*, 27179-85.
155. Gulbins, E.; Kolesnick, R. *Oncogene* **2003**, *22*, 7070-7077.
156. Patra, S. K. *Biochimica et Biophysica Acta, Reviews on Cancer* **2008**, *1785*, 182-206.
157. London, M.; London, E. *Journal of Biological Chemistry* **2004**, *279*, 9997-10004.
158. Chao, L.; Hatton, T. A.; Gast, A. P.; Jensen, K. F. *manuscript in preparation*.
159. Baumgart, T.; Hess, S. T.; Webb, W. W. *Nature (London, United Kingdom)* **2003**, *425*, 821-824.
160. Veatch, S. L.; Keller, S. L. *Biophysical Journal* **2003**, *85*, 3074-3083.
161. Castro, B. M.; de Almeida, R. F. M.; Silva, L. C.; Fedorov, A.; Prieto, M. *Biophys J* **2007**, *93*, 1639-1650.
162. Blanchette, C. D.; Lin, W.-C.; Orme, C. A.; Ratto, T. V.; Longo, M. L. *Biophys. J.* **2008**, *94*, 2691-2697.
163. Jacobson, K.; Mouritsen, O. G.; Anderson, R. G. W. *Nature Cell Biology* **2007**, *9*, 7-14.
164. van Meer, G. *Science (Washington, DC, United States)* **2002**, *296*, 855, 857.
165. Dykstra, M.; Cherukuri, A.; Sohn, H. W.; Tzeng, S.-J.; Pierce, S. K. *Annual Review of Immunology* **2003**, *21*, 457-481.
166. Golub, T.; Wacha, S.; Caroni, P. *Current Opinion in Neurobiology* **2004**, *14*, 542-550.
167. Gomez-Mouton, C.; Abad, J. L.; Mira, E.; Lacalle, R. A.; Gallardo, E.; Jimenez-Baranda, S.; Illa, I.; Bernad, A.; Manes, S.; Martinez, A. C. *Proc Natl Acad Sci U S A FIELD Full Journal Title:Proceedings of the National Academy of Sciences of the United States of America* **2001**, *98*, 9642-7.

168. Gomez-Mouton, C.; Lacalle, R. A.; Mira, E.; Jimenez-Baranda, S.; Barber, D. F.; Carrera, A. C.; Martinez-A, C.; Manes, S. *Journal of Cell Biology* **2004**, *164*, 759-768.
169. Pierini, L. M.; Eddy, R. J.; Fuortes, M.; Seveau, S.; Casulo, C.; Maxfield, F. R. *Journal of Biological Chemistry* **2003**, *278*, 10831-10841.
170. Bruses, J. L.; Chauvet, N.; Rutishauser, U. *Journal of Neuroscience* **2001**, *21*, 504-512.
171. Hering, H.; Lin, C.-C.; Sheng, M. *Journal of Neuroscience* **2003**, *23*, 3262-3271.
172. Gajate, C.; Mollinedo, F. *Blood* **2001**, *98*, 3860-3863.
173. Jan, J. T.; Chatterjee, S.; Griffin, D. E. *J Virol FIELD Full Journal Title:Journal of virology* **2000**, *74*, 6425-32.
174. Ridgway, N. D.; Lagace, T. A.; Cook, H. W.; Byers, D. M. *Journal of Biological Chemistry* **1998**, *273*, 31621-31628.
175. Freitas, R. A. *Nanomedicine* Austin, TX : Landes Bioscience, <c2003> 1999; Vol. v. 1.
176. Simons, K.; Ikonen, E. *Science (Washington, D. C.)* **2000**, *290*, 1721-1726.
177. Avrami, M. *J. Chem. Phys.* **1939**, *7*, 1103-12.
178. Mullins, W. M.; Elsass, C. R. *Biochem. J.* **1993**, *291*, 326-8.
179. Yang, J.; McCoy, B. J.; Madras, G. *J. Chem. Phys.* **2005**, *122*, 064901/1-064901/10.
180. Narine, S. S.; Humphrey, K. L.; Bouzidi, L. *J. Am. Oil Chem. Soc.* **2006**, *83*, 913-921.
181. Deen, W. M. In *Analysis of Transport Phenomena*; Oxford University Press: New York Oxford, 1998, p 30-63.
182. Chen, F.; Smith, K. A.; Hatton, T. A. *AIChE 2007 Annual Meeting* **2007**.
183. Sethian, J. A. *Level set methods and fast marching methods*; 2nd ed.; Cambridge University Press: Cambridge, UK, 1999.

APPENDIX

Matlab Code for Modeling SM-induced Solvent-mediated Phase Transfromation

1. Program: moving_boundary.m-- Main program that generates and updates the marker points on the boundaries of domains after every time step.

2. Subroutine: m_fem_comsol.m-- To solve the concentration profile via Comsol solver

3. Subroutine: updating_markerp.m-- To eliminate undesired topological changes and redistribute the marker points

4. Subroutine: calculate_normal.m-- To calculate the normal vector of domain boundary at each marker point

5. Subroutine: random_init.m-- To obtain a random distribution of domains in the initial morphology

```
function fem=moving_boundary(d, n, num, timeinterval, step, DaG, DaD, Dk,
filename,filename1, check)

%name the figures with the input parameters----------------------------
str1=num2str(d);
str2=num2str(n);
str3=num2str(num);
str4=num2str(timeinterval);
str5=num2str(step);
str6=num2str(DaG);
str7=num2str(DaD);
str8=num2str(Dk);
str9=['d=' str1 ',n=' str2 ',num=' str3 ',timeinterval=' str4 ',step=' str5
',DaG=' ...
      str6 ',DaD=' str7 ',Dk=' str8, '','Surface: Concentration, c'];
str10=['d=' str1 ',n=' str2 ',num=' str3 ',timeinterval='];
str11=[ str5 ',DaG=' str6 ',DaD=' str7 ',Dk=' str8 ];


%input the initial geometry-------------------------------------------------
%coordinates of the center of round objects--obtained from random_init.m
xoo=[ 0.8710    0.2993   -0.2987   -0.4080    0.5004 ...
    -0.5012   -0.2189   -0.7851    0.0919   -0.3465 ...
    0.7767    0.2118    0.5950    0.8433   -0.2296    ...
    0.6932   -0.6617    0.6418    0.4450    0.0188 ...
    0.1311   -0.6670   -0.8336   -0.6582    0.1185  ...
    -0.5445    0.7864    0.5406   -0.8985   -0.8256 ];

yoo=[ 0.8362    0.4071    0.0410    0.3931   -0.7541 ...
    -0.5329   -0.2873    0.4704   -0.8074    0.8378 ...
    -0.2196    0.1126    0.8239    0.1471   -0.6068 ...
    -0.5226   -0.7848    0.4744   -0.3269    0.4915 ...
    0.8169    0.0889   -0.4091    0.8975   -0.4062 ...
    0.6516   -0.8426    0.1686    0.7254   -0.1371 ];

r=0.1;% radius of the round objects

%to construct and plot initial marker points
figure;
orig_length=2*r*pi/n;%length between two marker points
s=0:360/n:(360-360/n);
for i=1:num
xo=xoo(i)+r*cos(s/360*2*pi);
yo=yoo(i)+r*sin(s/360*2*pi);
p{i}=[xo; yo];% p(0)
hold on;
plot (xo,yo);
end

%time step to obtain the updated geometry-----------------------------
%initial set up
fem0=0;
inde=ones(1, num);
time_dissolution=zeros(1, num);

%the time step starts
```

```
for f=1:step
    %different time steps have different intervals to increase the time
    %scale we examine
 if (f>40)&&(f<=46)
     timeinterval_m=10*timeinterval;
 elseif f>46
     timeinterval_m=100*timeinterval;
 else
    timeinterval_m=timeinterval;
 end

%obtain the concentration profile in m_fem_comsol
fem=m_fem_comsol(d, num, p, timeinterval_m, DaG, DaD,f, fem0);
clear fem0;
fem0=fem;
clear p0;
p0=p;

%updating marker points of each domain
for i=1:num% for ith domain
 if length(p{i})>d
     clear u;
     %obtain concentration at marker points from the concentration profile
obtained in m_fem_comsol
     u = postinterp(fem, 'c', p{i});

     %calculate the displacement of marker points
     clear nx;clear ny;
     [nx, ny]=calculate_normal(p{i});%obtain normal vector toward domains at
the marker points
     clear h
     h=timeinterval_m*Dk*DaD*(ones(1, length(u))-u);%Equation of motion of
domain boundary
     clear xo; clear yo;
     xo=p{i}(1,:);
     yo=p{i}(2,:);
     xo=xo+nx.*h;%1*n
     yo=yo+ny.*h;%1*n
     clear p{i};
     p{i}=[xo; yo];%2*n--updated p after boundary moved

     %to redistribute marker points and eliminate undesired topological
changes in updating_markerp.m
     clear restructured_p;
     [restructed_p, N]=updating_markerp(p{i}, p0{i}, orig_length, d, check);
     clear p{i};
     p{i}=restructed_p;%2*n resturctured p
     psize(i)=length(p{i});
     clear xo;
     clear yo;
     xo=p{i}(1,:);
     yo=p{i}(2,:);
     %polt the updated boundaries of domains
     hold on;
     plot(xo, yo,'m-');
```

```
 end%end if the ith domain still exists

end%end of updating boundaries of each domain (i)

% plot the concentration profile plot with initial geometry of domains
figure;
for i=1:num
xo1=xoo(i)+r*cos(s/360*2*pi);
yo1=yoo(i)+r*sin(s/360*2*pi);
hold on;
plot(xo1,yo1,'k-')
end
hold on;
postplot(fem, ...
         'tridata',{'c','cont','internal'}, ...
         'tridlim',[0 1],...
         'trimap','jet(1024)', ...
         'solnum','end', ...
         'title',str9, ...
         'refine',3, ...
         'axis',[-1,1,-1,1,-1,1]);
str20=num2str(f);
     filenameK=[ filename1 str20];
saveas(gcf,filenameK,'jpg')
close(gcf)

end% end of each timestep

saveas(gcf,filename1,'jpg')
close(gcf)
end



%=========================================================================
%=========================================================================


function fem=m_fem_comsol(d, num, p, timeinterval, DaG, DaD,f, fem0)

flclear fem

% COMSOL version
clear vrsn
vrsn.name = 'COMSOL 3.2';
vrsn.ext = '';
vrsn.major = 0;
vrsn.build = 222;
vrsn.rcs = '$Name:  $';
vrsn.date = '$Date: 2005/09/01 18:02:30 $';
fem.version = vrsn;

%construct initial geometry-----------------------------------------------
g1=square2('2','base','center','pos',{'0','0'},'rot','0');%corral boundary
g2=circ2('0.05','base','center','pos',{'0','0'},'rot','0');%SMase-feature
g6=geomcomp({g1,g2},'ns',{'g1','g2'},'sf','g1-g2','edge','none');
```

```
for i=1:num %ith SM-domains
clear c;clear g;
if length(p{i})>d
c=geomspline(p{i}, 'splinemethod','uniform','closed','on');
g=solid2(c);
g6=geomcomp({g6,g},'ns',{'g6','g'},'sf','g6-g','edge','none');
end
end

clear s
s.objs={g6};
s.name={'CO1'};
s.tags={'g6'};

fem.draw=struct('s',s);
fem.geom=geomcsg(fem);


fem.mesh = meshinit(fem);
       fem.shape = 2;
       fem.xmesh = meshextend(fem);

% Boundary conditions-------------------------------------------------
clear appl
appl.mode.class = 'Diffusion';
appl.module = 'CHEM';
appl.assignsuffix = '_chdi';
clear bnd
bnd.type = {'N0','N','N'};
bnd.kc = {0,DaG,DaD};
bnd.cb = {0,0,1};
bnd.ind(1:4)=[1,1,1,1];
bnd.ind(5:8)=[2,2,2,2];

nk=0;
for i=1:num
    if length(p{i})>d
        nk=nk+length(p{i});
    end
end

if nk==0
else
bnd.ind(9:8+nk)=ones(1,nk).*3;
end
appl.bnd = bnd;

%initial condition--------------------------------------------------
clear equ
equ.init =1;
equ.ind = [1];
appl.equ = equ;
fem.appl{1} = appl;
fem.border = 1;
fem.outform = 'general';
```

```
fem.units = 'SI';

% Multiphysics-----------------------------------------------------
fem=multiphysics(fem);

% Extend mesh------------------------------------------------------
fem.xmesh=meshextend(fem);

% Evaluate initial value using current solution-------------------
if f==1
   fem.sol=femtime(fem, ...
                'solcomp',{'c'}, ...
                'outcomp',{'c'}, ...
                'tlist',[0:timeinterval:timeinterval], ...
                'tout','tlist');
else
init = asseminit(fem,'init',fem0)
% Solve problem
fem.sol=femtime(fem, ...
                'init',init, ...
                'solcomp',{'c'}, ...
                'outcomp',{'c'}, ...
                'tlist',[0:timeinterval:timeinterval], ...
               'tout','tlist');
end

end


%=========================================================================
%=========================================================================


function [restructed_p, N]=updating_markerp(p, p0, orig_length, d, check)
clear p_add
tot_num_added =0;

IN = inpolygon(p(1,:), p(2,:), p0(1,:), p0(2,:) );
INN=1-IN;
%check if the displacement of boundaries is beyond the region of the original
domain
if ~isempty(find(INN,1))
    restructed_p=[0; 0];
    N=0;
else

%to eliminate undesired topological change-----------------------------------
--------
if length(p)>d
 crosstest=1;
while (crosstest>0) && (length(p)>d)
    crosstest=0;
for i=1:length(p)
    add_point=0;

    if check >length(p)
```

```
        check=length(p);
    end

    for j=2:check
        [cros, crosy]=polyxpoly([p(1,i),p(1,mod(i,
length(p))+1)],[p(2,i),p(2,mod(i,length(p))+1)],[p(1,mod(i+j-1,  length(p))+1),
p(1, mod(i+j, length(p))+1)],[p(2,mod(i+j-1, length(p))+1),
p(2,mod(i+j,length(p))+1)]);
        if ~isempty(cros)
            crosstest=crosstest+1;
            if (i+j+1)<= length(p)
            p_add(1,:)= sum(p(1,i:i+j+1))/(j+2);
            p_add(2,:)= sum(p(2,i:i+j+1))/(j+2);
            p=[p(:,1:i-1) p_add p(:,i+j+2:length(p))];
            else
            p_add(1,:)= (sum(p(1,i:length(p)))+ sum(p(1,1:i+j+1-
length(p))))/(j+2);
            p_add(2,:)= (sum(p(2,i:length(p)))+ sum(p(2,1:i+j+1-
length(p))))/(j+2);
            p=[p(:,i+j+2-length(p):i-1) p_add];
            end
            tot_num_added=tot_num_added-j-1;
            add_point=1;
            break;
        end
    end
    if add_point
        break;
    end
end
end
end


% to redistribute marker points----------------------------------------
num_add=1;
kk=1;
while (num_add~=0)&&(length(p)>d)

 for i=kk:(length(p)-1)%%%kk-->1
%add points if two points are too far apart
       if length(p)<=d
       break;
       end
          num_add=round(norm(p(:,i+1)-p(:,i))/orig_length)-1;

          clear p_add;
       if num_add>0
            for jj=1:num_add
                p_add(:,jj)=p(:,i)+jj/(num_add+1)*(p(:,i+1)-p(:,i));
            end;
                tot_num_added=tot_num_added+num_add;
                p=[p(:,1:i) p_add p(:,i+1:length(p))];
              %  kk=i-1;
                break;
       end;
```

```
%remove points if two points are too close
if norm(p(:,i+1)-p(:,i))/orig_length < 0.625
    p_add=(p(:,i)+p(:,i+1))/2;
    if i+2>length(p)
    p=[p(:,1:i-1) p_add ];
    else
    p=[p(:,1:i-1) p_add p(:, i+2:length(p))];
    end
    tot_num_added=tot_num_added-1;
    num_add =1;
    %kk=i-1;%%
    break;
end
 end
end

%special treatment to the starting and end marker points-----------------
if (length(p)>d)
    num_add=round(norm(p(:,1)-p(:, length(p)))/orig_length)-1;
    clear p_add;
    if num_add>0
        for jj=1:num_add
            p_add(:,jj)=p(:, length(p))+jj/(num_add+1)*(p(:,1)-p(:,
length(p)));
        end;
        p=[ p p_add];
        tot_num_added=tot_num_added+num_add;
    end;

    if norm(p(:,1)-p(:, length(p)))/orig_length < 0.625
        p_add=(p(:, length(p))+p(:,1))/2;
        p=[p_add p(:, 2:length(p)-1)];
        tot_num_added=tot_num_added-1;
    end;
  end
    restructed_p=p;
    N=tot_num_added;

end
    return;

%=========================================================================
%=========================================================================


function [nx, ny]=calculate_normal(p)
[m,n]=size(p);

for i=2:(n-1)
length=((p(1,i+1)-p(1,i-1))^2+(p(2,i+1)-p(2,i-1))^2)^0.5;
ny(i)=(p(1,i+1)-p(1,i-1))/length;
nx(i)=-(p(2,i+1)-p(2,i-1))/length;
end
length=((p(1,2)-p(1,n))^2+(p(2,2)-p(2,n))^2)^0.5;
ny(1)=(p(1,2)-p(1,n))/length;
```

```
nx(1)=-(p(2,2)-p(2,n))/length;
length=((p(1,1)-p(1,n-1))^2+(p(2,1)-p(2,n-1))^2)^0.5;
ny(n)=(p(1,1)-p(1,n-1))/length;
nx(n)=-(p(2,1)-p(2,n-1))/length;
end
%=========================================================================
%=========================================================================

function [xo,yo]=random_init(a,b,n,r,dist)
a=a+r;
b=b-r;

xo(1)=a+(b-a)*rand(1,1);
yo(1)=a+(b-a)*rand(1,1);

for i=2:n
    test=0
while test==0
xo(i)=a+(b-a)*rand(1,1);
yo(i)=a+(b-a)*rand(1,1);
 for j=1:(i-1)
    k=(yo(i)-yo(j))^2+(xo(i)-xo(j))^2;
    if k<=(dist*r)^2
    test=0
        break;
    else
    end
test=1
 end

end
end

s=0:360/20:(360-360/20);
figure;

for i=1:n
xoo=xo(i)+r*cos(s/360*2*pi);
yoo=yo(i)+r*sin(s/360*2*pi);

hold on;
plot (xoo,yoo);
end

end
```